Dissertation zur Erlangung des Doktorgrades

der Fakultät für Chemie und Pharmazie

der Ludwig-Maximilians-Universität München

Solar Light Harvesting with Nanostructured Organic and Hybrid Photovoltaic Devices

Florian Karl Albert Auras

aus

Augsburg

2013

Erklärung

Diese Dissertation wurde im Sinne von § 7 der Promotionsordnung vom 28. November 2011 von Herrn Prof. Dr. Thomas Bein betreut.

Eidesstattliche Versicherung

Diese Dissertation wurde eigenständig und ohne unerlaubte Hilfe erarbeitet.

München, 22.08.2013

(Unterschrift des Autors)

Dissertation eingereicht am 22.08.1013

1. Gutachter: Prof. Dr. Thomas Bein

2. Gutachter: Prof. Dr. Achim Hartschuh

Mündliche Prüfung am 15.10.2013

Danksagung

Zu Beginn möchte ich mich bei meinem Doktorvater, Professor Dr. Thomas Bein, herzlich bedanken für die freundliche Aufnahme in seine Gruppe, sein Vertrauen und die große Freiheit zu eigenverantwortlicher Forschungsarbeit. Besonders die Möglichkeit, an einer Vielzahl interessanter Projekte zusammen mit Kollegen aus verschiedenen Subgroups zu arbeiten, war eine spannende Erfahrung und hat mein wissenschaftlichen Horizont erweitert.

Professor Dr. Achim Hartschuh möchte ich sehr herzlich danken für die Bereitschaft, das Zweitgutachten für diese Arbeit zu erstellen.

Während der Entstehung dieser Arbeit hatte ich die Gelegenheit zu tollen und fruchtbaren Kooperationen mit vielen anderen Arbeitsgruppen an der LMU und anderen Universitäten.

Prof. Dr. Christina Scheu, Angela Wochnik, Christoph Heinzl und Anna Frank möchte ich danken für die Zusammenarbeit bei „Extremerly Thin Absorber" Solarzellen, bei der TEM Charakterisierung und bei den $CuInS_2$-Projekten.

Prof. Dr. Paul Knochel, Thomas Kunz, Veronika Werner, John Markiewicz danke ich sehr für die Zusammenarbeit bei den COF-Projekten und den stetigen Nachschub an neuen Molekülen.

Prof. Dr. Achim Hartschuh, Matthias Handloser, Nicolai Hartmann und Harald Budde möchte ich für die Photolumineszenz- und TCSPC-Messungen und die viele schnelle Hilfe bei Optik-Fragen danken.

Vielen Dank an Dr. Valentina Cauda und Vivian Farías Rivera für die gelungene Zusammenarbeit bei dem ZnO Nanowire Projekt.

Besten Dank an Prof. Dr. Dirk Trauner und Florian Löbermann für die Porphyrine und Phthalocyanine für die PMO Projekte.

Prof. William Dichtel und John Colson danke ich für die kürzlich gestartete und schon sehr fruchtbare Zusammenarbeit bei Photoaktiven COFs.

Der größte Dank geht aber an meine Eltern für die großartige Unterstützung während meines Studiums und der Doktorarbeit. Ohne euch wäre all dies niemals möglich gewesen.

Abstract

In classical photovoltaic systems, free charge carriers are generated upon absorption of a photon and collected at anisotropic contacts. In organic materials however, the low dielectric constant causes the energy that is required to split the bound state initially formed after photoexcitation to be considerably higher than thermal energy at room temperature. The extra energy, however, can be provided by the junction of two materials with different energy levels. In order to achieve high quantum yields, the two materials have to be intermixed on a length scale that allows the bound state to be transferred to the interface, and separated into free charge carriers, before it recombines. Typically, a phase separation on the 10-20 nm scale in bulk heterojunction solar cells is achieved via de-mixing of a precursor solution during thin film deposition. Although this method leads to the desired microstructure if the materials are designed adequately and the processing conditions are selected well, the ability to create a perfectly defined morphology would be highly appreciated in fundamental research. We have pursued different routes for obtaining structurally well-defined bulk heterojunctions.

We used the anisotropic crystal growth of zinc oxide to synthesize arrays of vertically aligned nanowires, and applied them in metal oxide/polymer hybrid photovoltaic devices. Zinc oxide nanowires have been widely studied as photoanodes due to their unique one-dimensional growth and favourable charge transport characteristics. We significantly improved the hydrothermal synthesis for these nanowires, such that we were able to grow well-ordered nanowire arrays on transparent conducting substrates without the formation of bulk precipitates in the growth solution. These unwanted precipitates typically adhere to the growing nanowire array and compromise the film quality and reproducibility. We were able to tune the synthesis conditions towards the growth of extremely thin nanowires, which provide the roughness factors and inter-wire distances that would be most favourable for efficient light harvesting in zinc oxide/polymer photovoltaic devices. In combination with poly(3-hexylthiophene) as a first model system, we obtained a power conversion efficiency of 0.09% under simulated solar illumination. We found that our devices were mainly limited by comparably high dark currents, which originate from a high defect-related doping level.

Additionally, these nanowire arrays were implemented in piezoelectric nanogenerator devices in collaboration with the groups of Dr Valentina Cauda (Istituto Italiano di Tecnologia, Turin, Italy) and Prof Barbara Onida (Politecnico di Torino, Turin, Italy).

Soft templating approaches have been widely used for structuring silica materials. In this approach a structure directing agent, e.g. a block copolymer, is used to define a certain morphology, which is preserved through cross-linking of the precursor materials. We created a highly ordered porphyrin-bridged periodic mesoporous organosilica and studied its charge carrier generation capabilities. While porphyrin-based molecules are known sensitizers in dye-sensitized solar cells and, due to their good intermolecular charge transport, perform well in small molecule organic photovoltaics, the potential of porphyrin as photoactive building block for well-defined organosilica materials had not been explored so far. We synthesized an organosilica with periodically ordered pores and studied its photoresponse in an electrolyte as well as in solid-state heterojunctions after infiltration with a suitable electron acceptor. Taking into account the insulating nature of the silica linkages the observed photocurrents of about $25\,\mathrm{nA\,cm^{-2}}$ are an indication for the existence of stacked porphyrin units inside the material, which render it electronically conductive to some degree.

In the last projects described in this thesis, we employed crystalline covalent organic frameworks (COFs) as semiconducting host materials. These materials consist of extended two-dimensional sheets with an atomically defined arrangement of covalently bound building blocks, which stack in the third dimension via π-π–interactions. We demonstrated that upon infiltration with an electron acceptor a bi-continuous network is formed. We used a recently developed thienothiophene-containing COF to study the infiltration of COF films with fullerene-based electron acceptors. From photoluminescence quenching experiments, we concluded that the COF films have accessible pores throughout their entire thickness, while the degree of achievable pore filling is influenced by the solubility of the employed fullerene derivative. Experiments with acceptors that feature higher LUMO energies resulted in photovoltaic devices with a considerably improved open-circuit voltage.

We then investigated COFs that feature highly absorbing zinc phthalocyanine units in collaboration with the group of Prof William Dichtel (Cornell University, Ithaca, USA). We found that the position and accessibility of the COF building blocks are of key importance for effective charge carrier generation. In the examples we have investigated thus far, the main contribution to the photocurrent originates from the PCBM located inside the COF pores. The charge transport properties, however, seem to be strongly affected by the selection of COF building blocks. We showed that incorporation of the phthalocyanine units, despite their direct contribution to the photocurrent being small, enhances the fraction of collected electrons significantly.

In conclusion, we pursued three different routes to prepare morphologically well-defined three-dimensional heterojunctions of complementary semiconductors. Despite challenges in achieving sufficient infiltration and obtaining an interface that provides high charge carrier generation efficiency and low recombination rates, these nanostructured devices offer a unique degree of definition on the nanoscale, which renders them promising model systems for fundamental research in photovoltaics.

Table of Contents

1   Introduction

Sunlight provides a gigantic amount of practically inexhaustible power to the earth. Out of the 1.74×10^{17} W that hit the atmosphere 8.9×10^{16} W get absorbed by oceans and land (Figure 1.1). Per year, this creates a free supply of 3×10^{24} J to the earth, which is about 10,000 times more than the current energy consumption of all countries.
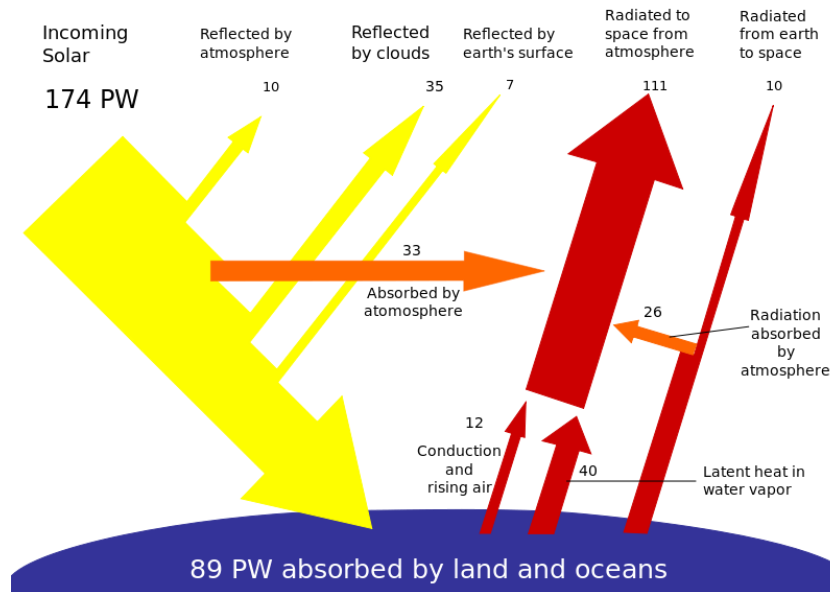
Figure 1.1   Breakdown of the incoming solar power.[1]

Several strategies to utilize solar energy directly or indirectly have been developed. A direct conversion of solar radiation into electricity can be achieved through photovoltaic modules. Figure 1.2 shows the average solar power that is received on the earth's surface. The black dots represent the area that would have to be covered with 8% efficient solar cells to match the world's current consumption of primary energy. Although this area seems small on a global map, it adds up to an area of about the size of Spain.
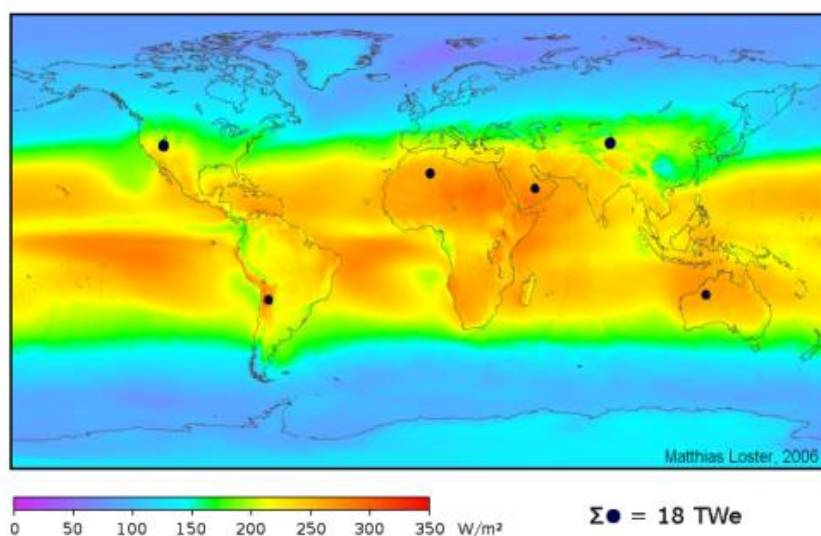
Figure 1.2 Average insolation showing land area (small black dots) required to replace the world primary energy supply with solar electricity (18 TW corresponds to 568 EJ per year).[2]

Currently most installed solar panels are based on crystalline silicon solar cells, which offer good power conversion efficiency and long lifetime. However, their production process is slow and requires large amounts of highly pure chemicals. In order to achieve a significant contribution to the world's power supply within the next decades, the production capacity needs to be increased dramatically. It would therefore be highly desirable to implement new technologies that are compatible with established techniques for mass-production, e.g. roll-to-roll fabrication.

Organic solar cells can be fabricated on flexible substrates using fast deposition processes like thermal evaporation or inkjet printing. Power conversion efficiencies well above 10% have been demonstrated recently.[3] Development of new, highly efficient organic semiconductors and the implementation of advanced device concepts, such as multijunction cells, led to a steep increase of device efficiencies (Figure 1.3).
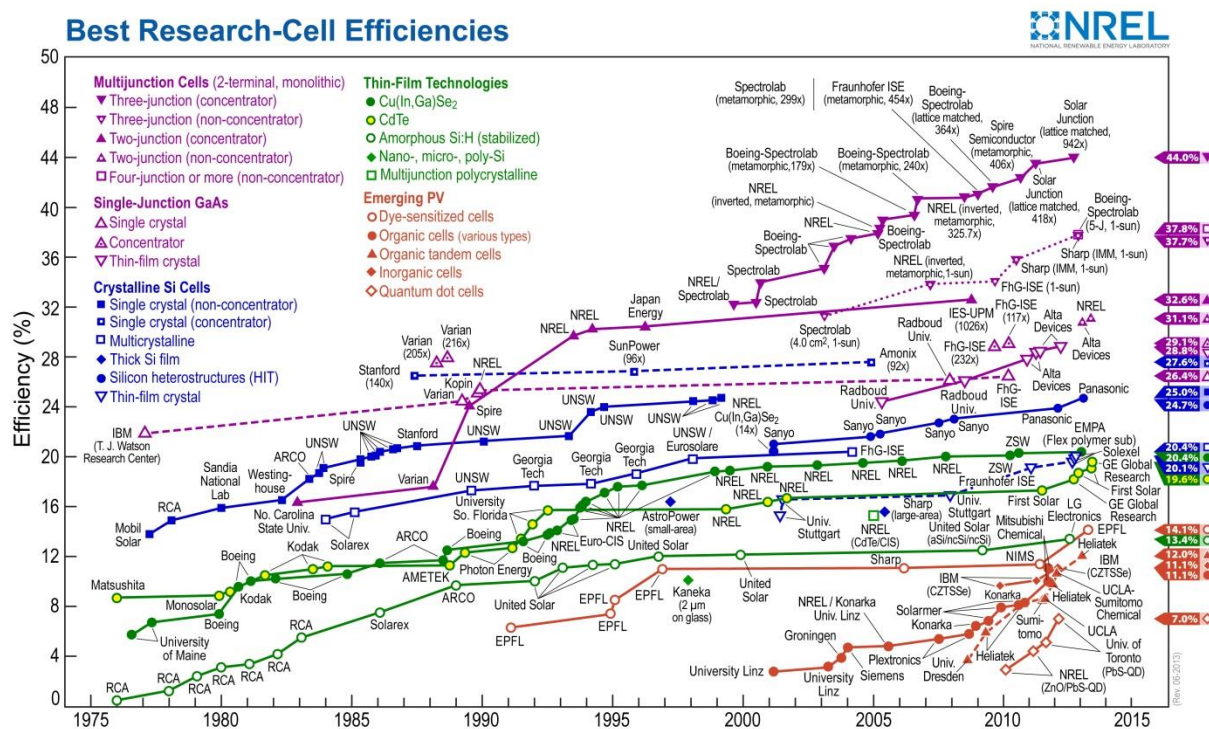
Figure 1.3 Best research-cell efficiencies.[4] Organic solar cells feature a steep increase to now 12.0% for a tandem device architecture.

1.1   Organic Solar Cells

Driven by the development of new organic semiconductors[5-6] and the implementation of multijunction concepts[7] organic solar cells have reached impressive power conversion efficiencies. Due to their delocalized π-electrons the absorption coefficient of organic semiconductors is very high, leading to sufficient light absorption within a few hundreds of nanometres and thus low material consumption.[8]

Due to the low dielectric constant of organic materials photogenerated charge carriers are exposed to strong Coulomb forces. Efficient separation of electrons and holes therefore requires an additional driving force, and transport over distances of at least 100 nm is only effective if electrons and holes are spatially separated. The energetic driving force for separation of the initial bound state can be gained through a heterojunction of two materials with different energy levels. If a type II junction is formed, i.e. the HOMO and LUMO of the one material are higher in energy than the

corresponding levels of the complementary semiconductor, holes will be transferred to one material (the donor) and electrons to the other (the acceptor). The strongly bound electron-hole pair, a singlet exciton, has a lifetime of less than 1 ns. Therefore its diffusion length is on the order of a few nanometres, which is much less than the absorption length. Significant improvements in photocurrent were achieved by creating an extended heterojunction throughout the volume of the active layer (Figure 1.4). These bulk heterojunctions are typically created through spontaneous de-mixing of a solution into donor-rich and acceptor-rich domains. Control of this phase separation to form domains of adequate dimensions and high phase purity and the formation of a bi-continuous network to allow holes and electrons to be collected with high quantum yield are important optimisation parameters in device fabrication.

1.1.1   Photogeneration of charge carriers in organic solar cells
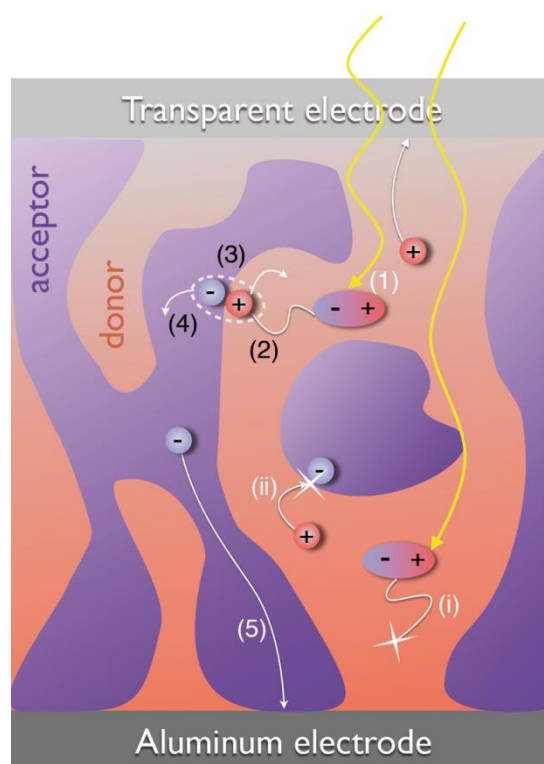
Figure 1.4 The processes involved in charge carrier generation in an organic solar cell.[9] (1) Incoming light is absorbed in both constituents of the donor-acceptor blend, generating singlet

excitons. These strongly bound states have to (2) diffuse to a donor-acceptor interface. (i) If they do not reach the junction within their lifetime, they will recombine, partly by emitting photoluminescence. (3) Ultrafast charge transfer occurs, after which the electron resides on the acceptor phase whereas the hole is on the donor material. This electron-hole pair may still be bound, requiring a (4) polaron pair dissociation step, although direct generation of charge carriers from singlet excitons is also reported in the literature. (5) The separated charge carriers are transported to the respective electrodes. They may (ii) recombine nongeminately, otherwise they are extracted at the electrodes, leading to the photocurrent.

In bulk heterojunction cells the donor as well as the acceptor materials can absorb incident photons. Conjugated polymers or oligomers, which are mostly used as the donor phase, have high absorption coefficients and moderate band gaps of 1.5-2.0 eV. While C_{60}-based acceptors have low absorption coefficients in the visible range, the absorption by the fullerene phase can be greatly enhanced through the use of C_{70} derivatives instead.

In the following we will discuss the processes involved in photogeneration assuming that the photon is absorbed in the donor polymer, however, the same considerations apply also for photons absorbed in the acceptor phase (Figure 1.4).

As the dielectric constant of organic materials is low, the screening of electric fields is weak. Therefore, the Coulomb interaction between electrons and holes is much stronger than in most inorganic semiconductors. Similarly, the binding energy of a singlet exciton is much higher (typically 400-700 meV), which is by far larger than thermal energy at room temperature. Consequently an additional energetic driving force is required to generate free charge carriers from an exciton. This extra energy can be gained from the energy offset at a heterojunction. If the energy alignment is favourable for charge transfer, the electron will be injected into the acceptor phase, potentially forming a still bound polaron pair, also referred to as the charge transfer state. The microstructure of the photoactive blend is of crucial importance for the injection efficiency. Since the exciton is an electrically neutral state, it will not be affected by external or built-in fields and thus the migration to a donor-acceptor interface relies on diffusion. If the exciton does not reach the heterojunction within its lifetime, it will recombine and with a certain

probability emit its energy as photoluminescence. Depending on the mobility and lifetime of the exciton a domain size of 10-30 nm is typically required for efficient injection.

After successful singlet exciton dissociation, the charge carriers now located at both sides of the interface either are still bound by Coulomb forces, forming a polaron pair or charge transfer exciton, or have transformed into free polarons directly. There is an ongoing discussion in the literature whether the main pathway for charge carrier generation is via charge transfer states, which then dissociate with near unity efficiency, or via direct generation of free charge carriers.
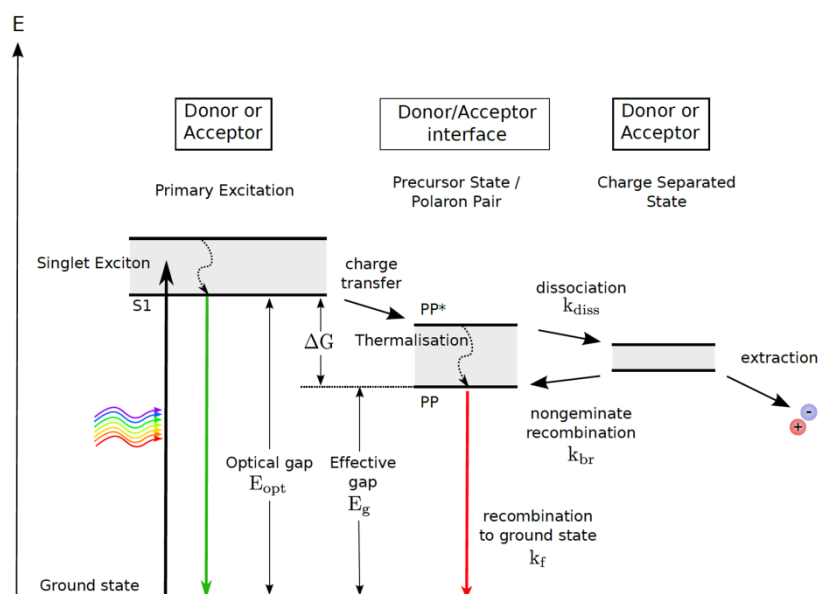
Figure 1.5   Energy scheme of the states and processes involved in charge carrier generation and recombination.[9]

Figure 1.5 describes the processes discussed above on an energy scale. Thermalisation losses and the energy that is lost upon charge transfer lead to a significant reduction in energy between the optical gap and the voltage the solar cell could output even without losses during charge transport. Thus the open-circuit voltage of efficient organic solar cells is about 800 mV lower than their optical gap.[10]

Photogenerated charge carriers have to migrate through the intermixed bulk heterojunction to be collected at their respective electrodes. This process can be

facilitated by a built-in or external electric field. If the charge transport at a given potential takes longer than the lifetime of the respective charge carriers, non-geminate recombination between a hole in the donor and an electron in the acceptor phase will take place. Especially in finely intermixed or disordered systems this represents a major loss mechanism and causes low photocurrents and fill factors.

1.1.2 Materials for organic photovoltaics

Progress in organic photovoltaics is mainly driven by the development of new donor and acceptor materials. A selection of successful donor and acceptor materials is shown in Figure 1.6. Early examples of conductive polymers that were applied in bulk heterojunction solar cells were poly(phenylene vinylene) (PPV) derivatives.[11] The invention of [6,6]-phenyl C_{61} butyric acid methyl ester as a well-soluble electron acceptor and advances in processing of the photoactive blend led to improved efficiencies of up to 2.5%.[12-13] The semi-crystalline regioregular poly(3-hexylthiophene) (P3HT) was found to offer better light absorption and, due to its well-defined packing, improved charge carrier transport, which led to the first organic solar cells with around 5% efficiency.[14-15] Although more recent polymers show higher efficiencies, P3HT is still widely used as a reference material. The search for organic materials that could provide better light absorption in the near infrared region led to the development of polymers and oligomers with alternating electron-rich and electron-deficient units, which are electronically coupled via a conjugated π-system. These donor-acceptor materials represent the current state of the art in OPV and are tuned either to absorb in a very broad range (e.g. PCPDTBT) or deliver a high voltage in combination with PCBM (e.g. PCDTBT). Absorption spectra of these polymers are depicted in Figure 1.7. Fine-tuning of the device architecture, processing conditions and contact layers have boosted device efficiencies to well above 8%.[16-20]

MEH-PPV

P3HT

PCBM

PCPDTBT

PCDTBT

PTB7

R = ethylhexyl
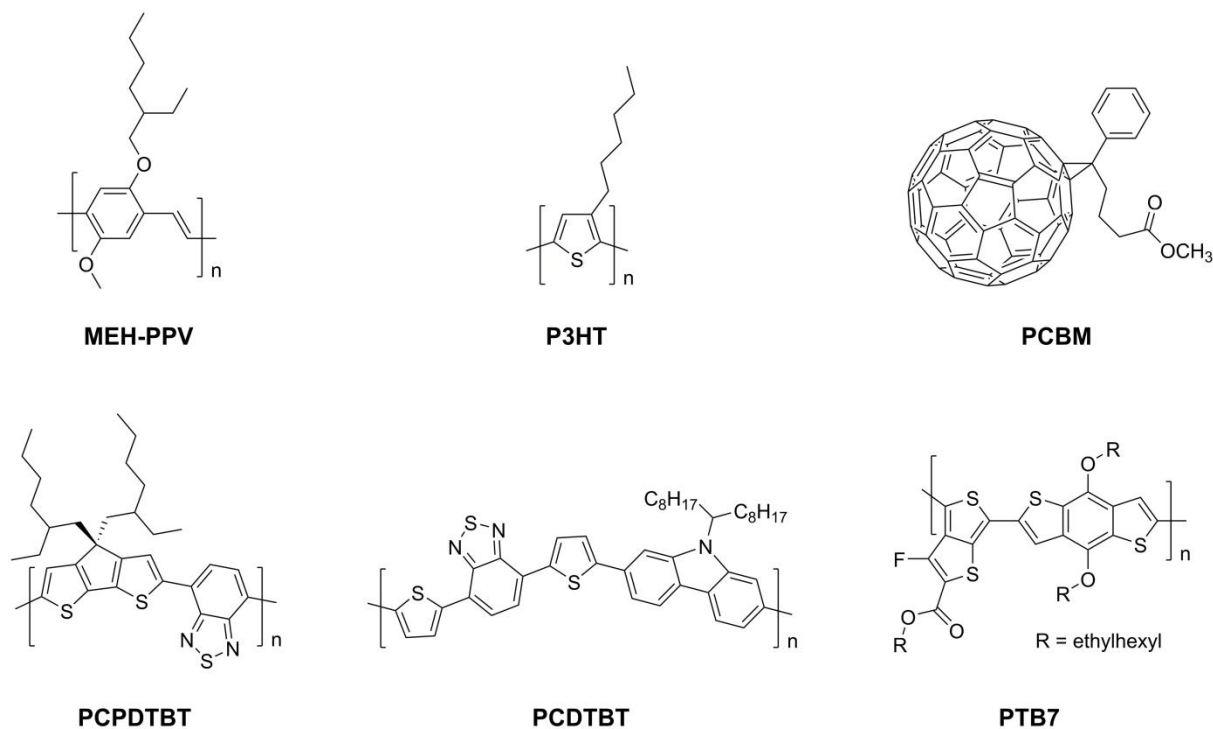
Figure 1.6 Chemical structures of selected donor and acceptor materials used in solution-processed organic photovoltaics.
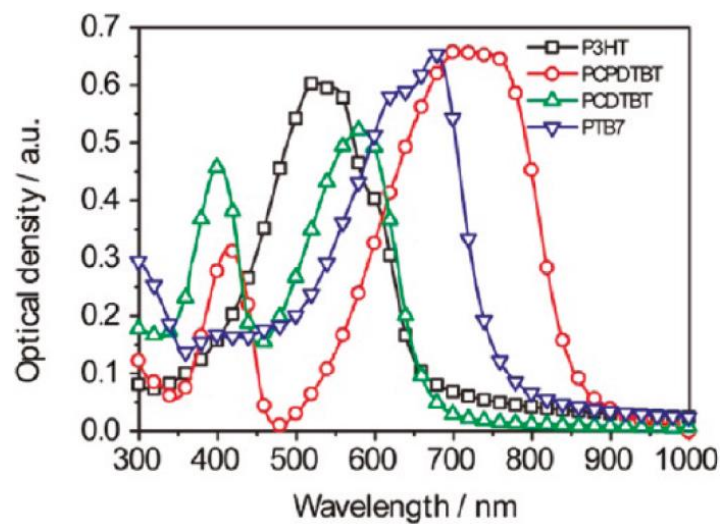
Figure 1.7 Absorption spectra of polymers that are commonly used in bulk heterojunction cells.[21]

1.2   Covalent Organic Frameworks

A recently developed class of ordered organic materials, covalent organic fameworks (COFs), has attracted considerable attention in the scientific community. COFs are crystalline and highly porous materials that are assembled from covalently bound molecular building blocks. Periodically ordered networks can be obtained if multifunctional linkers are connected in a reaction that offers a certain degree of reversibility and thereby provides a self-repair mechanism for the growing crystal. One of the most prominent patterns in COFs is the condensation between a trigonal hexaol and a linear diboronic acid, leading to the formation of sheets with a hexagonal pattern (Figure 1.8a).[22]
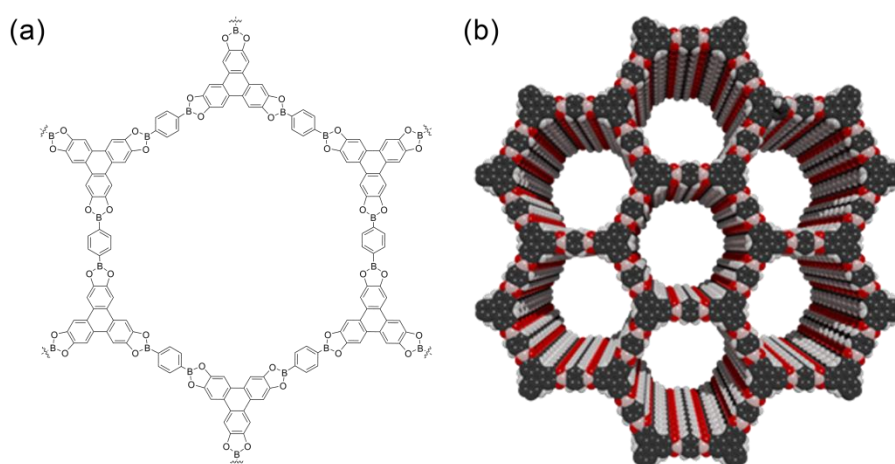
Figure 1.8 Molecular structure of the 2D sheets in COF-5 (a) and illustration of the three-dimensional structure of the COF (b).

A three-dimensional crystal is formed upon π-stacking of these 2D sheets. Most known COFs crystallise with an eclipsed arrangement of the layers, i.e. identical units stack on top of each other (Figure 1.8b). Deviations from this idealized stacking scheme have been addressed, regarding their implications on electronic properties.[23-24]

The COF concept offers great structural and functional flexibility. The pore size and pore geometry can be tuned via the selection of the molecular building blocks.[25-26] An aspect that makes COFs even more interesting for OVP research is the broad choice of functionality, which can be incorporated into the network by choosing adequate

building blocks. Several fluorescent COFs have been reported.[27-28] The optoelectronic properties of porphyrin- and phthalocyanine-containing COFs have been addressed in a number of publications.[29-30] Some of these materials were claimed to be n- or p-type semiconductors, however, with extremely low conductivities.[31-32] We have recently developed a thienothiophene-based COF which is capable of photoinduced charge transfer to an electron acceptor located inside the COF pores.[28] We used this combination of materials to construct the first COF-based photovoltaic device. The optoelectronic properties of several COFs and their capabilities of undergoing photoinduced charge transfer will be discussed in more detail in this thesis.

1.3 References

[1]   http://en.wikipedia.org/wiki/File:Breakdown_of_the_incoming_solar_energy.svg

[2]   http://en.wikipedia.org/wiki/File:Solar_land_area.png

[3]   http://www.heliatek.com/

[4]   http://www.nrel.gov/ncpv/

[5]   Y. Liang, Z. Xu, J. Xia, S.-T. Tsai, Y. Wu, G. Li, C. Ray, L. Yu, *Adv. Mater.* **2010**, *22*, E135-E138.

[6]   W. Ma, C. Yang, X. Gong, K. Lee, A. J. Heeger, *Adv. Funct. Mater.* **2005**, *15*, 1617-1622.

[7]   W. Li, A. Furlan, K. H. Hendriks, M. M. Wienk, R. A. J. Janssen, *J. Am. Chem. Soc.* **2013**, *135*, 5529-5532.

[8]   G. Dennler, M. C. Scharber, C. J. Brabec, *Adv. Mater.* **2009**, *21*, 1323-1338.

[9]   C. Deibel, A. Baumann, V. Dyakonov, in *Physics of Organic Semiconductors*.

[10]   M. A. Faist, T. Kirchartz, W. Gong, R. S. Ashraf, I. McCulloch, J. C. de Mello, N. J. Ekins-Daukes, D. D. C. Bradley, J. Nelson, *J. Am. Chem. Soc.* **2012**, *134*, 685-692.

[11]   N. S. Sariciftci, L. Smilowitz, A. J. Heeger, F. Wudl, *Science* **1992**, *258*, 1474-1476.

[12]   G. Yu, J. Gao, J. C. Hummelen, F. Wudl, A. J. Heeger, *Science* **1995**, *270*, 1789-1791.

[13]   S. E. Shaheen, C. J. Brabec, N. S. Sariciftci, *Appl. Phys. Lett.* **2001**, *78*, 841-843.

[14]   F. Padinger, R. S. Rittberger, N. S. Sariciftci, *Adv. Funct. Mater.* **2003**, *13*, 85-88.

[15]   M. D. Irwin, D. B. Buchholz, A. W. Hains, R. P. H. Chang, T. J. Marks, *PNAS* **2008**, *105*, 2783-2787.

[16]   J. Peet, J. Y. Kim, N. E. Coates, W. L. Ma, D. Moses, A. J. Heeger, G. C. Bazan, *Nat. Mater.* **2007**, *6*, 497-500.

[17]   S. H. Park, A. Roy, S. Beaupré, S. Cho, N. Coates, J. S. Moon, D. Moses, M. Leclerc, K. Lee, A. J. Heeger, *Nat. Photon.* **2009**, *3*, 297-303.

[18]   Z. He, C. Zhong, X. Huang, W.-Y. Wong, H. Wu, L. Chen, S. Su, Y. Cao, *Adv. Mater.* **2011**, *23*, 4636-4643.

[19]   Z. He, C. Zhong, S. Su, M. Xu, H. Wu, Y. Cao, *Nat. Photon.* **2012**, *6*, 591-595.

[20]   S. Chen, C. E. Small, C. M. Amb, J. Subbiah, T.-H. Lai, S.-W. Tsang, J. R. Manders, J. R. Reynolds, F. So, *Adv. Energy Mater.* **2012**, *2*, 1333-1337.

[21]   T. J. K. Brenner, Z. Li, C. R. McNeill, *J. Phys. Chem. C* **2011**, *115*, 22075-22883.

[22]   A. P. Côte, A. I. Benin, N. W. Ockwig, M. O'Keeffe, A. J. Matzger, O. M. Yaghi, *Science* **2005**, *310*, 1166-1170.

[23]   S. Patwardhan, A. A. Kocherzhenko, F. C. Grozema, L. D. A. Siebbeles, *J. Phys. Chem. C* **2011**, *115*, 11768-11772.

[24]   E. L. Spitler, B. T. Koo, J. L. Novotney, J. W. Colson, F. J. Uribe-Romo, G. D. Gutierrez, P. Clancy, W. R. Dichtel, *J. Am. Chem. Soc.* **2011**, *133*, 19416-19421.

[25]   M. Dogru, A. Sonnauer, A. Gavryushin, P. Knochel, T. Bein, *Chem. Commun.* **2011**, *47*, 1707-1709.

[26]   E. L. Spitler, J. W. Colson, F. J. Uribe-Romo, A. R. Woll, M. R. Giovino, A. Saldivar, W. R. Dichtel, *Angew. Chem. Int. Ed.* **2012**, *51*, 2623-2627.

[27]   S. Wan, J. Guo, J. Kim, H. Ihee, D. Jiang, *Angew. Chem. Int. Ed.* **2008**, *47*, 8826-8830.

[28]   M. Dogru, M. Handloser, F. Auras, T. Kunz, D. Medina, A. Hartschuh, P. Knochel, T. Bein, *Angew. Chem. Int. Ed.* **2013**, *52*, 2920-2924.

[29]   S. Jin, X. Ding, X. Feng, M. Supur, K. Furukawa, S. Takahashi, M. Addicoat, M. E. El-Khouly, T. Nakamura, S. Irle, S. Fukuzumi, A. Nagai, D. Jiang, *Angew. Chem. Int. Ed.* **2013**, *52*, 2017-2021.

[30]   A. Nagai, X. Chen, X. Feng, X. Ding, Z. Guo, D. Jiang, *Angew. Chem. Int. Ed.* **2013**, *52*, 3770-3774.

[31]   X. Ding, J. Guo, X. Feng, Y. Honsho, J. Guo, S. Seki, P. Maitarad, A. Saeki, S. Nagase, D. Jiang, *Angew. Chem. Int. Ed.* **2011**, *50*, 1289-1293.

[32]   X. Ding, L. Chen, Y. Honsho, X. Feng, O. Saengsawang, J. Guo, A. Saeki, S. Seki, S. Irle, S. Nagase, V. Parasuk, D. Jiang, *J. Am. Chem. Soc.* **2011**, *133*, 14510-14513.

12

2 Characterisation Techniques

2.1 UV-VIS Spectroscopy

UV-Vis spectroscopy can be used for investigating electronic transitions from the ground state to a broad range of excited states. This information can be used for qualitative and quantitative determination of the absorbing species in liquid and solid samples. Spectral shifts and peak broadening can provide valuable insights into interactions and degree of ordering of absorbing molecules in solid-state samples.[1]

In a dilute solution without interaction of the chromophores among each other or with the solvent the absorbance A at a certain wavelength, defined as

$$A(\lambda) = -log \frac{I(\lambda)}{I_0(\lambda)}$$

is related to the concentration of the absorbing species via the Lambert-Beer law:

$$A(\lambda) = \varepsilon(\lambda)\, c\, L$$

I is the measured intensity, I_0 the intensity without sample, $\varepsilon(\lambda)$ is the extinction coefficient, c the concentration and L the layer thickness.

UV-Vis spectroscopy is a standard tool for the characterisation of photoactive thin films. However, in many cases one would like to obtain not only qualitative information about the absorbing species, but to quantify the amount of light that is absorbed in the active layer. As thin films are commonly supported on a transparent substrate, light will be reflected from the air-substrate, the substrate-sample and the sample-air interfaces. Devices usually comprise stacks of several conductive and charge selective layers on a glass or polymer substrate and reflective metal top contacts. Each interface will reflect a fraction of the incident light. Additionally, a sequence of nanometer-sized layers with different refractive indices will cause complex interference phenomena, such that the amount of light that is available in the active layer depends on the thickness of all layers in the device. The Lambert-Beer law cannot be applied in these cases and a thicker active layer might even decrease its total absorption.[2] Reliable determination of the absorbance has been achieved through optical modelling based on the optical constants

of each individual layer[3] or measurements with an integrating sphere and a suitable reference.[4] The following procedure was found to produce reliable results for many types of thin film samples.

Scattering, but translucent samples (e.g. films on SnO₂:F, mesoporous TiO₂ films, hematite thin films):

- Transmission (*%T*) measurements of the sample and the reference. The sample has to be positioned just inside the sphere at the transmission port, such that light that is scattered towards the edges of the substrate is collected as well. The beam diameter should be smaller than the sample.
- Reflectance (*%R*) measurement of the sample and of the reference. The sample should be positioned outside the integrating sphere, such that light that is scattered towards the edges of the substrate is not collected this time.

The reference should be a substrate of the same size with all layers except the active layer. For the instrument baseline air (100% *T*) and a Spectralon white standard (*%R*) are used.

A convenient procedure to determine the active layer absorbance from these measurements has been proposed by Klahr *et. al.*[5]

We assume that all light is either reflected, transmitted, or absorbed.

$$\%T + \%R + \%A = 1$$

From the above four measurements percentage absorbance *%A* of the sample and the reference can be obtained. This is converted into absorbance units via the relation

$$A = -log(1 - \%A)$$

We can assume that interference effects play only a minor role as long as the samples (or the substrate) are scattering enough, such that

$$A_{sample} = A_{ref} + A_{film}$$

$$A_{film} = A_{sample} - A_{ref}$$

Thin film solar cells (non-scattering)

The active layer absorbance in thin film solar cells can be determined by a similar method as described above with the following modifications:

- The reflective metal top contact can be assumed as non-transparent. Therefore only the two measurements in reflection geometry are necessary.
- Due to interference the light intensity and thus the absorption in each layer depends on the optical constants and layer thickness of all layers. The reference therefore has to consist of exactly the same device structure, except for the active layer, which has to be replaced by a transparent layer of the same thickness and refractive index. Poly(methyl methacrylate) (PMMA) can be applied as reference material when measuring the absorbance of polymer:fullerene films.

2.2 Photoluminescence Spectroscopy

When exciting a chromophore or an electron in a semiconductor, it will relax to its ground state after a certain time, while the excess energy is released as phonons or photons. Following optical excitation the excited state rapidly thermalizes to its vibrational ground state, whereas the large energy difference between the excited state and the ground state is likely to be released as a photon. In addition to radiative transition directly to the ground state, the energy can be released step-wise through competing processes, like intersystem crossing, or charge transfer to an acceptor molecule.

Detection of the emitted photons can provide valuable information about the decay mechanisms of the optically excited chromophore and thus the effectiveness of processes like charge transfer.

A detailed description of the experimental setup is given in Chapter 9.2.

2.3   Basic Photovoltaic Characterisation: Current-Voltage Characteristics

Solar cells are commonly rated according to their photovoltaic conversion efficiency (PCE) measured under well-defined conditions. For terrestrial use the ASTM G173-03 air mass 1.5 global (AM1.5G) spectrum at a total light intensity of 100 mW cm^{-2} is the current standard.[6] This spectrum includes absorption and scattering by the atmosphere and hemispheric illumination by diffuse light. Laboratory solar simulators typically use a xenon lamp and appropriate filters to achieve a spectral output that closely resembles this AM1.5G spectrum.

The PCE of a test device can be obtained by measuring its current-voltage (IV) characteristics under 100 mW cm^{-2} AM1.5G illumination (also referred to as 1 sun). A typical IV-curve measured for an inverted bulk heterojunction solar cell is shown in Figure 2.1. From this curve one can extract the basic parameters:

The *open-circuit voltage* (V_{OC}) is the voltage at which the current through the cell is 0. V_{OC} is mainly determined by the difference between the quasi-Fermi levels in the donor and acceptor phase, although in many cases the contacts to the active layer might also play a role.[7]

The current through the cell at no external bias is called the *short circuit current density* (J_{SC}). J_{SC} depends on the optical absorption of the cell, the ability to create free charge carriers from absorbed photons, and the transport of these charge carriers to the electrodes.

The maximum power the cell can generate, P_{max}, and the corresponding V_{max} and J_{max} define the *photovoltaic conversion efficiency* (PCE) via the relation

$$PCE = \frac{P_{max}}{P_{in}} = \frac{V_{max} J_{max}}{P_{in}}$$

where P_{in} is the power of the incident light.

As a measure of how good the maximum performance of a solar cell is with respect to its capability of creating current at no applied potential and voltage at open circuit, the *fill factor* (*FF*) is introduced. It is defined as

$$FF = \frac{V_{max} \, J_{max}}{V_{OC} \, J_{SC}} = \frac{P_{max}}{V_{OC} \, J_{SC}}$$

i.e. the ratio between the light blue and the dark blue rectangle in Figure 2.1. The fill factor is a measure for the ability of a device to support efficient charge carrier generation and collection under forward bias. Good organic solar cells have fill factors of around 70%,[8] while single-crystalline silicon or III-V cells can even reach about 85%.[9]
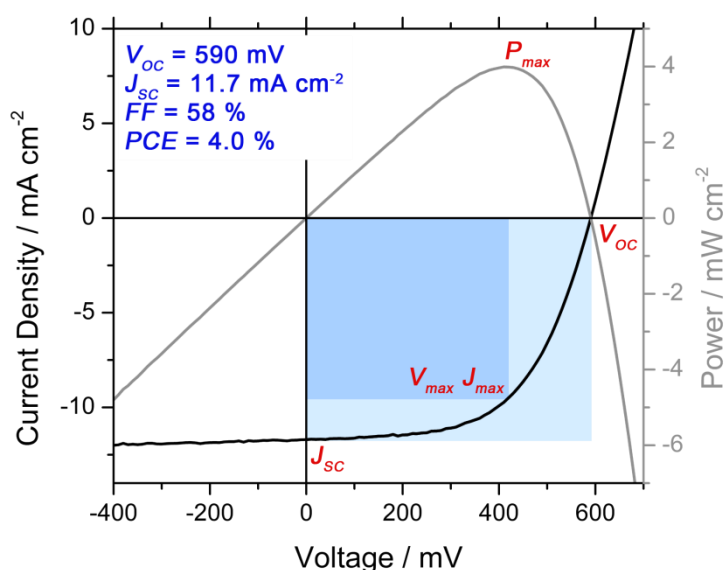
Figure 2.1 *J-V* characteristics of an inverted P3HT:PCBM bulk heterojunction cell.

As discussed in Chapter 1.1, the major loss mechanisms present in an organic solar cell are voltage- or current-dependent. Hence the shape of an IV-curve can provide first information about losses in a device sample. A set of light-intensity dependent IV-curves obtained for a regular TT-COF:[60]PCBM device is displayed in Figure 2.2a.[10]

The steep slope around zero applied bias indicates that the built-in potential is not sufficient for efficient polaron pair dissociation and/or charge collection. As expected these processes become more efficient at reverse bias and hence the photocurrent increases.

If one plots the short circuit current versus the light intensity (Figure 2.2b), an ideal solar cell without charge transport limitations and recombination of polarons would

exhibit a linear behaviour. A sub-linear behaviour indicates losses through recombination of (already separated) hole polarons in the donor phase with electron polarons in the acceptor phase before they can reach the electrodes. This recombination mechanism depends on the number of charge carriers in the device and hence on the light intensity.

The slope at high forward bias is governed by the ohmic resistance of the device, since the forward current through the diode rises exponentially. A high series resistance leads to an additional reduction of the fill factor and consequently reduction in cell performance.[11]
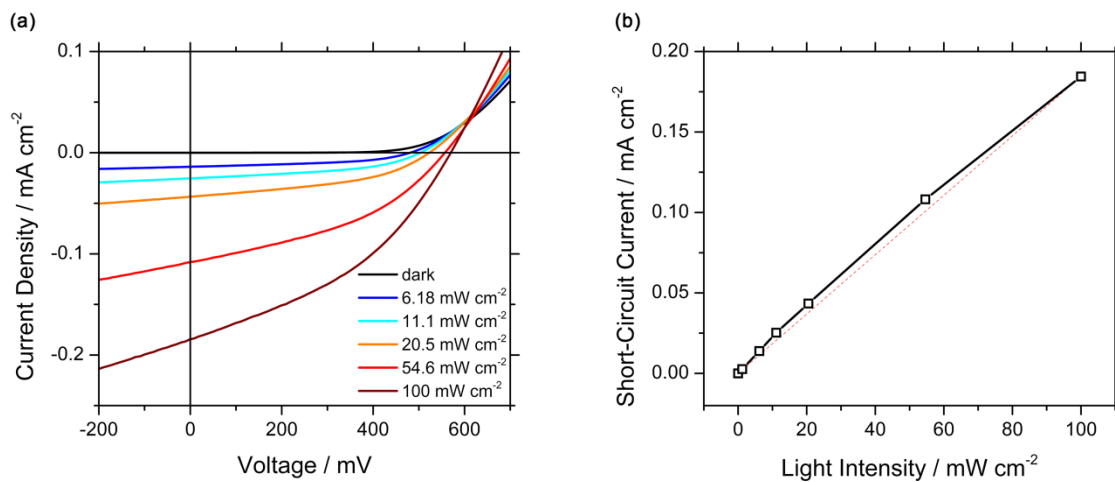
Figure 2.2 Light-intensity dependent *J-V* curves of a TT-COF:PCBM device (a), and the short-circuit current plotted vs. light intensity (b). The dotted red line would be the ideal, linear behaviour.

2.4 External/Internal Quantum Efficiency

As discussed in Chapter 1.1 the process of current generation can be split into several steps, where the overall quantum efficiency is the product of the efficiencies of each step. In many cases one would like to analyse not only the amount of current generated under white light illumination, but to gain additional insights by measuring the current response of a device in a spectrally resolved way.

The *external quantum efficiency* (EQE) is defined as the number of collected electrons per incident photon at the respective wavelength, and can be expressed as

$$EQE(\lambda) = \frac{n_e(\lambda)}{n_{ph}(\lambda)} = \eta_{abs}(\lambda) \times \eta_{ED} \times \eta_{PD}(V) \times \eta_{coll}(n_e n_h)$$

where η_{abs} is the absorption in the active layer, η_{ED} the efficiency for exciton diffusion and dissociation, η_{PD} the polaron dissociation efficiency, and η_{coll} the collection efficiency. As discussed above, η_{ED} is independent of the applied bias, because the exciton is a neutral quasi-particle, whereas η_{CT} depends on the built-in and the external field. η_{coll} is contingent on the number of charge carriers in the active layer.

The *internal quantum efficiency* relates the photons absorbed by the active layer(s) to the collected current. This requires exact determination of the absorbance of the active layer *in the photovoltaic device*. Methods how this can be achieved are discussed in Chapter 2.1.

The EQE is measured by directing a beam of monochromatic light, obtained from a xenon lamp and a monochromator with order sorting filters, onto the sample, measuring its current response and relating this to the response of a calibrated reference diode. For better signal to noise ratio the monochromatic beam is modulated by an optical chopper and the signal is detected via a lock-in amplifier, which is locked to this modulation frequency. Lamp drift is corrected through monitoring the monochromatic light intensity during the measurement with a photodiode and a second lock-in amplifier. Since the response of most solar cells is different at high light intensities, the most reliable EQE spectra are measured using a white light bias. This way the cell is set to operating conditions that are similar to full sun illumination while the monochromatic light only adds a small perturbation. A detailed description of the experimental setup is given in Chapter 9.1.

EQE is a powerful measurement technique for obtaining information about the photoactive species in the sample. The shape of the spectrum is mainly governed by the absorption spectrum of the active components, which thus can be unambiguously identified. Moreover, in cases where the device comprises highly active and less active domains, e.g. well-intermixed polymer/fullerene domains and large fullerene

agglomerates[12] or amorphous and crystalline polymer regions,[13] the EQE spectrum is more sensitive to the photoactive fraction, whereas UV-Vis spectroscopy probes the entire film. Measuring the EQE under applied bias (forward or reverse), or with front- and back-side illumination can be used for mechanistic studies[14] and for probing charge transport behaviour.[15]

2.5 Scanning Electron Microscopy

Electron microscopy is a powerful technique to obtain structural and compositional information on the nanoscale. In scanning electron microscopy (SEM) a focused electron beam, typically generated by a field emission gun, is scanned across the sample. The interactions of an electron beam with a thick sample are depicted in Figure 2.3. The strong interaction of electrons with matter leads to rapid deceleration and absorption of the incident electrons, such that only a small volume of the sample (depending on the acceleration voltage, typically in the order of a few μm^3) is perturbed.

Among the signals that are used in a typical SEM secondary electrons offer the best spatial resolution and surface sensitivity. Due to their low energy only secondary electrons created very close to the sample surface can be emitted from the sample and be detected. The emission of secondary electrons is more pronounced at sharp edges, thus the morphology of a sample leads to an image contrast in the resulting SEM micrograph.

Backscattered electrons have higher energy and thus can originate from a larger volume (blue) and thus offer systematically lower spatial resolution than secondary electrons. However, the yield of backscattered electrons depends strongly on the atomic number and density of the sample, such that different materials or phases can be visualised.

Characteristic X-rays are a common way of analysing sample composition in energy-dispersive or wavelength-dispersive X-ray spectroscopy (EDX and WDX). Provided that the primary electrons have sufficient energy to excite atomic transitions, EDX permits simultaneous analysis of all elements present in the sample.
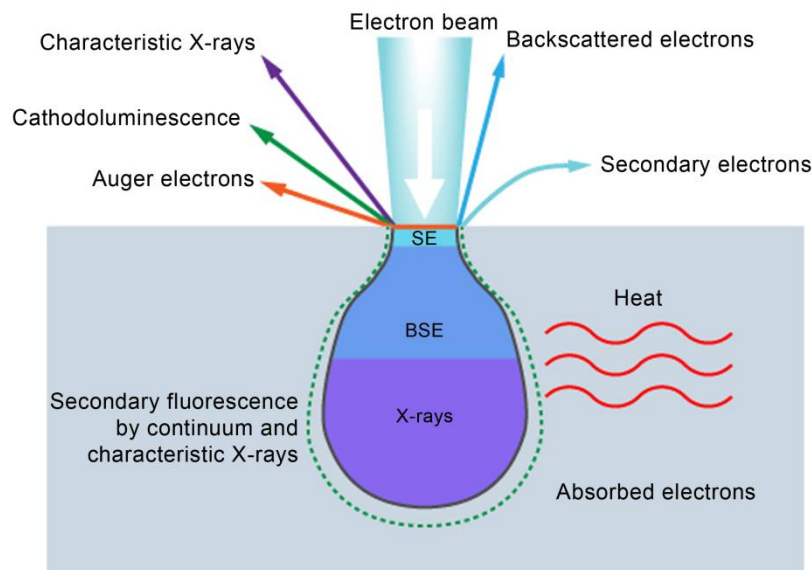
Figure 2.3 Interactions of an electron beam with a thick sample.[16]

2.6   References

[1]   T. C. Monson, M. T. Lloyd, D. C. Olson, Y.-J. Lee, J. W. P. Hsu, *Adv. Mater.* **2008**, *20*, 4755-4759.

[2]   G. Dennler, M. C. Scharber, C. J. Brabec, *Adv. Mater.* **2009**, *21*, 1323-1338.

[3]   G. F. Burkhard, E. T. Hoke, M. D. McGehee, *Adv. Mater.* **2010**, *22*, 3293-3297.

[4]   H. J. Snaith, C. Ducati, *Nano Lett.* **2010**, *10*, 1259-1265.

[5]   B. M. Klahr, A. B. F. Martinson, T. W. Hamann, *Langmuir* **2011**, *27*, 461-468.

[6]   http://rredc.nrel.gov/solar/spectra/am1.5

[7]   R. Steim, F. R. Kogler, C. J. Brabec, *J. Mater. Chem.* **2010**, *20*, 2499-2512.

[8]   Z. He, C. Zhong, S. Su, M. Xu, H. Wu, Y. Cao, *Nat. Photon.* **2012**, *6*, 591-595.

[9]   http://www.ise.fraunhofer.de/en/press-and-media/press-releases/presseinformationen-2013/43.6-four-junction-solar-cell-under-concentrated-sunlight

[10]   M. Dogru, M. Handloser, F. Auras, T. Kunz, D. Medina, A. Hartschuh, P. Knochel, T. Bein, *Angew. Chem. Int. Ed.* **2013**, *52*, 2920-2924.

[11]   J. R. Sites, P. H. Mauk, *Solar Cells* **1989**, *27*, 411-417.

[12]   S. J. Lou, J. M. Szarko, T. Xu, T. J. Marks, L. X. Chen, *J. Am. Chem. Soc.* **2011**, *133*, 20661-20663.

[13]   M. T. Lloyd, R. P. Prasankumar, M. B. Sinclair, A. C. Mayer, D. C. Olson, J. W. P. Hsu, *J. Mater. Chem.* **2009**, *19*, 4609-4614.

[14]   E. T. Hoke, K. Vandewal, J. A. Bartelt, W. R. Mateker, J. D. Douglas, R. Noriega, K. R. Graham, J. M. J. Fréchet, A. Salleo, M. D. McGehee, *Adv. Energy Mater.* **2013**, *3*, 220-230.

[15]   J. Halme, G. Boschloo, A. Hagfeldt, P. Lund, *J. Phys. Chem. C* **2008**, *112*, 5623-5637.

[16]   http://www.ammrf.org.au/myscope/sem/background/concepts

3 Highly Oriented Zinc Oxide Nanowire Arrays for Hybrid Inorganic-Organic Solar Cells

3.1 Introduction

Excitonic solar cells, including organic, hybrid, and dye-sensitized solar cells, are promising candidates for inexpensive, large-scale solar energy conversion, as they have proven to be efficient light harvesters under diffuse illumination conditions. While most dye-sensitized and metal oxide/polymer hybrid solar cells are based on a nanocrystalline titanium dioxide film with high surface area, the development of scaffolds that could offer improved transport properties and a better accessible pore structure is subject of ongoing research. One-dimensional single-crystalline structures might offer superior charge carrier transport compared to the random diffusion in a typical TiO$_2$ film. Single crystalline nanowires of zinc oxide have been shown to possess orders of magnitude higher electron mobilities than polycrystalline films.[1-2] Oriented nanowire arrays feature open channels perpendicular to the film surface, which facilitate infiltration with polymer- or small molecule-based hole transporters.[3-4]

Zinc oxide nanowire arrays have been extensively studied as photoanodes in liquid electrolyte and solid-state dye-sensitized solar cells and polymer/metal oxide hybrid solar cells.[1, 5-8] However, in many cases the zinc oxide featured a high density of defect states, which was found to be inherent to the method of preparation.[9-11] Thus the nanowire surface required additional passivation to facilitate electron injection and charge separation.[12-13]

Among the synthetic approaches for preparing ordered zinc oxide nanowire arrays are hydrothermal methods, electrochemical deposition, and deposition from the gas phase.[14-17] Solution-based methods offer a cost-effective low-temperature approach that is applicable to a variety of substrates.[18] Most synthetic protocols for aqueous growth use a two-step method consisting of the deposition of pre-formed ZnO nanocrystals on the substrates as seeds, followed by epitaxial growth of these seeds into nanowires. The size, density and orientation of the seeds thus directly translate into the morphological features of the resulting nanowire arrays. Perfect vertical nanowire orientation can be obtained on suitable single-crystalline substrates[19] or via deposition

of textured seeds.[17] In the latter case geometrical selection was found to sort out the small fraction of misaligned nanowires in an early stage of nanowire growth, leading to an improvement of the c-axis orientation as the growth proceeds.[20]

Depending on the exact synthetic method used for hydrothermal nanowire growth, nanowires of different length, diameter, aspect ratio, and tip shape can be obtained.[21-24] It has been found that the composition of the growth solution greatly impacts the defect density in the nanowires and thus electronic properties, such as photoluminescence, charge carrier concentration, mobility, and conductivity.[25]

Here we present a synthetic method for the growth of highly oriented and homogeneous zinc oxide nanowire arrays, which allows us to tune the nanowire morphology via the pH of the growth solution while keeping all other parameters constant. Our method thus provides a platform for studying the influence of the morphology and the OH⁻ concentration during growth, decoupled from other synthetic parameters, on the device performance in polymer/nanowire hybrid solar cells.

3.2 Results and Discussion

Thermal decomposition of a zinc acetate precursor is a widely used method for decorating various substrates with small, textured seeds.[17] The initially deposited zinc salt is converted into a polycrystalline zinc oxide film during calcination, which provides the nuclei for subsequent epitaxial nanowire growth.

3.2.1 pH-Dependent nanowire morphologies

The first developed hydrothermal methods for nanowire growth typically used a zinc salt and an amine, for example hexamethylenetetramine (HMT). Although these methods are suitable for growing well-oriented nanowires, the unavoidable formation of bulk precipitate can reduce reproducibility and film quality. Especially for applications in polymer/nanowire hybrid solar cells, any adhering precipitate could short-circuit the cell and thereby cause device failure. Recently a synthetic method that avoids the formation of any precipitate in the bulk solution via complexation of zinc ions with

ammonia has been reported.[26] We extended this method to the growth of nanowires of different morphology and aspect ratio. We found that changes in the pH of the growth solution, realised via the introduction of an NH_3/NH_4^+ buffer, have a profound effect on the nanowire length, aspect ratio, and density (Figure 3.1). Our optimised solution consisted of 25 mM zinc nitrate, 12.5 mM HMT, 6 mM polyethylenimine (PEI), and 250-350 mM of the ammonia buffer. During the reaction HMT decomposes slowly into ammonia (thus forming OH^-) and formaldehyde. As each HMT molecule generates 4 OH^- ions, the 2:1 ratio of Zn^{2+} and HMT employed in our synthesis is the correct stoichiometric ratio and thus should ensure a constant pH while the nanowire growth proceeds. Indeed we observe a constant pH in the growth solution over several hours. PEI was found to bind selectively to the non-polar outer facets of the ZnO nanowires and thus reduce the growth rate in lateral direction, which results in higher achievable aspect ratios.[1] Additionally, PEI was reported to slow down the growth kinetics of nuclei that spontaneously form in the bulk solution, such that they dissolve again with high probability before reaching the critical radius for being thermodynamically stable.[26] Ammonia is known to be a good complexing agent for zinc ions and thereby reduces the concentration of free, reactive Zn^{2+} below the critical concentration for nucleation in the bulk phase. However, the high concentration of ammonia also increases the concentration of OH^- ions in the growth solution by more than an order of magnitude. Zinc oxide nanowires grown at high pH are known to possess a higher defect density, which is associated with oxygen vacancies and the incorporation of OH^- into the crystal lattice. These vacancies not only dramatically reduce the charge carrier mobility, but also have to be balanced by electrons for charge neutrality, which in turn leads to high n-type doping. We therefore modified the synthetic protocol by the addition of ammonium nitrate, which enables us to buffer the pH to a certain desired value without having to sacrifice the benefit of ammonia as a complexing agent. We can thus grow nanowire arrays of desired morphology or electronic properties that are completely free of adherent precipitate.

The nanowire arrays obtained at different pH are presented in Figure 3.1. The detailed composition of the NH_4NO_3/NH_4OH buffer and the resulting pH and nanowire length are summarized in Table 3.1. At low pH (a-c) the PEI binds strongly to the nanowire surface, promoting the growth of very high aspect ratio nanowires.[27] The PEI seems to become

less effective as the pH of the solution increases, such that the lateral growth becomes faster and the resulting nanowires are thicker. We also observe that the nanowire tips become increasingly sharp, which is a second indication for smaller differences in growth rate of the different lattice planes. Finally, at very high pH when only ammonium hydroxide is used, the growth rate is significantly reduced, but the resulting nanowires exhibit very high aspect ratios, again, and are very thin and uniform.
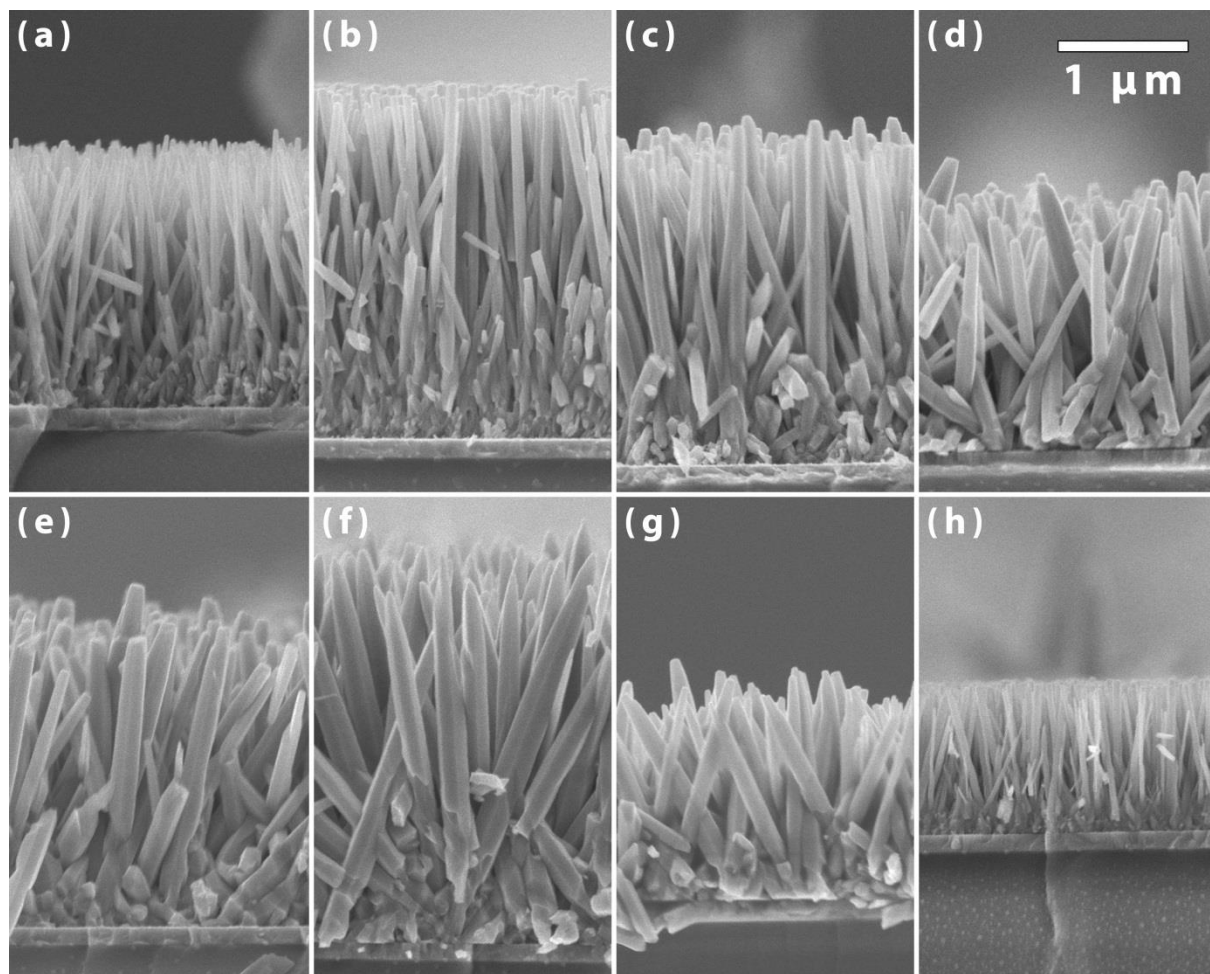
Figure 3.1   pH-dependent nanowire morphologies: (a) pH 7.3, (b) pH 7.4, (c) pH 7.6, (d) pH 7.8, (e) pH 7.9, (f) pH 8.0, (g) pH 8.2, and (h) pH 8.9. All samples were grown at 88 °C for 1 h.

Table 3.1 Experimental details of the pH-dependent nanowire growth.

pH	Length / μm	$c(NH_4NO_3)$ / mM	$c(NH4OH)$ / mM
7.3	2.1	179	71
7.4	2.6	156	94
7.6	2.7	139	111
7.8	2.0	125	125
7.9	2.3	111	139
8.0	3.1	94	156
8.2	1.7	71	179
8.9	1.2	0.0	250

3.2.2 Ultra-thin nanowires for photovoltaic applications

Typical polymer:fullerene bulk heterojunction solar cells require a phase separation between the donor and acceptor phase on a 5-10 nm length scale.[28] If the spinodal decomposition produces larger domains, excitons are likely to recombine before having diffused to the interface and dissociated. When replacing the organic acceptor phase with the zinc oxide nanowires, similar considerations apply. The exciton diffusion length in commonly used polymers such as P3HT is around 10 nm. If the distance between the interface and the location where the exciton is initially created through absorption of a photon is larger than the exciton diffusion length, the yield of charge transfer excitons will drop considerably. However, the inactive polymer regions will act as a light filter and limit the number of photons that are available to the polymer layer that is close enough to the interface. For potentially efficient device operation it therefore would be highly desirable to ensure good charge transfer exciton yield by reducing the spacing between individual nanowires to a maximum of about twice the exciton diffusion length.

We found that the nanowire length could be easily controlled via the reaction time. However, the wire diameter was already approximately 60 nm after a few minutes and almost unchanged as the reaction proceeded. It has been reported that the density of

nanowires depends on the size and number of seeds on the substrate and hence can be varied via the calcination temperature when converting the zinc acetate layer into ZnO. Lower temperatures were found to yield a large number of small seeds, whereas higher temperatures supported diffusion and Ostwald ripening and thus resulted in fewer seeds of larger dimensions.[17] In order to obtain the nanowire density required for efficient exciton collection we additionally had to make adjustments to the nanowire growth. We found that when not stirring the solution the growth was not only slower, but the resulting nanowires were only 20-40 nm in diameter with the spacing between them being in this range as well (Figure 3.2). At the early stage of the reaction considerably more seeds seem to be able to grow into small nanowires. Due to limited mass transport to the sides of the nascent nanowires, slightly smaller seeds are not rapidly overgrown by neighbouring nanowires that expand faster in diameter. Although the number of seeds that can grow into nanowires is greatly enhanced we found that the geometrical selection of well-aligned seeds seems to work very well, as we can observe only marginal differences in the degree of orientation.
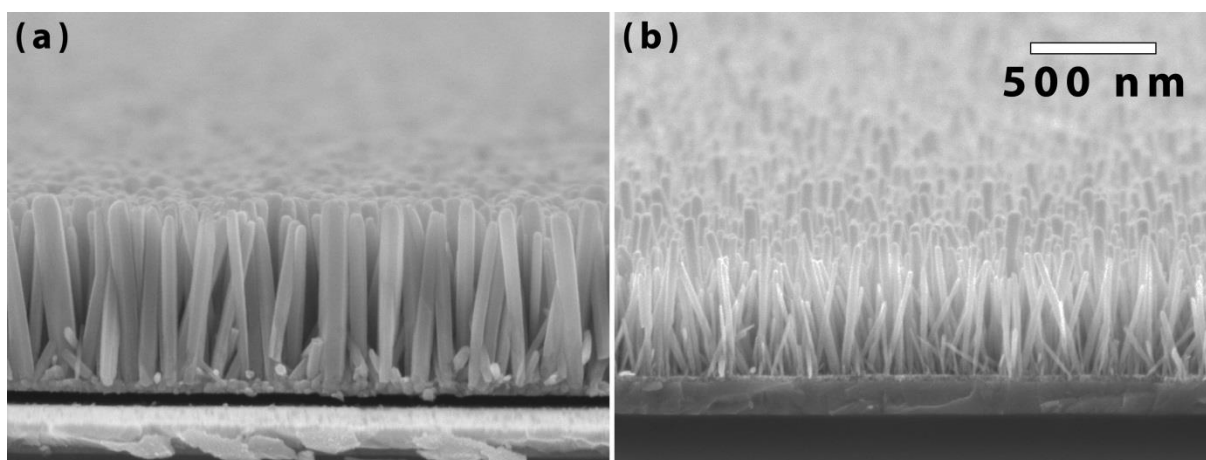
Figure 3.2   Nanowires grown at pH 8.9 for 30 min. (a) with stirring and (b) without stirring.

The orientation and crystallinity of our newly developed thin nanowires was further confirmed by X-ray diffraction (Figure 3.3). We observe a sharp and intense reflection at 34.42 °, which corresponds to the zincite (002) lattice planes, while the intensity of the (101) reflection is greatly reduced and all other reflections are absent. Nanowire arrays for photovoltaic applications were synthesized on indium tin oxide (ITO) substrate. We

found that with our method nanowires grow selectively on the seeded areas, whereas no nanowires could be observed on the exposed ITO or glass surfaces.
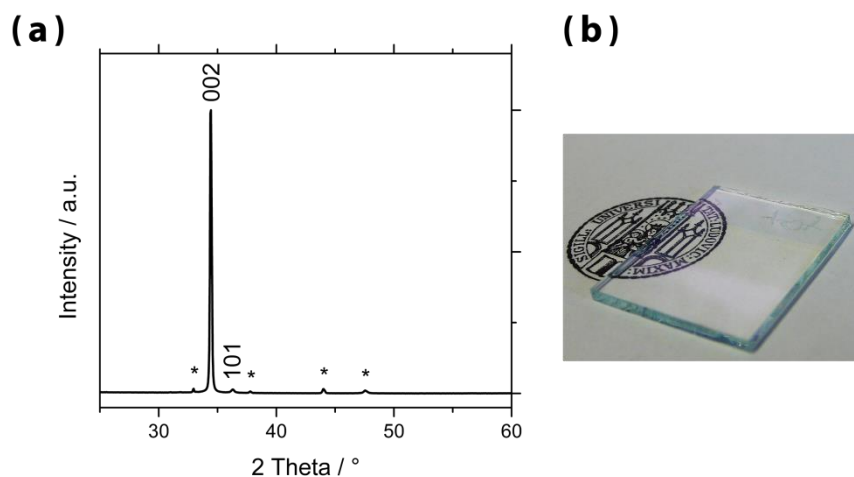
Figure 3.3 (a) X-ray diffraction pattern of a thin nanowire array. The reflections marked with an asterisk originate from the ITO substrate. (b) Photograph of a nanowire sample used for application in solar cell devices. The nanowires are selectively grown on the yellowish stripe in the middle of the sample.

3.2.3 Polymer/zinc oxide photovoltaic devices

Due to their unique morphology, which is most favourable for polymer infiltration, long-term stability, and good transport properties zinc oxide nanowires are an appealing model system as photoanodes in polymer/metal oxide hybrid solar cells.[3, 29] The highest power conversion efficiency reported until now for a zinc oxide nanowire/polymer cell using poly(3-hexylthiophene-2,5-diyl) (P3HT) is 0.74%.[30-31] The authors achieved the best efficiencies with relatively thick and long (600 nm) nanowires. However, P3HT is a strong absorber, such that the achievable photocurrent increases only marginally when raising the thickness of the active layer above a few hundred nanometers.[32] The losses due to a weaker built-in field and non-geminate recombination on the other hand increase approximately linearly with the layer thickness. Organic bulk heterojunction solar cells therefore reach their maximum

efficiency at an active layer thickness of only 230 nm for P3HT and 100 nm for most high-performing polymers.[33-34]

We reasoned that when using arrays of very thin nanowires we could achieve the same interfacial area with much shorter nanowires and thus might be able to reduce the series resistance and recombination losses associated with thicker active layers. Having developed a reproducible method for growing 20-40 nm thick nanowires with controllable length we used these arrays on ITO-coated glass substrates as photoanodes in P3HT/ZnO solar cells. P3HT was introduced via spin-coating a chlorobenzene solution onto the nanowire arrays and subsequently annealing the samples at 150 °C in argon to assist polymer infiltration into the nanowire array. A cross-sectional SEM image of a nanowire array after infiltration is shown in Figure 3.4a. Judging from the blurred shapes of the nanowires, the infiltration was successful and no larger voids are visible. Spin-coating of the polymer solution additionally generates a P3HT overlayer, which is important for avoiding short circuits through bringing the top electrode in contact with the nanowires. The devices are finished by thermal evaporation of a 10 nm WO_x layer as hole selective contact and exciton blocking layer, and a 100 nm silver electrode.

When measuring the current-voltage characteristics of the devices we notice a strong dependence of all parameters on the nanowire length (Figure 3.4b-d). Flat-layer devices, i.e. with only the seed layer, but no growth step, exhibit good rectification and low dark current. V_{OC} and FF stay relatively constant at around 300 mV up to a nanowire length of 160 nm, then decrease, due to the greatly enhanced dark current. Although the light available after having passed a certain distance within the active layer is expected to decrease logarithmically, J_{SC} increases approximately linearly with nanowire length. We attribute this to compositional gradients with considerably more ZnO at the ITO side and more P3HT close to the nanowire tips. From Figure 3.4a it is apparent that close to the seed layer a larger fraction of the total volume is taken up by zinc oxide than close to the nanowire tips. The overall power conversion efficiency reaches a maximum at a nanowire length of 160 nm, which represents the best compromise between current generation capabilities through a large interfacial area and losses due to high dark current and recombination of photogenerated charge carriers.

Several reports have indicated that the P3HT close to a metal oxide interface might not order as well as it does in a bulk film.[35-36] It is proposed that this amorphous layer and a high density of trap states at the zinc oxide surface might be the main reason for the low yield of separated charge carriers. Strategies to improve the charge carrier generation comprise passivation of the metal oxide surface with small molecules[37-38] or decorating the ZnO surface with long-chain alkanethiols for promoting P3HT crystallisation.[35, 39] These strategies might also be applicable to zinc oxide nanowires and might present opportunities for boosting device efficiencies.
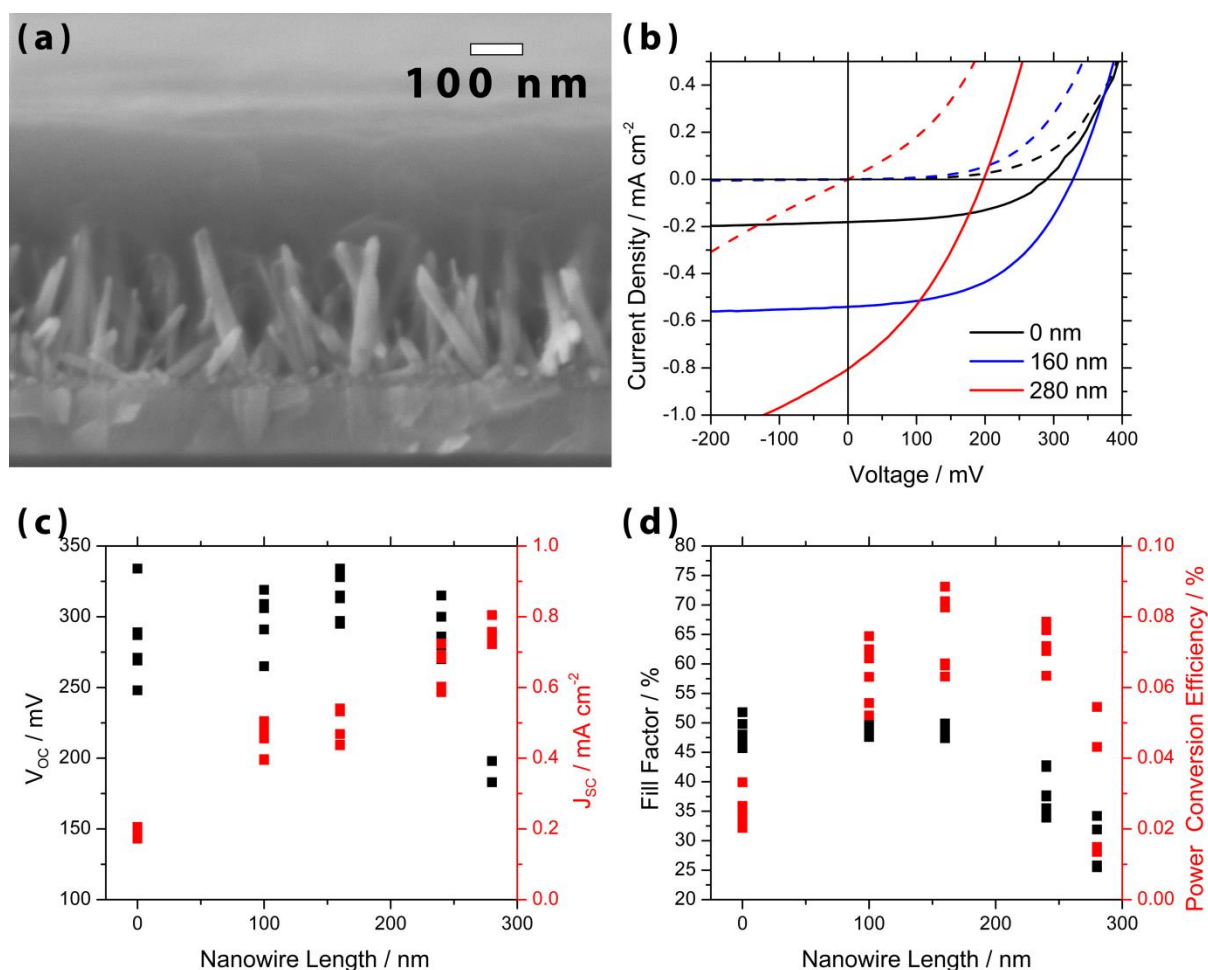
Figure 3.4   Polymer/zinc oxide photovoltaic devices. (a) cross-sectional SEM image showing the interpenetrated morphology of the active layer, (b) *J-V* curves measured under 1 sun illumination (solid lines) and dark (dashed lines) for different nanowire lengths, (c) and (d) extracted *J-V* characteristics depending on the nanowire length. The scatter plots are data from six individual devices per nanowire length.

3.3 Conclusion

Vertically oriented arrays of ultra-thin zinc oxide nanowires were successfully synthesized via an improved hydrothermal method. Through adjusting the pH of the growth solution we gained synthetic control over the resulting nanowire morphology without compromising the ability to effectively suppress bulk precipitation. Nanowire arrays that are free of any adherent precipitate and hence suitable for application in polymer/metal oxide solar cells were obtained on transparent conducting oxide-coated substrates. We incorporated these arrays into hybrid photovoltaic devices and found a clear connection between the nanowire length and the device performance, which peaks at a nanowire length of 160 nm. Improvements in device performance can be anticipated from introducing molecular modifiers to the polymer/zinc oxide interface.

3.4 Experimental Section

All chemicals and solvents were obtained from Sigma-Aldrich or Alfa Aesar in high purity grades and used as received. Regioregular P3HT (M_W = 54000) was purchased from Merck and used without further purification. Patterned ITO-coated glass (VisionTek, 12-15 ohms/sq) was cleaned by sonication in detergent solution, water, ethanol and isopropanol and was treated with an oxygen plasma directly before use.

The seed layer was deposited by spin-coating a solution consisting of 300 mM Zn(OAc)$_2$ and 300 mM ethanolamine in anhydrous 2-methoxyethanol at 3000 rpm, followed by calcination on a hot plate at 350 °C for 10 min. 50 μL of the ZnO precursor solution were used to cover a 15×15 mm^2 area of the substrate. Nanowires were grown on these seeded substrates at 88 °C in a solution consisting of 25 mM Zn(NO$_3$)$_2$, 12.5 mM HMT, 6 mM PEI (Aldrich, M_W = 800, end capped), 0-250 mM NH$_4$NO$_3$, and 0-250 mM NH$_4$OH (buffer composition and resulting pH are specified in Table 3.1). The total amount of NH$_4^+$ ions added to the solution was fixed at 250 mM, while the composition of the buffer was adjusted to yield the desired pH. 25 mL of the growth solution were used per three substrates of 20×15 mm size. After nanowire growth the substrates were removed from the hot solution, rinsed with deionized water, dried, and heated to 300 °C for 5 min on a hotplate in order to remove any organics from the surface.

The hot nanowire-coated substrates were cooled in a stream of dry nitrogen and immediately spin-coated with 40 µL of a 30 mg mL^{-1} solution of P3HT in anhydrous chlorobenzene. Spin-coating for 60 s at 1000 rpm resulted in good polymer infiltration and the formation of an overlayer of about 200 nm. The films were annealed at 150 °C for 10 min in an argon atmosphere to aid polymer infiltration and crystallisation. Photovoltaic devices were completed by thermal evaporation of 10 nm WO$_x$ and 100 nm Ag, yielding an active area of 15 mm^2 (Figure 3.5).
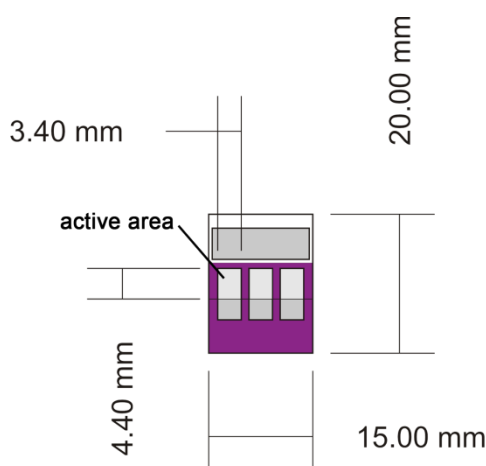
Figure 3.5   Layout with three individual devices per substrate. The active area is defined via the overlap of the ITO electrode and the top contacts, however, for accurate photovoltaic measurements an illumination mask of 3.0×4.0 mm (centred on the active areas) is used.

Scanning electron micrographs were recorded with a JEOL JSM-6500F scanning electron microscope using secondary electrons for imaging. X-ray diffraction was carried out using a Bruker D8 Discover with Ni-filtered CuK$_\alpha$-radiation (0.154 nm) and a position-sensitive detector (LynxEye). Current-voltage characteristics were measured under simulated AM1.5G solar irradiation (Solar Light Model 16S) at 100 mW cm^{-2}. The light intensity was monitored with a Fraunhofer ISE-calibrated silicon reference cell equipped with a KG5 filter for reduced spectral mismatch. *J-V* curves were recorded using a Keithley 2400 source meter. The devices were masked with a 3.0×4.0 mm mask to avoid any contribution of light that is scattered at the edges of the substrate.

3.5 References

[1]   M. Law, L. E. Greene, J. C. Johnson, R. Saykally, P. Yang, *Nat. Mater.* **2005**, *4*, 455-459.

[2]   P. Tiwana, P. Docampo, M. B. Johnston, H. J. Snaith, L. M. Herz, *ACS Nano* **2011**, *6*, 5158-5166.

[3]   Y.-J. Lee, M. T. Lloyd, D. C. Olson, R. K. Grubbs, P. Lu, R. J. Davis, J. A. Voigt, J. W. P. Hsu, *J. Phys. Chem. C* **2009**, *113*, 15778-15782.

[4]   N. O. V. Plank, H. J. Snaith, C. Ducati, J. S. Bendall, L. Schmidt-Mende, M. E. Welland, *Nanotechnology* **2008**, *19*, 465603.

[5]   P. Ravirajan, A. M. Peiró, M. K. Nazeeruddin, M. Grätzel, D. D. C. Bradley, J. R. Durrant, J. Nelson, *J. Phys. Chem. B* **2006**, *110*, 7635-7639.

[6]   N. O. V. Plank, I. Howard, A. Rao, M. W. B. Wilson, C. Ducati, R. S. Mane, J. S. Bendall, R. R. M. Louca, N. C. Greenham, H. Miura, R. H. Friend, H. J. Snaith, M. E. Welland, *J. Phys. Chem. C* **2009**, *113*, 18515-18522.

[7]   D. C. Olson, J. Piris, R. T. Collins, S. E. Shaheen, D. S. Ginley, *Thin Solid Films* **2006**, *496*, 26-29.

[8]   D. C. Olson, Y.-J. Lee, M. S. White, N. Kopidakis, S. E. Shaheen, D. S. Ginley, J. A. Voigt, J. W. P. Hsu, *J. Phys. Chem. C* **2007**, *111*, 16640-16645.

[9]   W. Kim, G. Kwak, M. Jung, S. K. Jo, J. B. Miller, A. Gellman, K. Yong, *J. Phys. Chem. C* **2012**, *116*, 16093-16097.

[10]   L.-Y. Chen, Y.-T. Yin, C.-H. Chen, J.-W. Chiou, *J. Phys. Chem. C* **2011**, *115*, 20913-20919.

[11]   J. Fan, F. Güell, C. Fábrega, A. Fairbrother, T. Andreu, A. M. López, J. R. Morante, A. Cabot, *J. Phys. Chem. C* **2012**, *116*, 19496-19502.

[12]   M. Law, L. E. Greene, A. Radenovic, T. Kuykendall, J. Liphardt, P. Yang, *J. Phys. Chem. B* **2006**, *110*, 22652-22663.

[13]   L. E. Greene, M. Law, B. D. Yuhas, P. Yang, *J. Phys. Chem. C* **2007**, *111*, 18451-18456.

[14]   L. Vayssieres, *Adv. Mater.* **2003**, *15*, 464-466.

[15]   T. Pauporté, G. Bataille, L. Joulaud, F. J. Vermersch, *J. Phys. Chem. C* **2010**, *114*, 194-202.

[16]   J. Elias, R. Tena-Zaera, C. Lévy-Clément, *J. Electroanal. Chem.* **2008**, *621*, 171-177.

[17]   L. E. Greene, M. Law, D. H. Tan, M. Montano, J. Goldberger, G. Somorajai, P. Yang, *Nano Lett.* **2005**, *5*, 1231-1236.

[18]   L. E. Greene, M. Law, J. Goldberger, F. Kim, J. C. Johnson, Y. Zhang, R. J. Saykally, P. Yang, *Angew. Chem. Int. Ed.* **2003**, *42*, 3031-3034.

[19]   D. Andeen, J. H. Kim, F. F. Lange, G. K. L. Goh, S. Tripathy, *Adv. Funct. Mater.* **2006**, *16*, 799-804.

[20]   T. Y. Olson, A. A. Chernov, B. A. Drabek, J. H. Satcher, Jr., T. Y.-J. Han, *Chem. Mater.* **2012**.

[21]   M. Kokotov, A. Biller, G. Hodes, *Chem. Mater.* **2008**, *20*, 4542-4544.

[22]   M. Kokotov, G. Hodes, *J. Mater. Chem.* **2009**, *19*, 3847-3854.

[23]   K. Govender, D. S. Boyle, P. B. Kenway, P. O'Brien, *J. Mater. Chem.* **2004**, *14*, 2575-2591.

[24]   Z. R. Tian, J. A. Voigt, J. Liu, B. McKenzie, M. J. McDermott, M. A. Rodriguez, H. Konishi, H. Xu, *Nat. Mater.* **2003**, *2*, 821-826.

[25]   V. Farías Rivera, F. Auras, P. Motto, S. Stassi, G. Canavese, E. Celasco, T. Bein, B. Onida, V. Cauda, *submitted*.

[26]   C. Xu, P. Shin, L. Cao, D. Gao, *J. Phys. Chem. C* **2010**, *114*, 125-129.

[27]   J. Qiu, X. Li, F. Zhuge, X. Gan, X. Gao, W. He, S.-J. Park, H.-K. Kim, Y.-H. Hwang, *Nanotechnology* **2010**, *21*, 195602.

[28]   Y. Vaynzof, D. Kabra, L. Zhao, L. L. Chua, U. Steiner, R. H. Friend, *ACS Nano* **2011**, *5*, 329-336.

[29]   D. C. Olson, Y.-J. Lee, M. S. White, N. Kopidakis, S. E. Shaheen, D. S. Ginley, J. A. Voigt, J. W. P. Hsu, *J. Phys. Chem. C* **2008**, *112*, 9544-9547.

[30]   L. Baeten, B. Conings, H.-G. Boyen, J. D'Haen, A. Hardy, M. D'Olieslaeger, J. V. Manca, M. K. Van Bael, *Adv. Mater.* **2011**, *23*, 2802-2805.

[31]   B. Conings, L. Baeten, H.-G. Boyen, D. Spoltore, J. D'Haen, L. Grieten, P. Wagner, M. K. Van Bael, J. V. Manca, *J. Phys. Chem. C* **2011**, *115*, 16695-16700.

[32]   G. Dennler, M. C. Scharber, C. J. Brabec, *Adv. Mater.* **2009**, *21*, 1323-1338.

[33]   W. Ma, C. Yang, X. Gong, K. Lee, A. J. Heeger, *Adv. Funct. Mater.* **2005**, *15*, 1617-1622.

[34]   T. Kirchartz, T. Agostinelli, M. Campoy-Quiles, W. Gong, J. Nelson, *J. Phys. Chem. Lett.* **2012**, *3*, 3470-3475.

[35]   T. C. Monson, M. T. Lloyd, D. C. Olson, Y.-J. Lee, J. W. P. Hsu, *Adv. Mater.* **2008**, *20*, 4755-4759.

[36]   W. J. E. Beek, M. M. Wienk, R. A. J. Janssen, *Adv. Funct. Mater.* **2006**, *16*, 1112-1116.

[37]   E. V. Canesi, M. Binda, A. Abate, S. Guarnera, L. Moretti, V. D'Innocenzo, R. S. S. Kumar, C. Bertarelli, A. Abrusci, H. Snaith, A. Calloni, A. Brambilla, F. Ciccacci, S. Aghion, F. Moia, R. Ferragut, C. Melis, G. Malloci, A. Mattoni, G. Lanzani, A. Petrozza, *Energy Environ. Sci.* **2012**, *5*, 9068-9076.

[38]   J. Weickert, F. Auras, T. Bein, L. Schmidt-Mende, *J. Phys. Chem. C* **2011**, *115*, 15081-15088.

[39]   M. T. Lloyd, R. P. Prasankumar, M. B. Sinclair, A. C. Mayer, D. C. Olson, J. W. P. Hsu, *J. Mater. Chem.* **2009**, *19*, 4609-4614.

4   Zinc Oxide Nanowires for Piezoelectric Applications

The following experiments have been performed in a joint project: The synthetic procedure for growing highly ordered ZnO nanowire arrays on transparent conductive substrates and the structural characterisation of these films were carried out by Florian Auras and Vivian Farías Rivera at LMU. The assembly of these films into nanogenerator devices and the piezoelectric measurements were performed by Paolo Motto, Stefano Stassi, Giancarlo Canavese, Edvige Celasco, Barbara Onida and Valentina Cauda at the Istituto Italiano di Tecnologia and the Politecnico di Torino.

4.1   Introduction

Zinc oxide (ZnO) is a commercially important material used for example as white translucent pigment in paints, as protective coating for metals, in rubber processing and sunscreens because it is abundant and nontoxic. In the past decade, ZnO thin films and nanostructures have become promising materials for emerging electronic applications.[1-3] Zinc oxide is a wide band gap (3.37 eV) semiconductor material with a large exciton binding energy of 60 meV.[4] It possesses great potential for optoelectronic applications due to its high electron mobility,[5] high thermal conductivity, transparency throughout the visible range, ease of doping,[6-7] UV emission,[8-9] and piezoelectricity.[10]

A wide range of ZnO nanostructures have been reported, including nanowires,[11] nanopyramids,[12] nanoplatelets,[13] and nanospheres.[14] The chemical instability of zinc oxide leads to slightly reversible crystallisation in a variety of synthetic approaches including solution-based methods and growth from the vapour phase, offering synthetic

control over the resulting nano-morphology as well as a high degree of crystallinity. The combination of its optoelectronic properties and morphological versatility make the ZnO nanostructures interesting for emerging electronic applications. Especially ZnO nanowires have attracted considerable attention as electrodes in dye-sensitized solar cells (DSCs),[15] polymer-metal oxide hybrid solar cells,[16] as material for solution-processable n-channel field effect transistors,[2] and active medium for UV lasers.[17]

Due to the combination of semiconducting and piezoelectric properties, ZnO nanostructures have recently been studied as mechanical strain sensors[18] and gas sensors,[19] as well as energy nanogenerators responding to mechanical deformation.[20-22] In these devices, the piezoelectricity is employed to convert mechanical into electrical energy for the operation of low-power electronics. The semiconducting property of ZnO is also essential, leading to the formation of a Schottky barrier between the metal contact and the nanowires.[23] In detail, lateral bending and compressive deformations of ZnO nanowires induce a charge separation and it was reported that the compressed side of the ZnO nanowire in contact with the metallic electrode develops a negative potential. The generated negative potential in the nanowires drives the electrons from the top electrode to the bottom one through the external circuit. When the stress is removed, the piezoelectric potential inside the nanowires disappears and the accumulated electrons flow back via the external circuit. The presence of the Schottky barrier is fundamental to avoid a current flow through the junction, thus preventing the cancellation of the potential induced by the deformation.

In order to produce cost-effective devices, to optimize the performance, and to cover large surface areas a profound control of the synthesis process is needed. In particular, diameter, length, orientation, crystallinity, and density of the ZnO nanowires, as well as the ability to grow on various conductive substrates are parameters of key importance for the above applications that need to be studied and controlled.[24-25] In this context different methods have been employed to develop new ZnO nanomaterials with different nanostructures and morphologies, such as vapour-phase transport processes,[26-28] chemical vapour deposition,[29] spray pyrolysis,[30-31] thermal evaporation,[32] and other template-based methods.[28] In particular, low-cost solution processes and wet-chemical methods such as electrodeposition[33-34] and aqueous

chemical growth[35-36] were widely studied; they offer the possibility of growing different ZnO nanostructures at low temperature and pressure. In particular, one of the advantages of the aqueous chemical growth is that it involves low concentrations of reactants, low pressure and moderate temperatures. Additionally, this technique offers reproducible preparation of free-standing and single-crystalline ZnO nanowire arrays at large scale and low cost.

Herein we report on the development of vertically oriented ZnO nanowire arrays on transparent conducting oxide substrates that can be used as electric nanogenerators. We demonstrate that with our approach different nanowire lengths, diameters, densities, as well as homogeneous coverage of large areas can be achieved upon variation of the synthesis parameters.

We deposited different ZnO seed-layers with the aim of determining the influence of the seeding process parameters on the final ZnO nanowire morphology and orientation. For this purpose, two different coating techniques were used, i.e. spin-coating and dip-coating. Moreover, different concentrations of the zinc acetate solution and different temperatures for the seed-layer calcination were evaluated. The final ZnO nanowire length and thus aspect ratio (length/diameter) were also investigated by varying the reaction time during the growth step.

Finally, we examined the electric and piezoelectric properties of these high-aspect ratio nanowires as a function of their length through measuring the charge generated by these nanostructures upon applying a mechanical compressive stress. By combining this array of nanostructures with an appropriate electronic circuit, one can thus obtain a mechanical pressure sensor (by measuring the amount of charge generated), or an energy harvester by storing the charges in a series of capacitors. These features, combined with the simplicity and reproducibility of the synthetic approach, make the above nanostructures a promising tool for ready-to-use devices.

4.2 Results and Discussion

The synthesis of the ZnO nanowires was carried out in a two-step procedure. In the seeding step, the substrates were covered with a precursor solution of zinc acetate (Zn(OAc)$_2$) in ethanol. Calcination promotes the formation of a very thin layer consisting of small ZnO crystals on the transparent conductive substrate (TCO) surface. These small crystals serve as nuclei for the subsequent nanowire growth.[37] The second step is the epitaxial growth of these seeds into nanowires through an aqueous chemical approach whereby the orientation of the seeds directly translates into the orientation of the nanowires.

In the case of ZnO (wurtzite structure) the c-axis of the nanocrystal coincides with the wire axis, as this crystal axis is known to have the highest growth rate.[38] This is due to the fact that the corresponding crystallographic planes (001) are the most reactive surfaces as they are terminated by either only O or only Zn atoms; in contrast, the other low-index crystallographic planes are stoichiometric and therefore less reactive.[32]

Using an appropriate seed layer, vertically oriented ZnO nanowires can be synthesized by a chemical aqueous growth method, with zinc nitrate as the Zn^{2+} precursor and hexamethylenetetramine (HMT, (CH$_2$)$_6$N$_4$) as the source of OH$^-$.[39]

In particular, we have used the so called high growth rate aqueous solution (HGRS), initially proposed by Xu et al.[40] and further optimized it in this work. The HGRS contains not only zinc nitrate and HMT, but also polyethylenimine (PEI) and ammonium hydroxide. Both compounds effectively help to suppress homogeneous nucleation, thus preventing the formation of ZnO particles in the bulk solution, while allowing high-rate one-dimensional growth of ZnO nanowires on seeded substrates. Through this approach very high aspect ratio ZnO nanowires can be obtained. Based on the above discussion, it is anticipated that the morphology of the extended ZnO nanostructures strongly depends on the morphology of the zinc acetate-based seeds;[41] moreover, the formation of these seeds is expected to be sensitive to process conditions including the coating and heating steps. In the following, we will discuss the results obtained from different deposition techniques and process parameters.

4.2.1   Seeding by spin-coating

Spin-coating is one of the most commonly used methods to prepare thin films, and often this process will be influenced by the chemical and physical characteristics of the solution to be coated, such as the solution concentration, and also by the gas atmosphere. It is well known that factors like temperature and humidity play an important role in the final film properties.[42]

a) Change of the seed-layer solution concentration

In the first experiment the TCO substrates were coated five times during the seeding step by using a solution of $Zn(OAc)_2$ in ethanol (EtOH) at different concentrations (5, 10, 20 and 25 mM), each coating followed by washing in EtOH and drying with a stream of N_2. Subsequently, the films were calcined at 350 °C to form the ZnO seed-layer. Afterwards, nanowires were grown in the HGR solution for 1 h at 88 °C.

FESEM images of the cross sections of different ZnO nanowire arrays (Figure 4.1) show dense arrays of vertically oriented nanowires. As the concentration of the $Zn(OAc)_2$ seeding solution increases, the final length and density of nanowires increase as well. Additionally, one can observe a direct relationship between the nanowire average diameter and their length with the seeding solution concentration (Table 4.1). These effects can be attributed to a geometrical selection:[43] A higher density of randomly oriented seeds provides more seeds with close to vertical c-axis orientation. Thereby the selection criterion for successful growth of a seed into a nanowire gets sharper. And since the perfectness of orientation influences the growth rate, the length is the highest for the highest density of seeds (1.95 μm length for 25 mM spin coated seed layers, see Table 4.1). In addition, we observed a more homogeneous nanowire diameter distribution in samples where higher concentrations of the seeding solution were used. In contrast to this, the nanowires grown on the 5 mM seed layer are not so densely packed and show a broader diameter distribution (from 23 to 72 nm, see Table 4.1). The best compromise in terms of high aspect ratio is reached when growing the nanowires on a 10 mM seed layer. Large surface areas of the substrates (15×20 mm^2) were homogeneously covered by the nanowires in all cases.
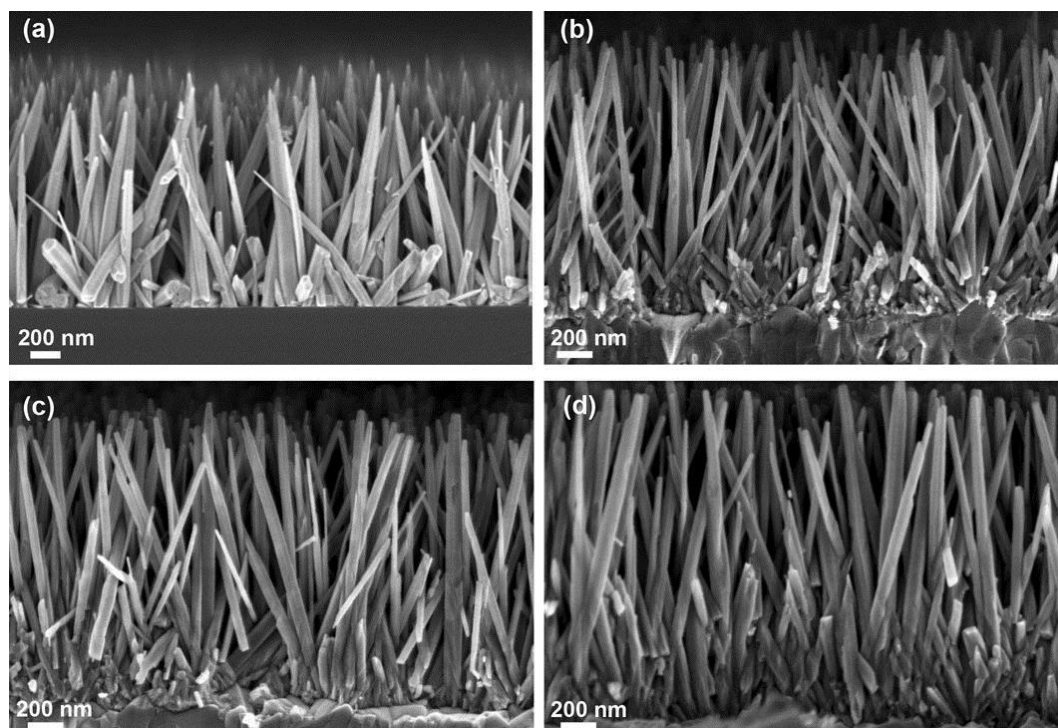
Figure 4.1   Cross section FESEM images of ZnO nanowire arrays prepared by spin-coating and calcination at 350 °C. (a) 5 mM, (b) 10 mM, (c) 20 mM, and (d) 25 mM of Zn(OAc)$_2$ in the seed-layer solution.

Table 4.1   ZnO nanowire final dimensions (D*: average diameter).

Nanowire final dimensions				
Zn(OAc)$_2$ (mM)	Length (μm)	Min. Diameter (nm)	Max. Diameter (nm)	Aspect Ratio (L/D*)
5	1.49	23	72	31
10	1.57	30	63	34
20	1.63	62	74	24
25	1.95	64	77	28

b) Change of the calcination temperature

For this experiment different TCO substrates were spin-coated once with a 10 mM Zn(OAc)$_2$ seeding solution, since in the previous experiments this concentration showed the best nanowire aspect ratio. The samples were calcined at different temperatures to evaluate the influence of the thermal treatment on the ZnO seed-layer formation, and, consequently, on the final morphology of the ZnO nanowire arrays.

From the results reported in Figure 4.2, one can observe that the calcination temperature has a great influence on the final structure and dimension of the ZnO nanowire arrays. At 250 °C (Figure 4.2a) vertically aligned, but short ZnO nanowires were obtained, with an approximate length of 900 nm and an average diameter between 43 nm and 61 nm (Table 4.2). A sample calcined at 350 °C (Figure 4.2b), shows much longer (1.57 µm) and more dense nanowires with respect to the previous sample (average diameter range from 30 nm to 63 nm). In contrast to this, the ZnO seeds calcined at 450 °C (Figure 4.2c) produce a highly dense array but a broad distribution of nanowire diameters (between 22 nm and 78 nm) and shorter length than in the previous case (1.40 µm). We therefore conclude that the optimal calcination temperature for the seed-layer is 350 °C. It has been found that both lower and higher temperatures (also at 550 °C, data not shown) yield shorter and thicker ZnO nanowires, which is not desired in this case as it decreases the final aspect ratio.
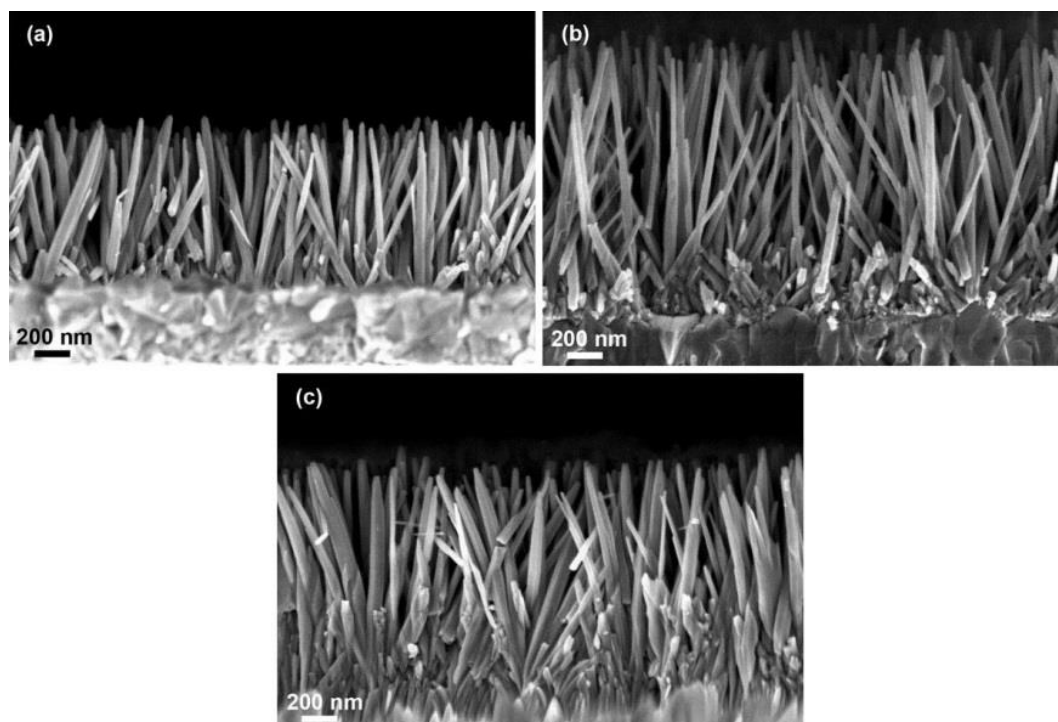
Figure 4.2 Cross section FESEM images of ZnO nanowire arrays prepared by spin-coating a 10 mM solution of Zn(OAc)$_2$ as seed-layer and grown with the HGRS technique. Seed-layers were calcined at (a) 250 °C, (b) 350 °C, and (c) 450 °C prior to nanowire growth.

Table 4.2   ZnO nanowire final dimensions (D*: average diameter).

Nanowire final dimensions				
Seed-layer calcination temperature (°C)	Length (µm)	Min. Diameter (nm)	Max. Diameter (nm)	Aspect Ratio (L/D*)
250	0.92	43	61	18
350	1.57	30	63	34
450	1.40	22	78	28

4.2.2   Seeding by dip-coating

The dip-coating method was also studied as seeding technique, because it could offer better control over the process conditions than spin-coating. Moreover, it offers the possibility of increasing or decreasing the final film thickness just by adjusting the dip-coating speed. In the following paragraphs we report on the results obtained by changing both process and synthesis parameters during the seeding step while using the dip-coater machine.

a) Change of the dip-coater speed

For this experiment, in order to assess the impact of the dip-coating speed on the final ZnO nanowire array, several TCO substrates were coated once with a seeding solution containing 5 mM $Zn(OAc)_2$ in ethanol. The dip-coater was set to different speeds equal to 44, 63, 108 and 375 mm/min, thus always maintaining the speed inside the draining regime.[42] All samples were then calcined at 350 °C and the ZnO nanowire growth was carried out with the HGRS method. The seed-layer precursor concentration was fixed at 5 mM, since no differences in aspect ratio and morphology of the final nanowires were found among 5 and 10 mM for the dip coating procedure (see Figure 4.8). However, more vertically oriented nanowires were obtained in the case of the 5 mM derived seed-layer, thus justifying the use of this concentration for all further experiments with the dip-coating deposition technique.

An obvious influence of the dip-coating speed on the final seed-layer and the resulting nanowire array can be observed in Figure 4.3. For low speeds, few randomly oriented nanowires were grown on the TCO substrate (Figure 4.3a and b), indicating that the deposited seeding material did not suffice to create a compact and homogeneous seed-layer. By increasing the dip-coating speed to 108 mm/min (Figure 4.3c and d), higher density and better orientation of ZnO nanowires than in the above two samples were obtained. The deposited seeding material was thicker than in the previous cases thus creating more dense, stable seeds and subsequently thick, dense and better oriented ZnO nanowires with 1.3 μm in length and diameters between 60 and 120 nm. There is some space between the nanowires, thus also allowing them to grow in the radial direction, resulting in larger diameters. The seeding material deposited on the substrate

at 108 mm/min was enough to create a homogeneous seed-layer, however, relatively thick ZnO nanowires with intermediate density were grown.

In contrast to this, at high dip-coating speed (375 mm/min) an even thicker seed-layer can be observed at the bottom of the nanowire array (Figure 4.3e and f), which is not visible for the samples obtained at lower speeds. This thick seed-layer allows the formation of a high quantity of seeds and, as a result, high density of ZnO nanowires with thinner diameters and better orientation. As a result vertically aligned nanowires with large surface area and high aspect ratios are obtained.
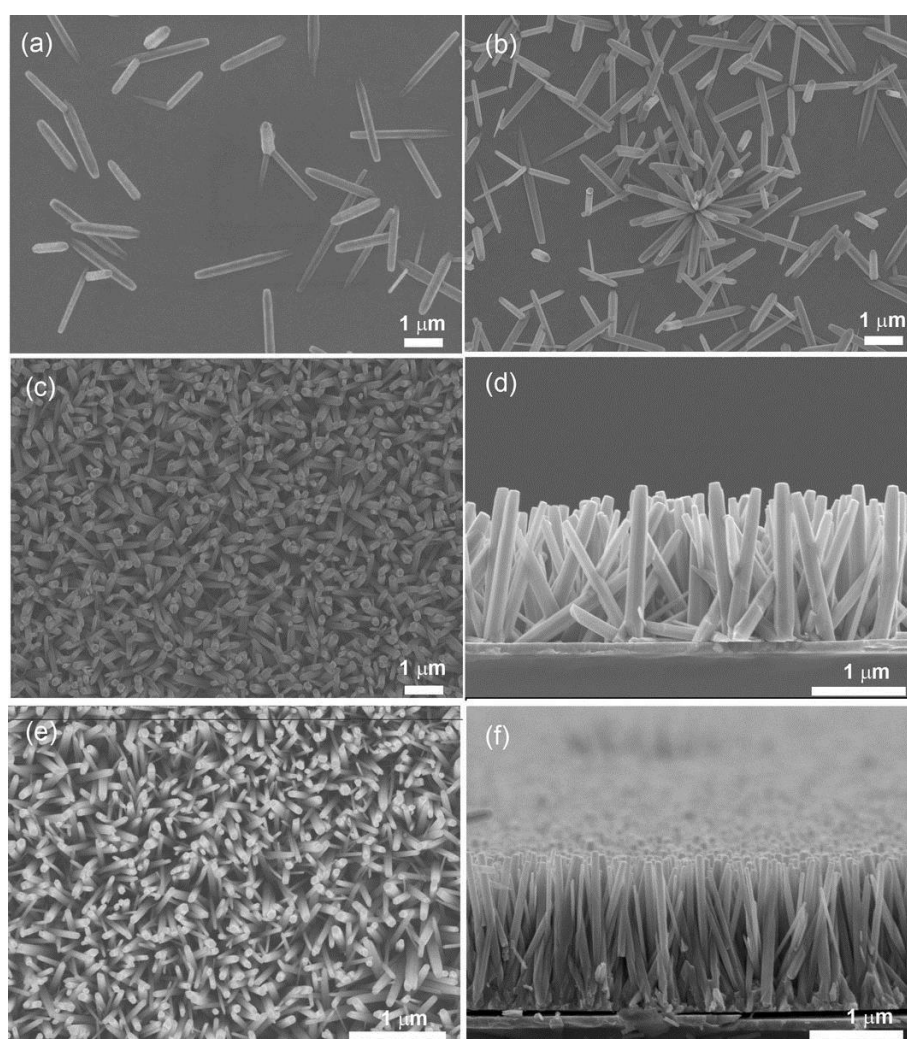
Figure 4.3 Top view and cross section FESEM images of ZnO nanowire arrays prepared by dip-coating a 5 mM solution of $Zn(OAc)_2$ as seed-layer precursor and high rate aqueous chemical growth. (a) 44 mm/min, (b) 63 mm/min, (c) and (d) 108 mm/min, (e) and (f) 375 mm/min.

b) Variation of the nanowire length with the reaction time

For this experiment TCO substrates were dip-coated at 375 mm/min in a 5 mM of Zn(OAc)$_2$ seeding solution, since these parameters were selected from the previous results for obtaining the optimal growth conditions. The main objective of this experiment was to grow very long ZnO nanowires with high aspect ratio on the seeded substrates by leaving the substrates inside the reaction solution for several hours without refreshing the growth bath. After the desired growth time the samples were removed from the reaction solution, rinsed with deionized water and dried with nitrogen. We observed a considerable reduction of the growth rate as the growth solution became increasingly depleted of the reactants. In order to grow even longer ZnO nanowires refreshing with new growth solution would be necessary.

Figure 4.4 shows the top and cross sectional FESEM images of the samples prepared at different reaction times. Besides the differences in nanowire length also a change in the shape of the nanowire tips is noticed for the different reaction times, going from flat, then flat-cone-shape and finally to concave tips (see insets).
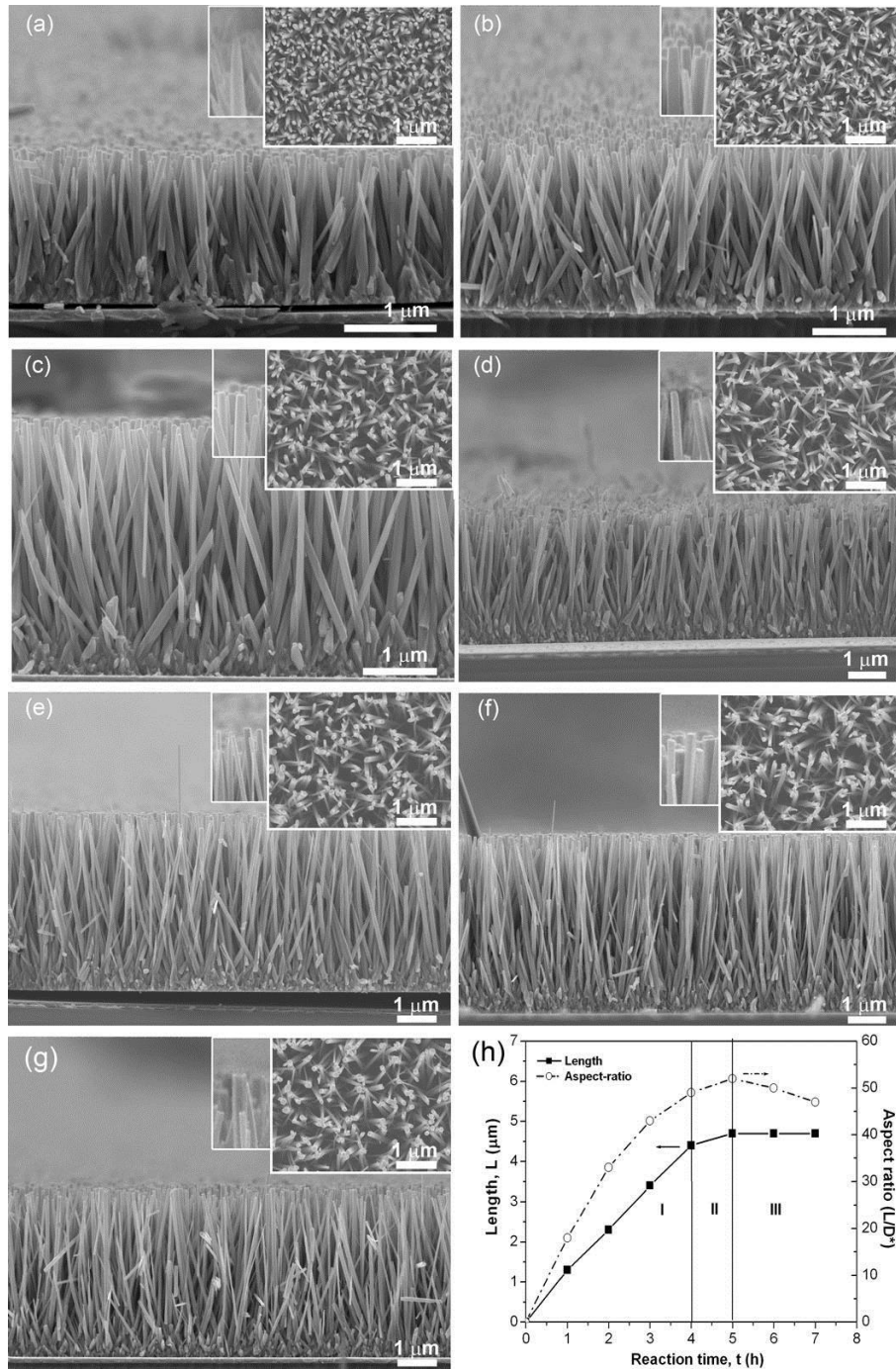
Figure 4.4 Cross section FESEM images of ZnO nanowire arrays prepared by dip-coating a 5 mM solution of $Zn(OAc)_2$ as seed-layer precursor and reaction with HGRS for (a) 1 h, (b) 2 h, (c) 3 h, (d) 4 h, (e) 5 h, (f) 6 h, (g) 7 h. (h) ZnO nanowire lengths grown from 1 to 7 hours, plotted as a function of the reaction time (D^*: average diameter). In the inset panels of the micrographs we show the top view and a magnified view of the nanowires showing their tip shape.

The nanowire length increased to 1.3 µm after 1 hour and nanowires kept growing at a rate of approximately 1 µm/h for reaction times up to 4 hours (see Table 4.3). From 4 to 5 hours the growth rate was reduced, and after 5 hours the nanowires stopped growing and the length was constant until the end of the reaction (Figure 4.4h). The nanowire diameter, however, increased from the beginning to the end of the total reaction time.

Table 4.3   ZnO nanowire final dimensions (D*: average diameter).

Time (h)	Length (µm)	Growth rate (µm/h)	Min. Diameter (nm)	Max. Diameter (nm)	Aspect Ratio (L/D*)
1	1.3	1.3	40	100	18
2	2.3	1.0	40	100	33
3	3.4	1.1	60	100	43
4	4.4	1.0	60	120	49
5	4.7	0.3	60	120	52
6	4.7	0.0	60	130	50
7	4.7	0.0	70	130	47

The aspect ratio of the nanowires increased during the first 5 hours. It was relatively high even after 1 hour and reached a maximum value of 52 after 5 hours. Afterwards, the aspect ratio began to decrease as nanowires stopped growing and the length remained constant due to reactant depletion.

As mentioned above, we notice three different regions in Figure 4.4h with different growth behaviours. In region I (from the beginning of the reaction to four hours), the nanowires begin to grow from the pre-existing ZnO seeds in the seed-layer.

At this initial stage of growth, the reaction

$$Zn^{2+} + 2OH^- \leftrightarrow ZnO + H_2O$$
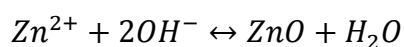
is favoured, leading to the continuous growth of ZnO on the previously formed ZnO sites. In this stage, Zn^{2+} and OH- ions from the growth solution (provided by the zinc nitrate

salt and by the decomposition of the HMT) are present at high concentration and attach mainly at the nanowire tip to promote the anisotropic nanowire growth. The growth rate is approximately constant at $1\,\mu m/h$ until 4 hours and the nanowire length increases linearly in region I, then the growth rate decreases in region II and finally reaches zero in region III (from 5 to7 hours). In the region III the nanowires stop growing due to depletion of the zinc precursor in the growth solution. At this point, the growth solution is depleted enough that it cannot maintain the fast anisotropic growth. The still high concentration of OH$^-$ ions promotes Ostwald ripening, which leads to a dissolution of material from the polar nanowire tips and deposition onto the nonpolar side facets of the nanowires. Additionally there is still some deposition at low rate, called surface reaction process as reported in the literature[44] in the presence of capping agents, like PEI in this case. Both factors together might result in stagnating or eventually even decreasing length, while the diameter slowly increases. This is supported by the observation of slightly concave and etched nanowire tips.

For all the above samples, X-ray diffraction showed a wurtzite ZnO pattern with an enhanced (002) peak intensity attributed to the vertical orientation of the nanowires. The ZnO nanowires are single crystalline as shown by high resolution transmission electron microscopy (see Figure 4.9 and Figure 4.10).

4.2.3   *Electric and piezoelectric characterisation*

The conductivity of ZnO can strongly affect the piezoelectric response. The higher the free carrier concentration due to the presence of crystallographic defects (i.e. oxygen vacancies), the higher is the conductivity of the material, resulting in a lower piezoelectric coefficient d33. This observation is explained by the reduction of the Madelung constant due to free electrons and to a screening effect on the electric dipole displacements (related to the ions) in the ZnO crystal.[45]

In order to compare the electric behaviour of the nanowires with different lengths, we measured their current-voltage (I-V) characteristics (Figure 4.5). We first note that in all cases we obtain a Schottky behaviour of the I-V characteristics. The concentration of free carriers in the ZnO nanowires is inversely dependent on their length. We note, however,

that the variation of the current values is higher than the variation in length between the different samples, due to the fact that the presence of crystallographic defects in the nanowires does not linearly increase with their length, but it is related to the crystal growth governed by Ostwald ripening and the surface reaction mechanism, as mentioned above. Thus, a direct piezoelectric response would be partially quenched due to free carriers that screen the charges generated by the piezoelectric effect.

In direct piezoelectricity, the application of a mechanical stress on the piezoelectric material results in the generation of an electric field between its ends. The most common methods for characterizing the direct piezoelectricity of such nanostructures usually involve tensile loading or lateral bending of the material with simultaneous measurement of generated charge or electric potential.[21-22] This is challenging because the charges or voltages tend to be small and are partially screened by the free carriers due to the semiconducting nature of ZnO, thus requiring highly sensitive electronics.[23] In general, the generated charge can be utilised in sensing and energy harvesting.
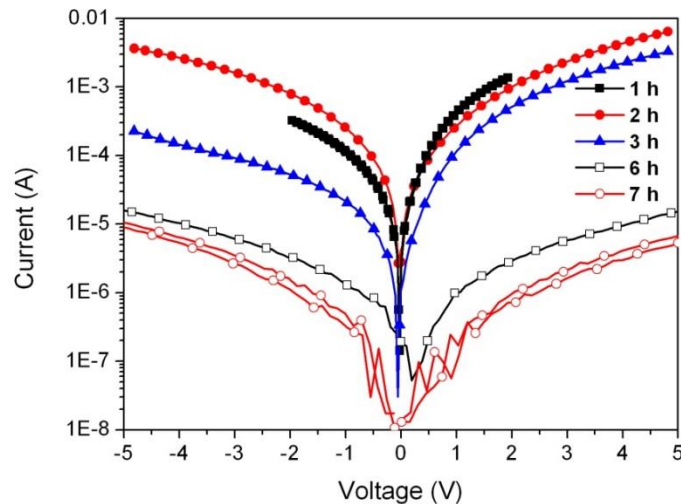
Figure 4.5 I-V characteristics of ZnO nanowires with different lengths resulting from their growth time, showing the Schottky contact between the semiconducting ZnO and the electrode used. The current values are plotted in logarithmic scale; therefore the absolute values are plotted.

In the present case, to evaluate the piezoelectric properties of the nanowires (i.e. the electric charge generated upon a mechanical deformation), we use a charge amplifier. It

converts the charge output of the ZnO nanowires into a proportional voltage, which is used as an input variable for the analysis system. A charge amplifier basically consists of an inverting voltage amplifier with a high open-loop gain and capacitive negative feedback. It possesses a junction field-effect transistor (JFET) at its input to achieve high insulation resistance and minimise the leakage current. If the open-loop gain is sufficiently high, the cable and sensor capacitance can be neglected, thus leaving the output voltage, V, dependent just on the charge, Q, at the charge amplifier input and on the range capacitor C_r:

$$V = \frac{-Q}{C_r}$$

The amplifier acts as an integrator that constantly compensates the nanowire electric charge with one of equal magnitude and opposite polarity of the range capacitor. The voltage across this capacitor is proportional to the charge generated by the nanowires. Thus, the charge amplifier converts an electric input charge Q into a usable proportional output voltage V. Figure 4.11 shows the charge amplifier electric circuit, where the electric analogue of the ZnO nanowires is a capacitor in series with a voltage source between IN1 and IN2 (not shown in the circuit). The nanowires have high output impedance and require a high-impedance buffer amplifier. The circuit includes a differential charge amplifier followed by a differential-to-single-ended amplifier. The differential topology reduces line-noise pickup, which is a problem in high-gain circuits. More details are provided in the supporting information (Chapter 4.5).
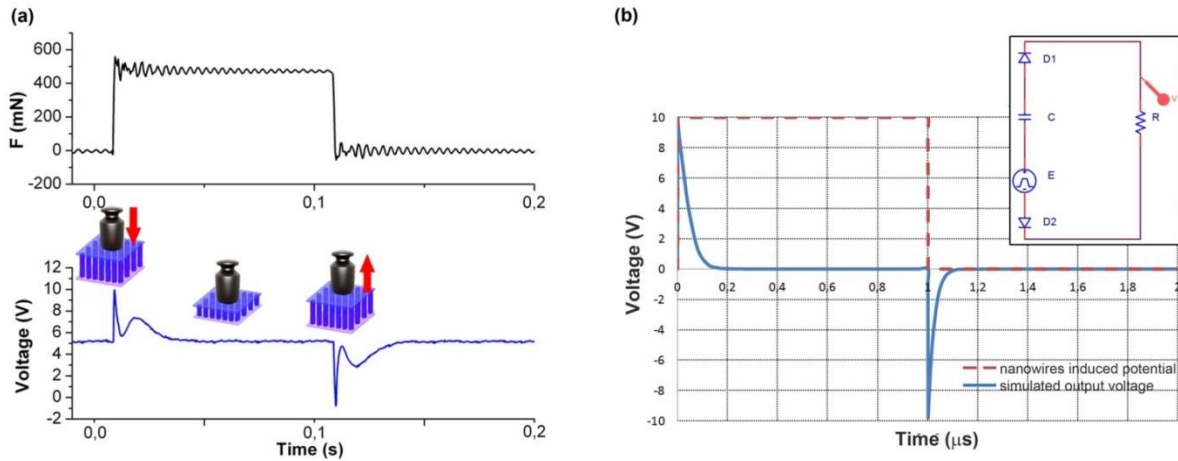
Figure 4.6 (a) The compressive force applied by the piezoelectric disk to the nanowire array (top) is synchronous to the first generated double electric pulse (voltage). The nanowires remain compressed until the compressive force is removed, i.e. after 0.1 s, and the release of the force generates another electric pulse with opposite polarity. The first intense and sharp signal of the voltage double peak is generated by the transient deformation applied to the nanowires, whereas the second pulse, broad and small, is attributed to a damped mechanical resonance of the actuation structure that induces a second force oscillation on the nanogenerator. (b) Simulated induced potential in the ZnO nanowires (red dashed line) and simulated output voltage (blue straight line) obtained from the nanowire array. Inset: the equivalent electronic circuit used for the PSpice simulation.

In order to induce the generation of an electric charge, the nanowires were subjected to a mechanical strain by means of a piezoelectric ceramic disk actuated by the piezo evaluation system with an electric square waveform with voltage amplitude of 800 V. This piezoelectric actuator generates pulses of force for 0.1 s equal to about 500 mN with intervals of 1 s from the previous to the next pulse on the ZnO nanowire top electrode (Figure 4.6a, top graph). The ZnO nanowire array is compressed by this force, which leads to the generation of an impulse of charges. These charges are converted into an output voltage dependent on the value of the capacitor C_r from the charge amplifier circuit, as previously explained. A National Instruments board connected to a LabView program was used for measuring the output voltage. The first positive peak is the output generated upon exerting the compressive strain, and the second negative pulse, after 0.1 s, is related to the release of the mechanical stress (see bottom graph and related

sketch in Figure 4.6a). Both, the positive and the negative measured pulses are composed of two distinct peaks: the first sharp and intense one is the voltage generated from the nanogenerator, whereas the second pulse, broader and smaller than the previous one, is attributed to a damped mechanical resonance of the actuator. This second oscillation is not considered in the calculation of the generated charge and energy.

The synchronisation between the induced mechanical displacement (due to both application and release of the compressive load, top graph of Figure 4.6a) and the generated voltage pulses of the ZnO nanowires (bottom graph) experimentally demonstrate their cause-and-effect relation. Furthermore, to clarify this behaviour, a model was developed for the PSpice circuit simulator. The nanowires can be modelled as a capacitor and a voltage generator (indicated in the inset of Figure 4.6b with E and C, respectively), which pushes the electron flow in the external circuit when nanowires are subjected to vertical strain.[46-47] If a Schottky contact is present at least in one end-electrode, it prevents the flow of electrons in the external circuit through the nanowire, such that the piezoelectric potential, induced by the external deformation is preserved.[48] In this case a piezoelectric potential is generated along the vertical axis of the nanowire: One side of the nanowire is subjected to a negative piezoelectric potential and the other side to a positive one. The generated negative potential in the nanowires drives the induced electrons from the top electrode to the bottom one through the external circuit. As the external force is removed, the piezoelectric potential inside the nanowires disappears and the accumulated electrons flow back via the external circuit. Consequently, an AC voltage and current pulses are recorded when an external elastic deformation is both applied and removed. Effective Schottky contacts at the top and bottom electrodes (*D1* and *D2* in the inset of Figure 4.6b) are preferred for AC power generation.[49] An electrical load R is connected to the nanowire model. The generator E was modelled to produce a signal proportional to the mechanical deformation generated by the piezo actuator (red dashed line in Figure 4.6b), whereas the blue curve represents the simulated generated voltage related to the probe V placed near the resistance R. The theoretical analysis is very similar to the experimental data reported in Figure 4.6a (bottom graph) with the exception of the second experimental parasitic damped peak induced by a structural mechanical resonance of the employed set up.

With the experimental setup described above, we have analysed the charge (measured as voltage) generated by the ZnO nanowires grown for 1, 3 and 7 hours. The overall results are shown in Figure 4.7, displaying the generated voltage versus the actuation time of the piezoelectric disk and the generated energy as a function of the nanowire length (Figure 4.7c). To enhance the measured values and to distinguish them from noise, different values of capacitance, C_r, were used in the charge amplifier circuit (from 100 pF for 1.3 µm long ZnO nanowires grown for 1 h, to 220 pF for those 3.4 µm long, and to 390 pF for those 5.7 µm long, grown 7 h). This solution allows having uniform measurements for different nanowire lengths. For this reason, both Figure 4.7a and b display the same maximum output voltage (note that the baseline is set to 5 V as explained in Chapter 4.5). The single pulses are enlarged in both insets.

By reversely connecting the polarity of the ZnO nanowires to the charge amplifier system (switching polarity), the generated output shows an inverse trend (first pulse negative and second one positive, see Figure 4.12). With these measurements we can confirm that the signal is truly generated from the nanowire device and we can rule out any artefact or noise.[50]

Figure 4.7c shows the energy produced by the nanowires as function of their length. By maintaining a constant C_r, a factor of proportionality is introduced to calculate the produced energy by the different nanowires:

$$W = \int_0^Q V dq = \int_0^Q \frac{q}{C_r} dq = \frac{1}{2} \frac{Q^2}{C_r} = \frac{1}{2} C_r V^2$$

From this equation the energy is related to the generated charge and to the output voltage. It increases with the length of the nanowires.[51]

Combining these results with the previous I-V characteristics, the strongest piezoelectric response was obtained for the nanowires grown for 7 h, i.e. the longest nanowires used in this work (4.7 µm). They were found to generate a higher amount of electric charge than the shorter nanowires under the same mechanical compressive stress. In contrast, the shortest nanowires, grown for 1 h, showed the highest conductivity.

With the present charge amplifier circuit one can use the ZnO nanowire arrays as a mechanical pressure sensor, or even store the generated charge in a series of capacitors, thus using the nanowires as energy harvester.[20] The key to use the nanowire arrays is that any tiny physical motion, even the one applied here by our actuator, can be converted in electrical energy.
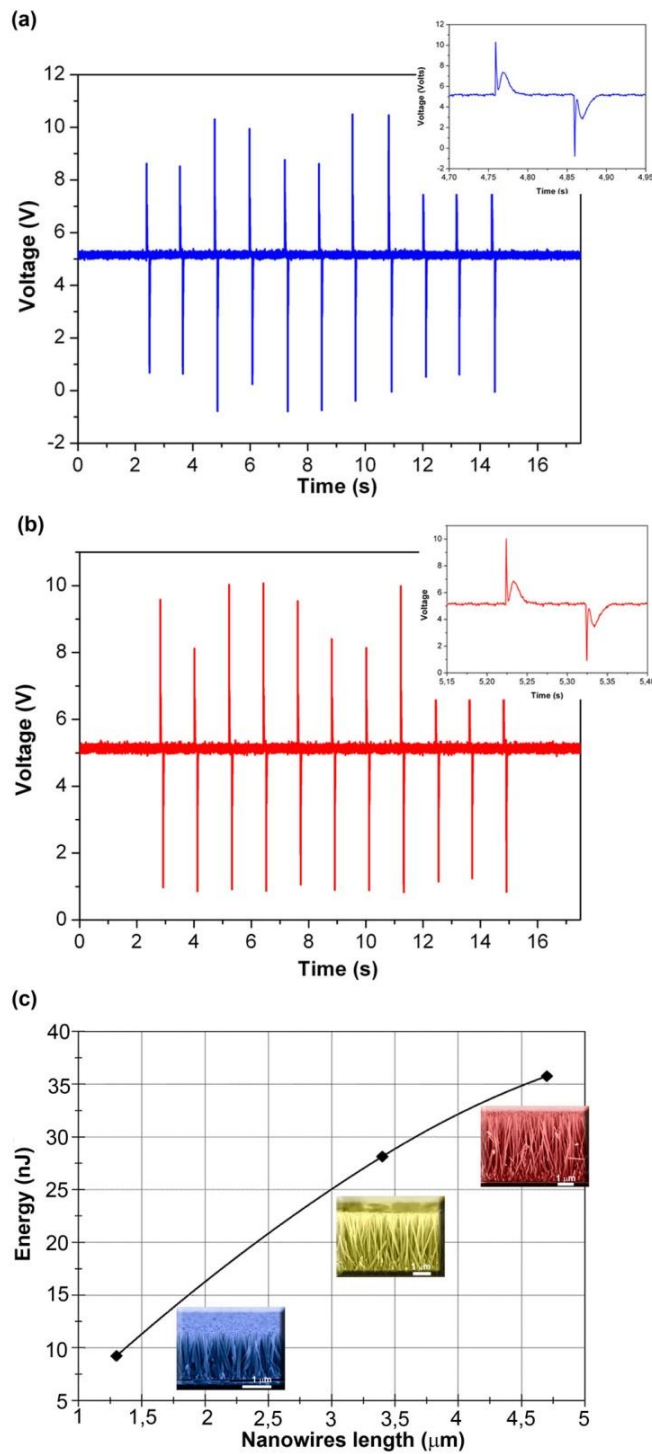
Figure 4.7 (a) Electric output generated upon compression of the nanowires grown for 1 h (length 1.3 μm) and (b) for 7 hours (length 4.7 μm). Insets in the right panels of (a) and (b) are enlarged views of a single pulse, where the first two voltage pulses correspond to applying and the second ones to releasing the compressive force. (c) Energy produced by the nanowires as a function of their length.

4.3 Conclusion

Vertically aligned ZnO nanowire arrays with high aspect ratios were successfully obtained on seeded substrates by hydrothermal synthesis. The synthesis procedure was optimised and dense arrays of 1D vertically oriented ZnO nanowires with aspect ratio of up to 52 were obtained with homogeneous coverage of large substrates. The ZnO nanowire morphology and alignment can be controlled by adjusting parameters such as the seed-layer deposition process and solution concentration, the heating processes and the growth reaction time. The versatility of this process allows convenient tuning of the final dimensions and morphology of the ZnO nanowire arrays by changing the experimental conditions depending on the desired properties, e.g. a more pronounced conductive or piezoelectric behaviour.

Both electric and piezoelectric properties of the nanowires were studied as a function of their length, and the generated charge and output voltage were measured by a charge amplifier. We found that the longer the nanowires, the lower is their conductivity and the higher the charge generated upon exerting a mechanical compressive deformation. The reproducible growth of such vertically oriented ZnO nanowires on conductive substrates allows their use as mechanical strain sensors as well as energy harvesters.

4.4 Experimental Section

4.4.1 Synthesis of the ZnO nanowire arrays

Indium tin oxide (ITO, VisionTek, 12 Ohms/sq.) and F-doped tin oxide (FTO, Pilkington TEC 7) glass slides were used as transparent conductive (TCO) substrates and cut into pieces of 15×20 mm^2. The as-cut glass pieces were thoroughly cleaned with detergent solution (Extran, Merck) at 60 °C for 30 min, sonicated for 15 min, rinsed with deionised water and successively sonicated in ultra-pure water and absolute ethanol. Afterwards, the glass slides were dried in a stream of N_2 gas. Directly before use the substrates were cleaned in an oxygen plasma.

The seed-layer preparation was carried out using two techniques. For the first set of samples, spin coating was carried out using a two-step program (1000 rpm for 20 s and

then 3000 rpm for 30 s), followed by immersion in ethanol for 10 s and drying with a stream of nitrogen. This procedure was repeated five times to ensure homogeneous and complete coverage. Seeding solutions of zinc acetate (99.99%, Sigma-Aldrich) in HPLC grade ethanol with concentrations from 5 mM to 25 mM) were used. The second set of samples was seeded by dip-coating at a speed ranging from 44 to 375 mm/min while using a constant concentration of zinc acetate (5 mM) in ethanol. The temperature and the relative humidity were kept constant at 20 °C and 33% r.h., respectively. After depositing the $Zn(OAc)_2$ layer, the substrates were calcined in air at 350 °C (unless stated otherwise) for 20 min (heating rate 5 °C/min) in order to convert the deposited film into a polycrystalline layer of ZnO.

Nanowire growth was carried out by immersing the seeded substrates into an aqueous solution containing zinc nitrate hexahydrate (98%, Aldrich), hexamethylenetetramine (HMT, 99.5%, Sigma) as hydroxide source with a Zn^{2+}:HMT molar ratio of 2:1, 5 mM polyethylenimine (PEI, M.W. = 800, end capped, Aldrich) and 320 mM ammonium hydroxide.

Hydrothermal growth was carried out at 88 °C under stirring at 400 rpm for reaction times ranging from 1 h to 7 h. The samples were removed from the hot solution, washed with deionised water and dried with a stream of nitrogen.

4.4.2   Characterisation

The different morphologies and orientations of the ZnO nanostructures were studied with a field emission scanning electron microscope (FESEM, Zeiss Auriga Dual-Beam or JEOL JSM-6500F). X-ray diffraction patterns were recorded in reflection geometry using a Bruker D8 Discover with Ni-filtered CuK_α-radiation and a LynxEye silicon strip detector. High Resolution Transmission Electron Microscopy (HRTEM) images were carried out using a FEI Tecnai G2 F20 S-TWIN, operating at 200 kV. The current versus voltage (I-V) characteristics were evaluated by a Piezo Evaluation System (PES, TFAnalyzer 2000HS, Aixacct) coupled to a single-point laser vibrometer from Polytec OVF-505), by contacting the conductive TCO substrate with a micro-manipulator and the

top of the nanowires with an aluminium cylinder of 7 mm² cross section, both connected to the instrument.

To induce the generation of electric charge, the nanowires were subjected to a controlled mechanical strain by means of a piezoelectric PZT (lead zirconate titanate) disk (PIC 151, PhysikInstrumente) used as actuator and pressing on the aluminium top electrode. This system generates pulses of force equal to about 500 mN with intervals of 1 s by applying an electric square waveform with voltage amplitude of 800 V with the PES. The charge generated by the ZnO nanowires was converted into a voltage output by means of a homemade charge amplifier, described in detail in the supporting information (Chapter 4.5), and measured with a National Instruments USB-6259 electronic board and a LabView program. By considering the capacitor used in the circuits, the generated charge, Q, and energy, W, were calculated.

4.5   Supporting Information

4.5.1   *Dip-coating procedure: Changing the seed layer solution concentration*

In order to assess the best concentration of seed-layer precursor for the dip-coating procedure, different seeding solutions were used during the coating step while keeping the dip-coating speed constant at 375 mm/min. For that purpose 2, 5, 10 and 20 mM Zn(OAc)$_2$ solutions were prepared in ethanol and used to coat the TCO substrates once, without ethanol rinsing. The samples were then calcined at 350 °C and the nanowire growth was performed under HGRS conditions. Table 4.4 summarises the final dimensions of the four different samples.

Table 4.4   ZnO nanowire final dimensions (D*: average diameter).

Nanowire final dimensions				
Zn(OAc)$_2$ (mM)	Length (µm)	Min. Diameter (nm)	Max. Diameter (nm)	Aspect Ratio (L/D*)
2	1.8	30	100	27
5	1.5	40	120	19

| 10 | 1.5 | 30 | 120 | 20 |
| 20 | 1.3 | 20 | 60 | 16 |

It is apparent that the concentration of the $Zn(OAc)_2$ seeding solution has a direct influence on the final ZnO nanowire structure (Figure 4.8). As the concentration of the seeding solution increases, both the final length and the average nanowire diameter decrease. At the same time, the diameter range becomes narrower, which indicates that the nanowires become more homogeneous.

It is worth noting that no strong differences are observed among the 5 and 10 mM seeding solution regarding the final nanowire dimensions. However, more vertically oriented nanowires were obtained in the case of the 5 mM seed-layer, thus justifying the use of this concentration for further experiments with the dip-coating deposition technique.
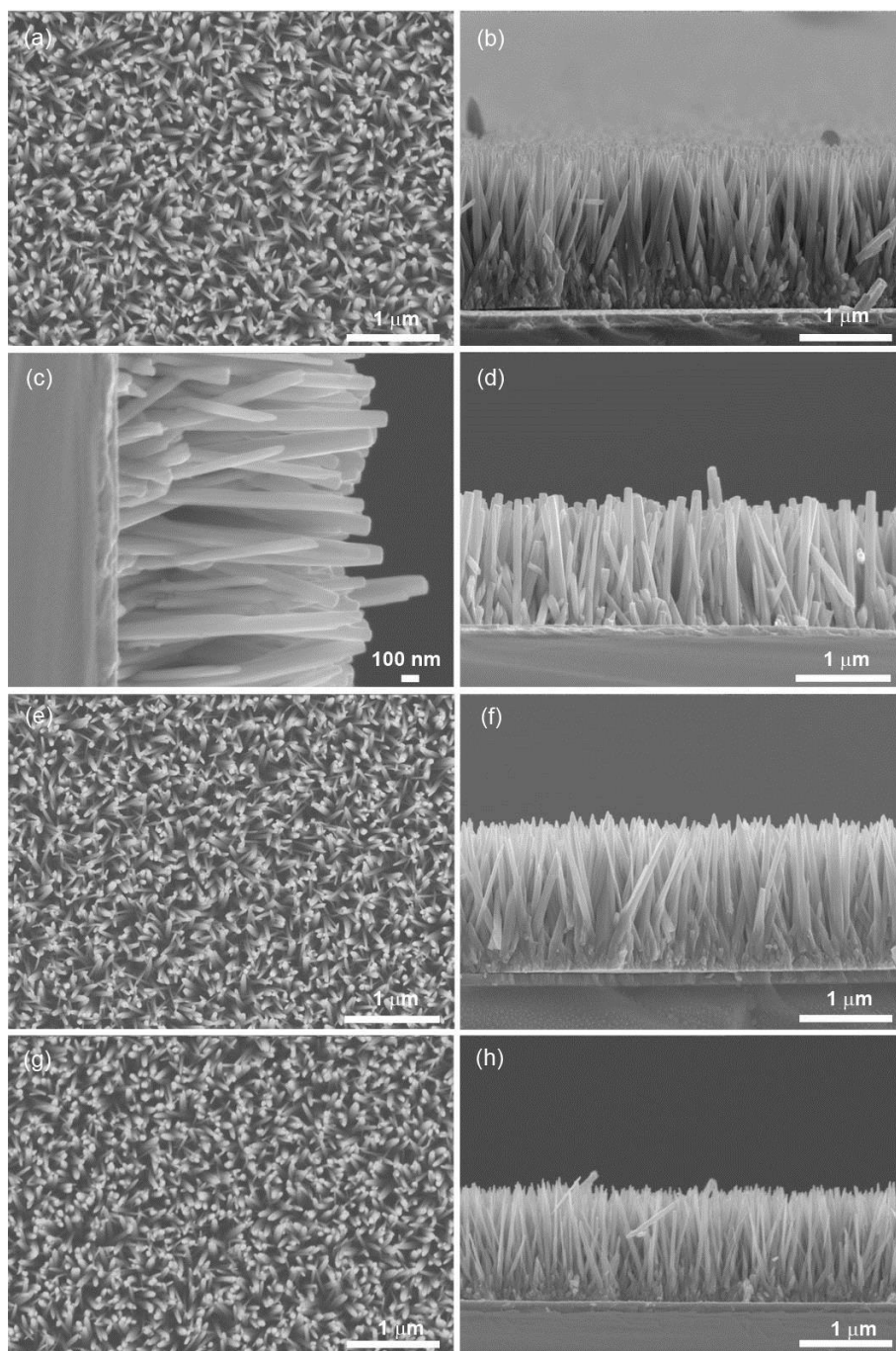
Figure 4.8 Cross section FESEM images of ZnO nanowires prepared by dip-coating (375 mm/min) different Zn(OAc)$_2$ solutions as seed layer precursor and HGRS. (a) 2 mM, (b) 5 mM, (c) 10 mM, and (d) 20 mM.
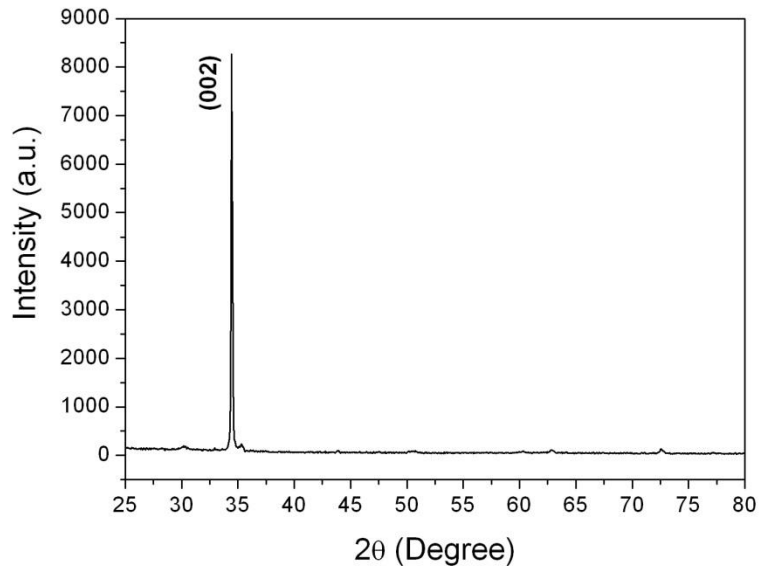
Figure 4.9   XRD of ZnO nanowire films prepared by dip-coating.

Figure 4.9 shows a typical X-ray diffraction pattern measured on a ~1.5 μm thick nanowire film. The high intensity of the (002) diffraction peak and almost complete absence of all other reflections confirms the preferred vertical orientation of the nanowires.
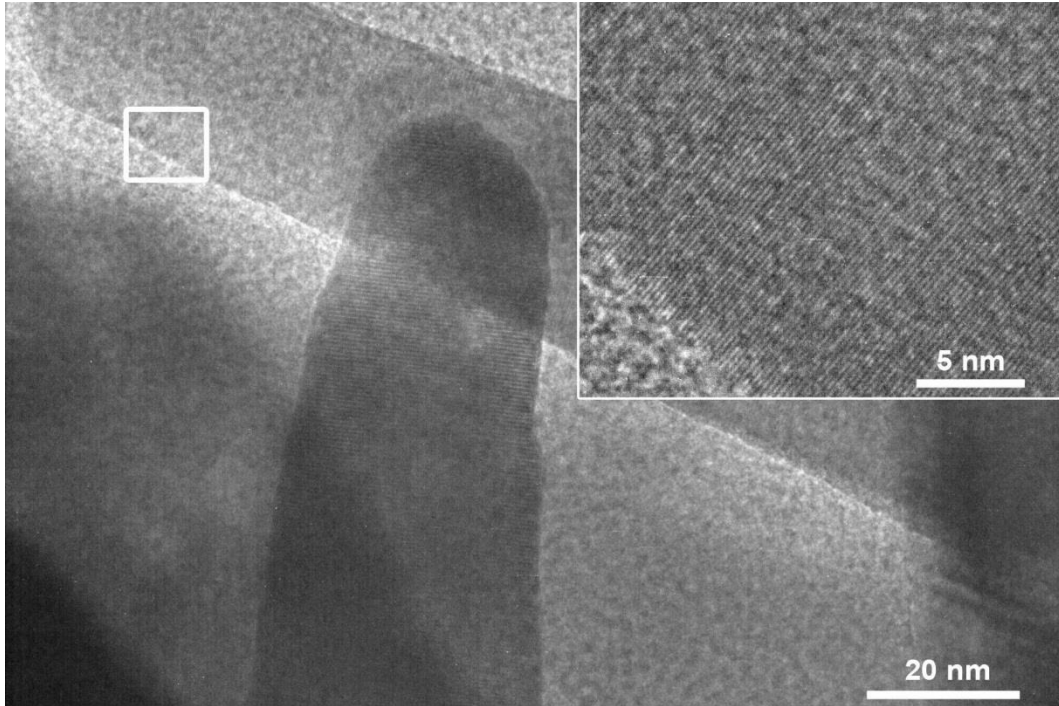
Figure 4.10 HRTEM image of two ZnO nanowires. The white rectangle is magnified in the inset, showing the lattice fringes and thus indicating the single crystalline nature of the nanowires.

4.5.2 Charge amplifier description

The electrical analogue of nanowires is a capacitor in series with a voltage source. The nanowires have high output impedance and require a high-impedance buffer amplifier. The circuit, shown in Figure 4.11, includes a differential charge amplifier followed by a differential-to-single-ended amplifier. The differential topology reduces line-noise pickup, which is a problem in high-gain circuits. A dual operational amp (IC2) endows the differential charge amplifier with single-supply operation and low supply current. R1, R2, and a small bypass capacitor (C3) set the input common-mode voltage at the mid-supply level. The differential amplifier does not amplify thermal noise generated by these resistors. Instead, it appears as a common-mode signal at the differential outputs and is attenuated by common-mode rejection in the following stage. Because thermal noise is proportional to resistance, this topology offers the advantage of lower supply current for a given noise target, whereas it does not amplify the biasing noise. AC gain for the differential stage is set by the C1 and C2 value relative to the nanogenerator capacitance (CEQ). In this case, CEQ measures 484 pF at 1 kHz, with an equivalent series

resistance (ESR) of 5 kΩ. One can model the ZnO nanogenerator as a differential voltage source in series with two capacitors of value 2CEQ. R3 and R4 have little effect at high frequencies because feedback is dominated by the reactance of C1 and C2. As a result, each half of the circuit has a gain of C1/CEQ = 96. The differential amplifier also acts as a first-order high-pass filter. To simplify analysis, one can assume C1 = C2 = C and R3 = R4 = R. Then, an inspection of either half of the amplifier shows a pole at $1/2\pi RC$ and a gain of CEQ/C at infinite frequency. AC gain is proportional to CEQ/C, so high AC gain implies a small C. In this case, C = 10 pF and R = 44 MΩ, which leads to a corner frequency of 360 Hz. R must be very large for good low-frequency response. Lowering the corner frequency means increasing the value of R, but the op amp's input leakage flowing in a large feedback resistor can produce a large offset voltage. To counter this effect, the dual operational amp is a CMOS device chosen for its small input leakage, which is only 1 pA. Differential-to-single-ended conversion is performed by IC2 and the resistors R5, R6, R8, and R9. The values shown give a differential gain of 20. Line-noise rejection depends on the match between C1 and C2, but tight-tolerance capacitors are expensive (in general, this is a disadvantage of differential charge amplifiers). If a perfect match cannot be obtained, the circuit's first-order rejection is still better than that of a single-ended amplifier.
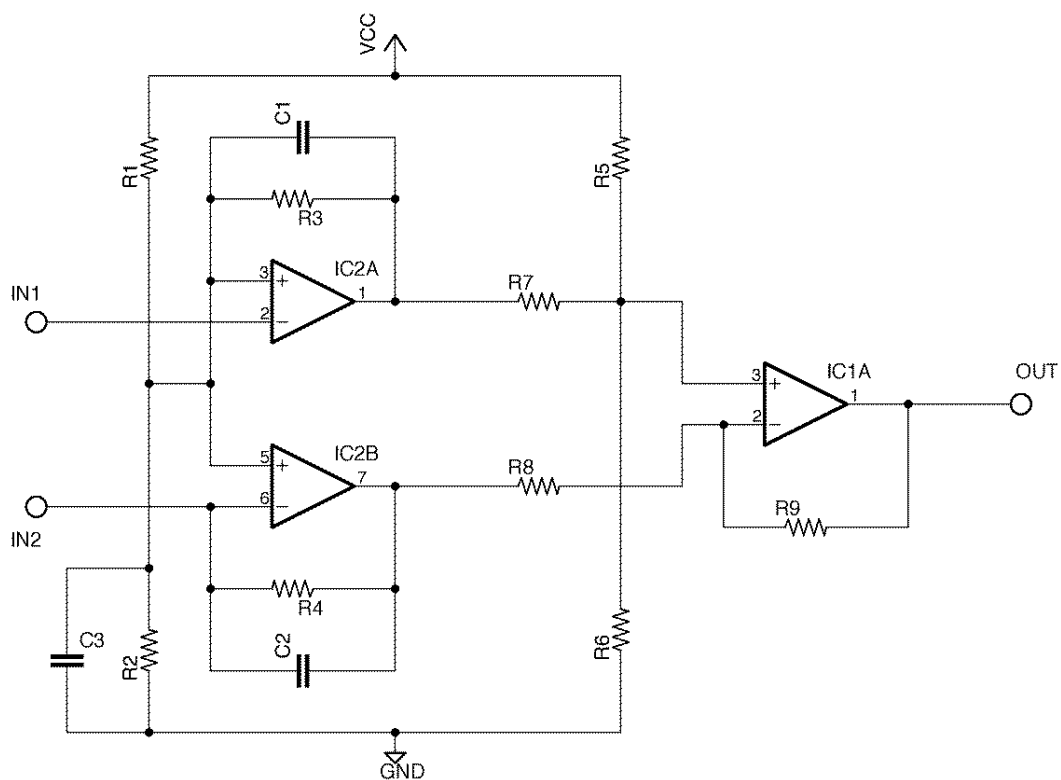
Figure 4.11   Electric circuit scheme of the charge amplifier, where the ZnO nanowires should be inserted between the IN1 and IN2 clamps.
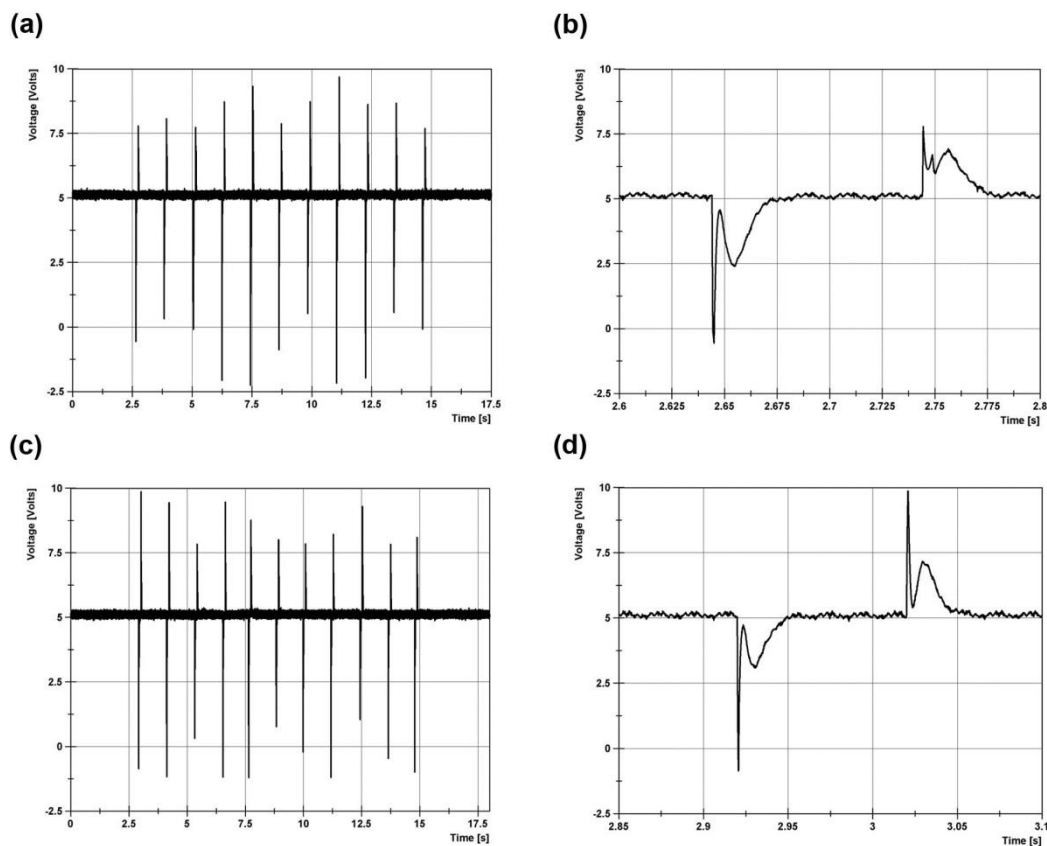
Figure 4.12 The switching polarity test: (a) The generated output and (b) the magnification of the single impulses from the nanowires grown for 1 h, using a capacitance C_r of 100 pF; (c) the generated output and (d) single magnified impulses from the nanowires grown for 7 h (C_r = 390 pF).

4.6   References

[1]   L. E. Greene, B. D. Yuhas, M. Law, D. Zitoun, P. Yang, *Inorg. Chem.* **2006**, *45*, 7535-7543.

[2]   B. Sun, H. Sirringhaus, *Nano Lett.* **2005**, *5*, 2408-2413.

[3]   S. Chen, C. E. Small, C. M. Amb, J. Subbiah, T.-H. Lai, S.-W. Tsang, J. R. Manders, J. R. Reynolds, F. So, *Adv. Energy Mater.* **2012**, *2*, 1333-1337.

[4]   D. C. Reynolds, D. C. Look, B. Jogai, C. W. Litton, T. C. Collins, W. Harsch, G. Cantwell, *Phys. Rev. B* **1998**, *57*, 12151-12155.

[5]   P. Tiwana, P. Docampo, M. B. Johnston, H. J. Snaith, L. M. Herz, *ACS Nano* **2011**, *6*, 5158-5166.

[6]   V. Bhosle, A. Tiwari, J. Narayan, *J. Appl. Phys.* **2006**, *100*, 033713.

[7]   S. Hartner, M. Ali, C. Schulz, M. Winterer, H. Wiggers, *Nanotechnology* **2009**, *20*, 445701.

[8]   J. Fan, F. Güell, C. Fábrega, A. Fairbrother, T. Andreu, A. M. López, J. R. Morante, A. Cabot, *J. Phys. Chem. C* **2012**, *116*, 19496-19502.

[9]   W. Kim, G. Kwak, M. Jung, S. K. Jo, J. B. Miller, A. Gellman, K. Yong, *J. Phys. Chem. C* **2012**, *116*, 16093-16097.

[10]   S. A. Wilson, R. P. J. Jourdain, Q. Zhang, R. A. Dorey, C. R. Bowen, M. Willander, Q. U. Wahab, M. Willander, S. M. Al-hilli, O. Nur, E. Quandt, C. Johansson, E. Pagounis, M. Kohl, J. Matovic, B. Samel, W. van der Wijngaart, E. W. H. Jager, D. Carlsson, Z. Djinovic, M. Wegener, C. Moldovan, R. Iosub, E. Abad, M. Wendlandt, C. Rusu, K. Persson, *Mater. Sci. Eng. R* **2007**, *56*, 1-129.

[11]   L. Vayssieres, K. Keis, S.-E. Lindquist, A. Hagfeldt, *J. Phys. Chem. B* **2001**, *105*, 3350-3352.

[12]   Y. Chen, M. Kim, G. Lian, M. B. Johnson, X. Peng, *J. Am. Chem. Soc.* **2005**, *127*, 13331-13337.

[13]   Z. R. Tian, J. A. Voigt, J. Liu, B. McKenzie, M. J. McDermott, M. A. Rodriguez, H. Konishi, H. Xu, *Nat. Mater.* **2003**, *2*, 821-826.

[14]   T. Andelman, Y. Gong, M. Polking, M. Yin, I. Kuskovsky, G. Neumark, S. O'Brien, *J. Phys. Chem. B* **2005**, *109*, 14314-14318.

[15]   N. O. V. Plank, H. J. Snaith, C. Ducati, J. S. Bendall, L. Schmidt-Mende, M. E. Welland, *Nanotechnology* **2008**, *19*, 465603.

[16]   L. Baeten, B. Conings, H.-G. Boyen, J. D'Haen, A. Hardy, M. D'Olieslaeger, J. V. Manca, M. K. Van Bael, *Adv. Mater.* **2011**, *23*, 2802-2805.

[17]   L. E. Greene, M. Law, J. Goldberger, F. Kim, J. C. Johnson, Y. Zhang, R. J. Saykally, P. Yang, *Angew. Chem. Int. Ed.* **2003**, *42*, 3031-3034.

[18]   A. V. Desai, M. A. Haque, *Sens. Actuators, A* **2007**, *134*, 169-176.

[19]   D. Calestani, M. Zha, R. Mosca, A. Zappettini, M. C. Carotta, V. Di Natale, L. Zanotti, *Sens. Actuators, B* **2010**, *144*, 472-478.

[20]   S. Xu, Y. Qin, C. Xu, Y. Wei, R. Yang, Z. L. Wang, *Nat. Nanotech.* **2010**, *5*, 366-373.

[21]   Z. L. Wang, *Mater. Sci. Eng. R* **2009**, *64*, 33-71.

[22]   Z. L. Wang, J. Song, *Science* **2006**, *312*, 242-246.

[23]   Z. L. Wang, *Adv. Mater.* **2009**, *21*, 1311-1315.

[24]   J.-S. Huang, C.-F. Lin, *J. Appl. Phys.* **2008**, *103*, 014304.

[25]   L. Schmidt-Mende, J. L. MacManus-Driscoll, *Mater. Today* **2007**, *10*, 40-48.

[26]   D. Yu, T. Trad, J. T. McLeskey Jr., V. Craciun, C. R. Taylor, *Nanoscale Res. Lett.* **2010**, *5*, 1333-1339.

[27]   Z. Zhu, T.-L. Chen, Y. Gu, J. Warren, R. M. Osgood Jr., *Chem. Mater.* **2005**, *17*, 4227-4234.

[28]   M. H. Huang, Y. Wu, H. Feick, N. Tran, E. Weber, P. Yang, *Adv. Mater.* **2001**, *13*, 113-116.

[29]   K. L. Choy, *Prog. Mater. Sci.* **2003**, *48*, 57-170.

[30]   M. Htay, Y. Tani, Y. Hashimoto, K. Ito, *J. Mater. Sci.: Mater. Electron.* **2009**, *20*, 341-345.

[31]   M. Breedon, M. B. Rahmani, S.-H. Keshmiri, W. Wlodarski, K. Kalantar-Zadeh, *Mater. Lett.* **2010**, *64*, 291-294.

[32]   B. Coasne, A. Mezy, R. J. M. Pellenq, D. Ravot, J. C. Tedenac, *J. Am. Chem. Soc.* **2009**, *131*, 2185-2198.

[33]   B. Postels, A. Bakin, H.-H. Wehmann, M. Suleiman, T. Weimann, P. Hinze, A. Waag, *Appl. Phys. A* **2008**, *91*, 595-599.

[34]   S. Öztürk, N. Tasaltın, N. Kılınç, H. Yüzer, Z. Z. Öztürk, *Appl. Phys. A* **2010**, *99*, 73-78.

[35]   S. Xu, Z. L. Wang, *Nano Res.* **2011**, *4*, 1013-1098.

[36]   B. Weintraub, Z. Zhou, Y. Li, Y. Deng, *Nanoscale* **2010**, *2*, 1573-1587.

[37]   L. E. Greene, M. Law, D. H. Tan, M. Montano, J. Goldberger, G. Somorajai, P. Yang, *Nano Lett.* **2005**, *5*, 1231-1236.

[38]   G.-R. Li, C.-R. Dawa, Q. Bu, F.-l. Zhen, X.-H. Lu, Z.-H. Ke, H.-E. Hong, C.-Z. Yao, P. Liu, Y.-X. Tong, *Electrochem. Commun.* **2007**, *9*, 863-868.

[39]   L. Vayssieres, *Adv. Mater.* **2003**, *15*, 464-466.

[40]   C. Xu, P. Shin, L. Cao, D. Gao, *J. Phys. Chem. C* **2010**, *114*, 125-129.

[41]   S. H. Lee, H. J. Lee, D. Oh, S. W. Lee, H. Goto, R. Buckmaster, T. Yasukawa, T. Matsue, S.-K. Hong, H. Ko, M.-W. Cho, T. Yao, *J. Phys. Chem. B* **2006**, *110*, 3856-3859.

[42]   D. Grosso, *J. Mater. Chem.* **2011**, *21*, 17033-17038.

[43]   T. Y. Olson, A. A. Chernov, B. A. Drabek, J. H. Satcher, Jr., T. Y.-J. Han, *Chem. Mater.* **2012**.

[44]   K. Biswas, B. Das, C. N. R. Rao, *J. Phys. Chem. C* **2008**, *112*, 2404-2411.

[45]   D. A. Scrymgeour, J. W. P. Hsu, *Nano Lett.* **2008**, *8*, 2204–2209.

[46]   S. N. Cha, J. S. Seo, S. M. Kim, H. J. Kim, Y. J. Park, S. W. Kim, J. M. Kim, *Adv. Mater.* **2010**, *22*, 4726-4730.

[47]   R. Yang, Y. Qin, L. Dai, Z. L. Wang, *Nat. Nanotech.* **2009**, *4*, 34-39.

[48]   H. K. Park, K. Y. Lee, J. S. Seo, J. A. Jeong, H. K. Kim, D. Choi, S. W. Kim, *Adv. Funct. Mater.* **2011**, *21*, 1187-1193.

[49]   B. Kumar, S. W. Kim, *J. Mater. Chem.* **2011**, *21*, 18946-18958.

[50]   R. S. Yang, Y. Qin, L. M. Dai, Z. L. Wang, *Appl. Phys. Lett.* **2009**, *94*, 022905.

[51]   J. W. Cho, C. S. Lee, K. I. Lee, S. M. Kim, S. H. Kim, *Appl. Phys. Lett.* **2012**, *101*, 083905.

5 A Photoactive Porphyrin-Based Periodic Mesoporous Organosilica

This chapter is based on the following publication:

Yan Li, Florian Auras, Florian Löbermann, Markus Döblinger, Jörg Schuster, Laurie Peter, Dirk Trauner, and Thomas Bein,

"A Photoactive Porphyrin-Based Periodic Mesoporous Organosilica",

manuscript in preparation.

The following experiments have been performed in a joint project: The porphyrin-based molecular building block was synthesized by Yan Li and Florian Löbermann, the synthesis and structural characterisation of the periodic mesoporous organosilica was carried out by Yan Li, the analysis of the photoactive properties including fabrication and optoelectronic characterisation of test devices was performed by Florian Auras and Yan Li.

5.1 Introduction

Periodic mesoporous organosilica (PMO) materials have attracted considerable attention due to their structural and functional flexibility,[1-3] rendering them a versatile platform for fundamental research and potential applications in catalysis,[4-6] as adsorbent and functionalized scaffold material,[7-8] and in optoelectronics.[9-12] These materials feature a unique combination of functional organic units and inorganic cross-linking parts within their periodically structured frameworks. In PMOs, each individual organic group is covalently bonded to two or more silicon atoms, such that the bridging organic unit is an integral part of the pore walls, rendering the mesopores well accessible for guest molecules.

To date, numerous organic units from small aliphatic groups to larger aromatic groups have been successfully incorporated in the framework of PMO materials.[13-19] Recent developments of PMO materials were tailored towards the incorporation of photoactive

and electroactive organic functionalities within their frameworks, aiming at their potential application in optoelectronic devices. It has been shown that the incorporation of building blocks with conjugated π-systems can produce fluorescent PMOs[11] or light harvesting systems, in which the energy absorbed by the PMO chromophore can be used for exciting a fluorescent dye that is located inside the pores.[12] Despite the insulating nature of the silica moiety, conductive PMOs can be realized if the packing of the organic building blocks can be controlled such that large π-stacked domains are formed.[20-21]

Porphyrins with their extended conjugated π-systems are capable of absorbing light throughout the visible range and are known to be effective donor materials in small molecule organic photovoltaics.[22] The large planar porphyrin units of a porphyrin-bridged silsesquioxane were reported to self-assemble into ordered superstructures, which consist of square arrays of porphyrin stacks.[23] However, in order to realize a periodically structured mesoporous framework through a soft-templating approach, rational design of the molecular precursor and careful balancing of solubility and reactivity are required.

Here we report that under optimized synthesis conditions a judiciously designed porphyrin-based ethoxysilane precursor (Figure 5.1) can be used to form periodic mesoporous organosilica films through an evaporation-induced self-assembly approach. When employing the triblock copolymer Pluronic F127 as a structure-directing agent the resulting PMO exhibits a face-centred orthorhombic structure with a pore size of 15 nm after template removal. This open-pore nanostructure facilitates the infiltration with an electron acceptor phase and thereby the formation of a bi-continuous network. We observe light-induced charge transfer from the photoactive PMO to the acceptor and charge percolation through the network, leading to a photocurrent between charge carrier selective electrodes. Our results demonstrate the potential of such PMOs with high surface area as light harvesting scaffold for potential application in photosensing applications, photocatalysis, and photoelectrochemistry.
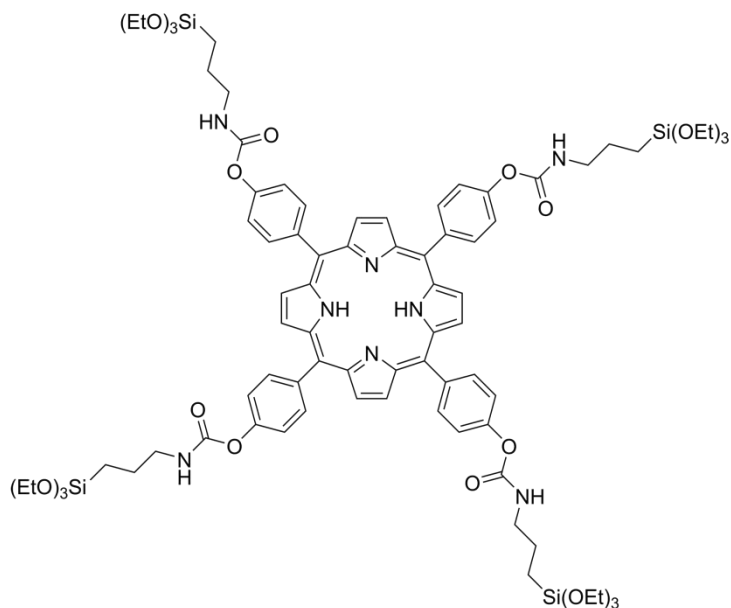
Figure 5.1   Chemical structure of the ethoxysilyl precursor containing porphyrin macrocycles.

5.2   Results and Discussion

5.2.1   Mesostructured porphyrin-bridged PMO films

The porphyrin-based PMO (Por-PMO) was synthesized by an evaporation-induced self-assembly (EISA) approach.[24] Mesostructured Por-PMO thin films were obtained by spin-coating an acidified solution containing the silane precursor and the triblock copolymer Pluronic F127 in ethanol onto flat substrates, followed by slow evaporation of the solvent. Figure 5.2 shows the small-angle X-ray scattering (SAXS) patterns of the as-deposited PMO film (a), after thermal annealing at 120 °C (b), and followed by solvent extraction (c). The as-prepared film exhibits a diffraction signal at $2\theta = 0.86\,°$, which indicates the formation of a periodic mesostructure with a d-spacing of 10.3 nm. After thermal treatment and solvent extraction, the reflection positions are shifted to 0.92 ° and 1.33 °, respectively, corresponding to d-spacings of 9.6 and 6.6 nm. The decreased d-spacings result from film shrinkage along the substrate normal, which is commonly observed for mesoporous thin films after template removal.[21, 25-27]

curve	sample	d-spacing / nm
a	as-prepared	10.2
b	120 °C	9.5
c	extracted	6.6
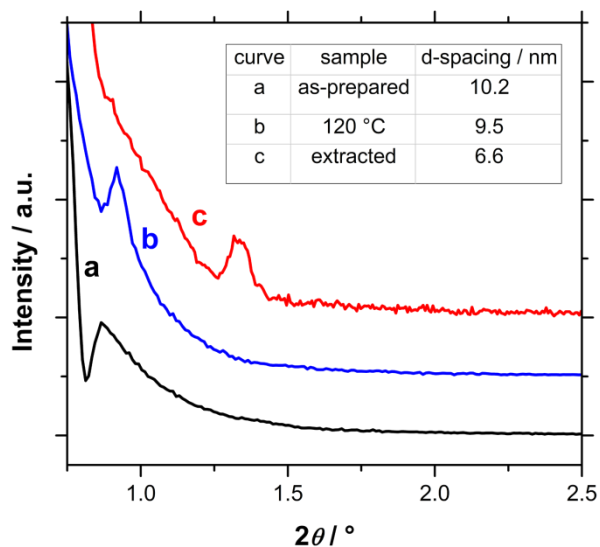
Figure 5.2 SAXS patterns of the Por-PMO films; (a) as prepared, (b) after thermal treatment at 120 °C for 5 hours, (c) after extraction with ethanol. An offset has been added to the curves for clarity.

The 2D-grazing-incidence small-angle X-ray scattering (GISAXS) pattern of the extracted Por-PMO film can be indexed to a face-centred orthorhombic unit cell (*Fmmm*) with the (010) plane parallel to the substrate (Figure 5.3). It resembles the patterns observed for mesoporous silica and carbon films of identical orthorhombic symmetry that were synthesized with the same structure directing agent,[28-31] and is similar to those observed for many mesoporous films after 1D shrinkage.[32-33] The reflections in the GISAXS pattern are doubled due to diffraction of the primary beam after being reflected at the film-substrate interface. Hence, reflections on top of each other (marked with a circle and a square) belong to the same set of lattice planes. The lower empty square denotes the position of the 002 reflection. As it is below the sample 'horizon', its intensity is fully absorbed by the sample. The lattice constants for the extracted Por-PMO film determined by SAXS and 2D-GISAXS are a = 17.5 nm, b = 13.2 nm, and c = 24.8 nm, if one defines the basis vectors **a** and **c** as parallel to the film and **b** along the film normal (Figure 5.3).
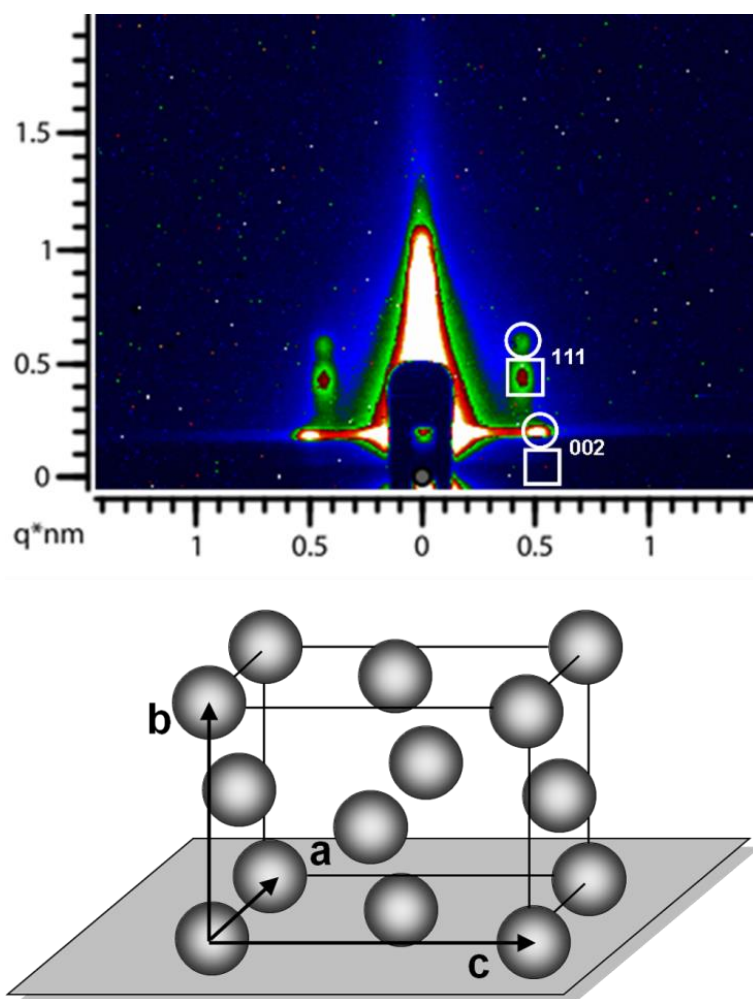
Figure 5.3   2D-GISAXS pattern (top) of the extracted Por-PMO film according to the face-centred orthorhombic symmetry (*Fmmm*) with the (010) plane parallel to the substrate. Schematic illustration of the face-centred orthorhombic unit cell (bottom).
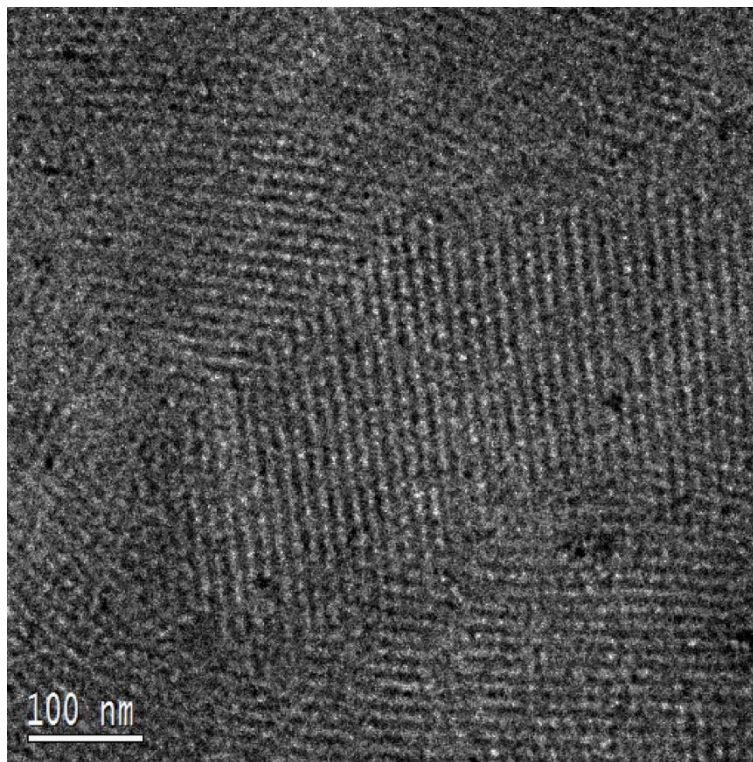
Figure 5.4 Plan-view TEM image of the extracted Por-PMO film. The presence of the ordered domains in the TEM image confirms the preservation of the mesostructure after removal of the surfactant template.

Figure 5.4 shows a representative transmission electron micrograph of the Por-PMO film after solvent extraction. In the plan-view image, the periodic mesostructure of the Por-PMO film with domain sizes in the range of hundreds of nanometers can be observed. The presence of the ordered domains in the TEM image confirms that the mesostructure is preserved after removal of the surfactant template and that its molecular building blocks are cross-linked enough to render it stable against electron-beam damage during TEM characterisation.

To investigate the porosity of the extracted Por-PMO material, nitrogen sorption isotherms of scratched-off films were recorded. Figure 5.5 shows the obtained isotherm with a typical type IV isotherm shape, which is commonly observed for mesoporous materials. The presence of the hysteresis loop indicates that the material features pores that are interconnected by pore openings of smaller diameter. The Por-PMO was found to have a Brunauer-Emmett-Teller (BET) surface area of 364 m^2 g^{-1} and a pore volume of

0.57 cm^3 g^{-1}. The NLDFT pore-size distribution calculated from the adsorption branch indicates that the extracted material has mesopores with a diameter of about 15 nm (inset of Figure 5.5). Such big pores enable the accommodation of large guest molecules into the 3D PMO mesostructure.
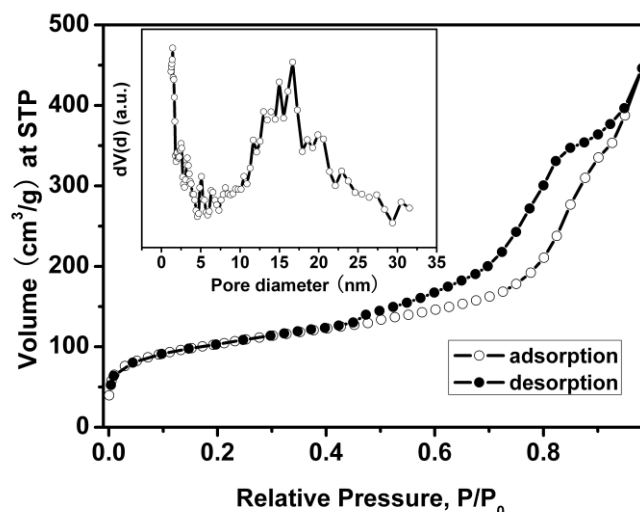
Figure 5.5 Nitrogen adsorption (○) and desorption (●) isotherms of the extracted Por-PMO material with an inset showing the pore size distribution calculated with the NLDFT model from the adsorption branch (○) using a SiO$_2$ kernel assuming cylindrical/spherical pore geometry for the sample.

The extracted Por-PMO material was furthermore investigated by solid-state NMR spectroscopy in order to get detailed information about the chemical environment of both ^{13}C and ^{29}Si nuclei in the PMO material. In the ^{13}C-MAS NMR spectrum (Figure 5.6a), the detected chemical shifts in the range of 100 – 160 ppm are assigned to the carbon atoms in the aromatic ring of the porphyrin moiety.[34-37] The signals at 7.8 ppm (SiCH$_2$), 23.2 ppm (SiCH$_2$CH$_2$), 42.1 ppm (CH$_2$NH), and 155.4 ppm (C=O) can be assigned to the carbon atoms in the propyl isocyanate moiety.[38-42] The ^{13}C-NMR spectrum proves that the porphyrin-based organic bridges in the precursor are robust enough to survive the synthesis conditions. In the solid state ^{29}Si MAS-NMR spectrum (Figure 5.6b), chemical shifts of T1 [CSi(OSi)(OH)$_2$], T2 [CSi(OSi)$_2$(OH)] and T3 [CSi(OSi)$_3$] sites were

observed at -46.5, -57.8 and -65.7 ppm, respectively.[43-44] No signals were observed in the range of -100 to -125 ppm, which would be representative of Qn sites [Qn = $Si(OSi)_n(OH)_{4-n}$], confirming that the Si-C bonds are stable and completely retained in the final mesoporous framework.[45-47]
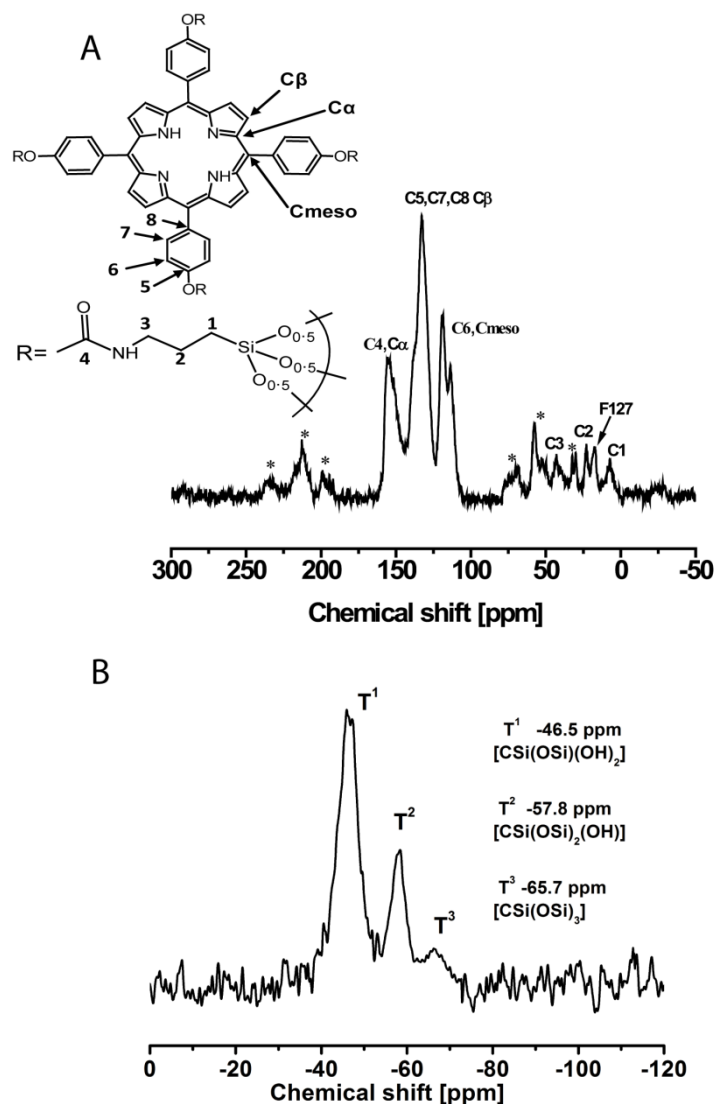
Figure 5.6 (a) ^{13}C-MAS NMR and (b) ^{29}Si-MAS NMR spectra of the extracted Por-PMO material with the corresponding assignments of the different resonances. Signals with asterisk * are the spinning side bands.

5.2.2 Optical properties

The UV-Vis spectra of a dilute solution containing the porphyrin-bridged precursor as well as that of the extracted Por-PMO film are shown in Figure 5.7. For the dilute precursor solution, a strong Soret band is observed at 416 nm. Additionally, four bands are observed at 514, 550, 590 and 651 nm, which can be assigned to the Q-band signals that are typical for non-aggregated, free-base porphyrin units.[37, 48-49] The absorption bands of the extracted Por-PMO film have similar shape but are red-shifted compared to the spectrum of the precursor solution. Similar red-shifts have been observed in other systems with assembled porphyrin macrocycles, and are believed to result from densely packed molecular aggregates that allow electronic coupling and energy transfer among the porphyrin building blocks.[23, 50-51]
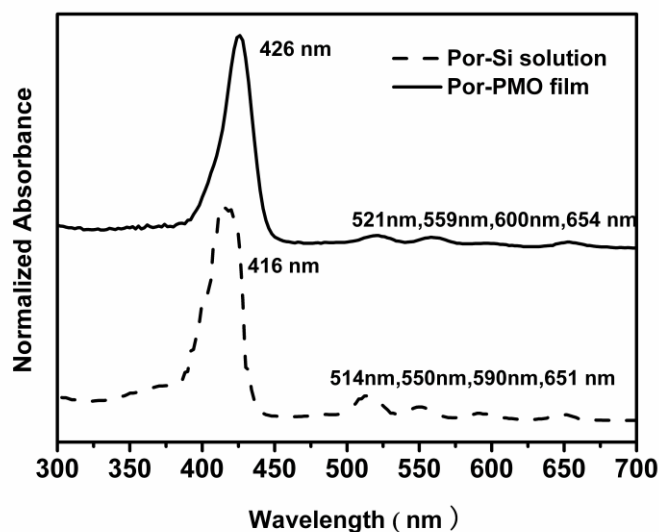
Figure 5.7 UV-Vis absorption spectra of the extracted Por-PMO film (solid line) and that of a dilute solution containing 10^{-5} M porphyrin organosilica precursor in THF (dashed line). For clarity, an offset is added to the black curve.

5.2.3 Optoelectronic properties

In order to investigate the photoactive and electronic properties of the Por-PMO we prepared films of about 100 nm thickness on ITO-coated glass substrates.

For the measurements in an aqueous electrolyte containing 0.1 M KNO_3 and 1 mM H_2O_2, the Por-PMO film was connected as working electrode and a Pt wire was used as counter-electrode (Figure 5.8). The time-resolved photocurrent response and the spectrally resolved response were investigated.
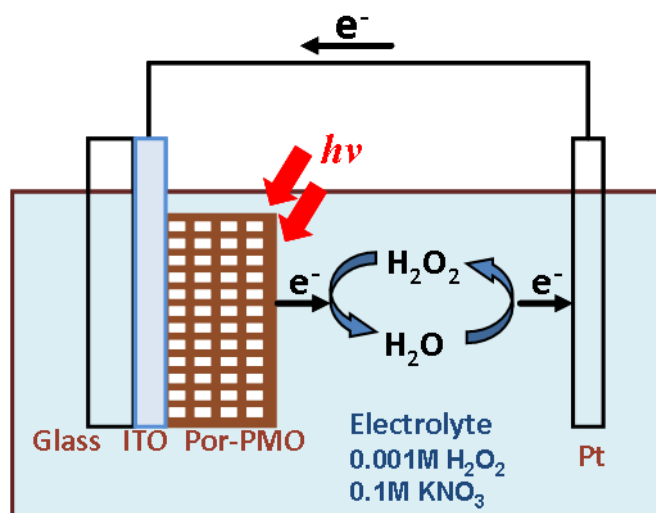
Figure 5.8 Illustration of the set-up for optoelectrochemical experiments in electrolyte containing 0.1 M KNO_3 and 1 mM H_2O_2.

Current transients were recorded at different intensities of simulated solar light with illumination from the film side (Figure 5.9a). A current pulse is generated upon illumination and quickly decays to a lower steady-state current. A pulse of similar amplitude but opposite sign is observed when switching the light off. These anodic and cathodic current spikes are well-known for films of organic semiconductors in electrolytes and are believed to originate from charging and discharging of surface states.[52-54] The sign of the photocurrent identifies the Por-PMO film as a p-type semiconductor, indicating that electron-hole pairs are generated upon illumination and the electrons are transferred to the electrolyte, whereas the holes are transported within the Por-PMO film.

In addition to the time-resolved photocurrent we recorded the spectrally resolved photocurrent at short circuit (Figure 5.9b, dashed line). Above 500 nm, the spectrum of

external quantum efficiency (EQE), which is the ratio of collected electrons to incident photons, closely resembles the absorbance spectrum of the Por-PMO film. However, around 420 nm, where the porphyrin has its strongest absorption, the current output is unexpectedly low. Since the absorbance in this wavelength region is far higher than at longer wavelengths, incident photons are absorbed mainly close to the film surface. Consequently, holes have to travel through the entire depth of the porphyrin network and might recombine with electrons from the electrolyte before they can be collected at the contact. In contrast to this, at longer wavelengths the light intensity does not vary dramatically throughout the depth of the film and thus the generation of electron-hole pairs is much more uniformly distributed over the entire film thickness, which seems more favourable for current collection.
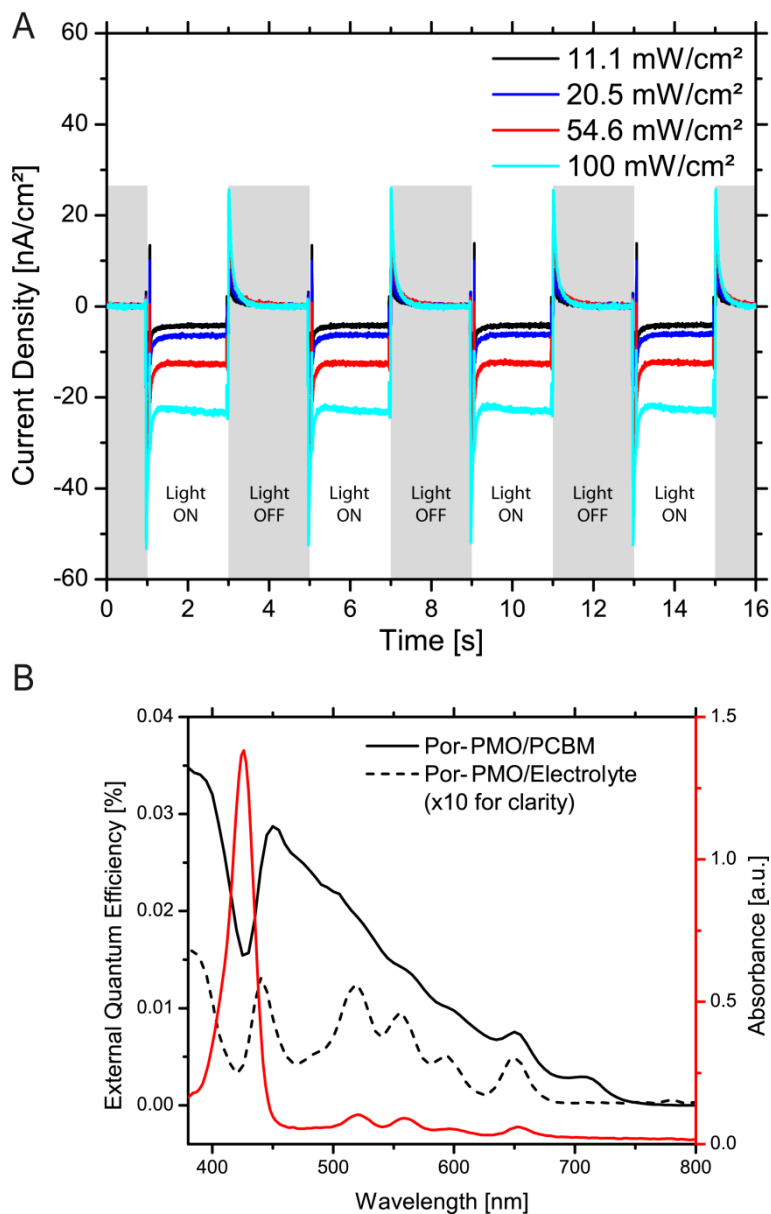
Figure 5.9 (a) Time-resolved photocurrent response of the extracted Por-PMO film deposited on ITO in an aqueous electrolyte containing 0.1 M KNO_3 and 1 mM H_2O_2 (active area is 1 cm^2). The experiment was carried out using simulated AM1.5G solar light of different light intensities. (b) External quantum efficiency of a Por-PMO film in the electrolyte and of the Por-PMO:PCBM solid-state device, and UV-Vis spectrum of a Por-PMO film. The spectrum measured in the electrolyte was multiplied by 10 for clarity.

We also combined the hole-transporting Por-PMO films with an electron acceptor to form a three-dimensional solid-state heterojunction. Soaking the extracted mesoporous films in a solution of [6,6]-phenyl-C_{61}-butyric acid methyl ester (PCBM), followed by

spin-coating leads to infiltration of the electron-transporting species into the mesopores (confirmed by N_2 sorption, Figure 5.12) and the formation of an additional PCBM overlayer of about 20 nm. This overlayer is desired in order to form an electron-selective contact with the Ag back electrode and to avoid short-circuiting the device through direct contact of the Ag with the PMO (configuration of the device illustrated in Figure 5.10).
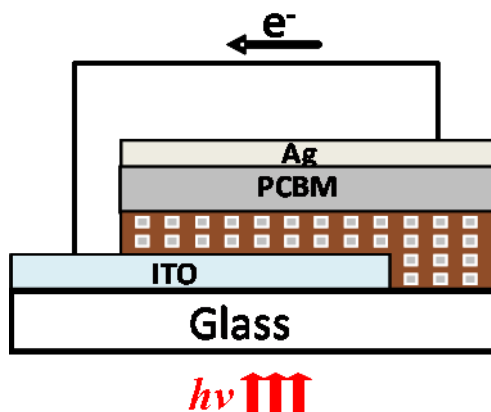
Figure 5.10 Illustration of the configuration of the solid-state device based on the mesostructured PMO film.

The external quantum efficiency spectrum of the device follows the absorbance trend of the Por-PMO film (Figure 5.9b, solid line). Compared to the measurements in an electrolyte the photocurrent response in the blue and UV part of the spectrum is much higher, which we attribute to a contribution of the PCBM. The observed photocurrent appears to be a superposition of excitons generated in the Por-PMO followed by electron injection into the PCBM, and excitons generated upon light absorption by the PCBM followed by hole injection into the Por-PMO. As already observed for the liquid electrolyte sample, the photocurrent generated at the strongest absorption peak of the porphyrin framework is in fact lower than at neighbouring wavelengths. At around 420 nm, since the illumination is through the ITO substrate in the case of the solid-state Por-PMO/PCBM device, most excitons are created close to the ITO front contact. Electrons in the PCBM would have to diffuse a long way through the interpenetrating network and might eventually recombine with holes in the PMO film before being

collected by the Ag contact. Again, the more uniform charge generation throughout the entire film seems to be favourable for current output.

5.3 Conclusion

A novel periodic mesoporous organosilica film material was successfully synthesized by polycondensation of a specially designed porphyrin-containing organosilane precursor in the presence of a surfactant template. The resulting PMO film possesses a three-dimensional orthorhombic mesostructure with a large pore size of 15 nm. The PMO film exhibits broad-band light absorption due to the incorporated porphyrin moieties. We have demonstrated the possibility of forming a three-dimensional heterojunction by infiltrating the PMO film with an electron acceptor phase and were able to prove light-induced charge transfer from the porphyrin PMO to the acceptor and charge percolation through the porphyrin PMO, which results in a stable photocurrent output upon simulated solar illumination. Our results demonstrate the potential of chromophore-containing PMOs with high surface area as light harvesting scaffolds, which render them structurally well-defined model systems for studying photoactive building blocks.

5.4 Experimental Section

5.4.1 Preparation of porphyrin-based PMO films

0.075 g (0.045 mmol) porphyrin-containing precursor (Figure 5.1, synthetic procedures in Chapter 5.5) and 0.075 g (0.006 mmol) Pluronic F127 were first dissolved in 2.4 mL ethanol. Next, 0.08 mL of 0.1 M HCl (8.0×10^{-3} mmol) were added and the resulting solution was stirred at room temperature for 4 h. Finally, the aged sol was spin-coated on glass slides (2×2 cm^2) at 3000 rpm for 30 s. The obtained films were dried in air at room temperature overnight. In order to fully condense the silica units and remove the surfactant, the films were heated in flowing N$_2$ with a ramp of 1 °C min^{-1} to 120 °C and kept at this temperature for 5 h and finally refluxed in absolute ethanol for 2 h.

5.4.2 Structural characterisation

Small-angle X-ray scattering (SAXS) was carried out using a Bruker D8 Discover with Ni-filtered CuK$_\alpha$-radiation (0.154 nm) and a position-sensitive detector (LynxEye). For two-dimensional grazing-incidence small-angle X-ray scattering (2D-GISAXS) characterisation, a SAXSess system by Anton Paar (CuK$_\alpha$-radiation, sample-detector distance 306.7 mm) with a CCD detector (PI-SCX:4300, Roper Scientific) was used. The samples were measured for 10 h with a tilt angle of 0.27° with respect to the primary beam. Transmission electron microscopy (TEM) was performed using a FEI Titan 80-300 instrument equipped with a field emission gun operated at 300 kV. Nitrogen sorption measurements were carried out at -196 °C using an Autosorb-1 (Quantachrome Instruments). Samples were degassed at 150 °C for 12 h in vacuum prior to measurement. For the sorption experiments thicker films were synthesized by drop-casting the same solution as described above on flat glass substrates. After thermal treatment, these thick films were scratched off from the glass slides and refluxed in absolute ethanol to remove the surfactant template. The Brunauer-Emmett-Teller (BET) surface area was calculated using experimental points at a relative pressure range of $p/p_0 = 0.05$-0.20. The total pore volume was calculated from the N_2 amount adsorbed at the highest p/p_0 ($p/p_0 = 0.98$). NLDFT pore size distributions were calculated from the adsorption branch using a SiO_2 kernel and assuming a cylindrical/spherical pore geometry. Solid-state ^{13}C and ^{29}Si NMR experiments were performed on a Bruker Avance-Ш 500 spectrometer (11.7 Tesla) operating at frequencies of 125.8 MHz for ^{13}C and 99.4 MHz for ^{29}Si. ^{13}C(^{1}H) CP-MAS spectra were acquired using a 90° pulse length of 2.5 µs (3.7 dB) with cross-polarisation contact time of 5 ms and a recycle delay of 2 s. ^{29}Si(^{1}H) CP-MAS experiments were conducted using a 90° pulse length of 2.5 µs (3.7 dB) with cross-polarisation contact time of 5 ms and a recycle delay of 2 s.

5.4.3 Photoelectrochemical characterisation

Por-PMO films for photoelectrochemical characterisation were synthesized on indium tin oxide coated glass (VisionTek, 150 nm ITO, 12-15 ohms/sq).

UV-Vis measurements were performed on a Hitachi U3501 spectrophotometer equipped with an integrating sphere. Absorbance spectra were recorded in transmission geometry with plain ITO as reference.

For the measurements in an electrolyte, the ITO substrates were cut into pieces of 1×1.5 cm^2. A 5 mm wide contact area on one side of the substrate was masked during the deposition of the PMO film, resulting in an active area of 1 cm^2. After extraction of the template the blank part of the ITO was contacted with a copper wire using silver paste and then this contact area was sealed with poly(dimethylsiloxane) in order to avoid direct contact between the ITO and the electrolyte. Photoelectrochemical measurements were performed with the Por-PMO film as working electrode and a platinum wire as counter electrode in an aqueous electrolyte containing 0.1 M KNO$_3$ and 1 mM H$_2$O$_2$.

Solid-state devices were fabricated on patterned ITO substrates. After deposition of the PMO layer and subsequent extraction of the template, the films (1.5×1.5 cm^2) were immersed overnight into a solution of [6, 6]-phenyl-C$_{61}$-butyric acid methyl ester (PCBM, 3 mg mL^{-1} in chlorobenzene) to enhance the infiltration of the PCBM into the mesopores. The films were then taken from this solution and immediately spin-coated at 1000 rpm for 60 s, which resulted in a thin and homogeneous layer of PCBM on top of the PMO film. Finally, 70 nm thick silver contacts were sputter-deposited through a shadow mask, yielding an active area of 16 mm^2. The samples were illuminated through a 12 mm^2 mask and measured in air.

For recording current transients the samples were illuminated with white light from an AM1.5G solar simulator (Solar Light Model 16S) at 100 mW cm^{-2}, which was modulated by a shutter. Illumination was carried out from the film side in case of the measurements in an electrolyte and through the ITO substrate in case of the solid-state devices. Lower light intensities were realized with a set of calibrated reflective neutral density filters. The signal was recorded using a low noise preamplifier (Femto DLPCA-200) and an oscilloscope (Tektronix DPO2012).

External quantum efficiency (EQE) measurements were performed at short circuit. Monochromatic light was obtained from a 150 W xenon lamp in combination with a

monochromator and order-sorting filters. The slits were adjusted such that the FWHM was 5 nm at a light intensity of approximately 2 mW cm^{-2}. All light intensities were calibrated with a Fraunhofer ISE certified silicon reference cell equipped with a KG5 filter. The monochromatic light was modulated using an optical chopper at a frequency of 4 Hz for measurements in an electrolyte and 12 Hz in case of the solid state devices. The signal was detected via a low noise pre-amplifier (Femto DLPCA-200) and a lock-in amplifier (Signal Recovery 7265). The modulation frequency was chosen slow enough such that the current response of the sample was square-like.

5.5   Supporting Information

5.5.1   Synthetic procedures of the porphyrin-containing ethoxysilyl precursor
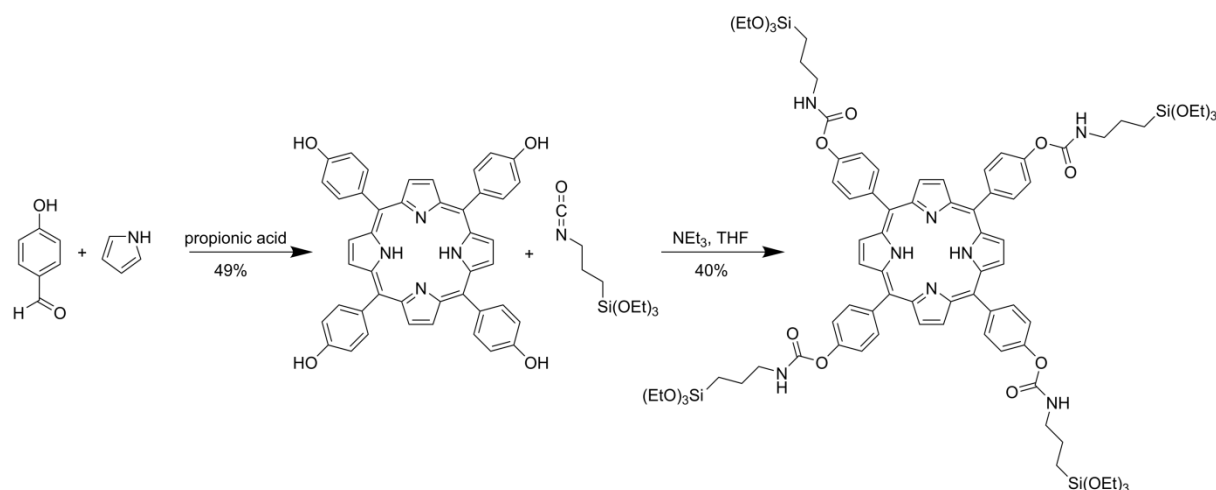
Figure 5.11   Synthetic route for the porphyrin-bridged ethoxysilyl precursor.

Meso-tetra(*p*-hydroxy)phenyl porphyrin[55]

4-Hydroxybenzaldehyde (3.6 g, 30 mmol, 1.0 *eq.*) was dissolved by refluxing in propionic acid (150 mL). Upon addition of pyrrole (C$_4$H$_4$NH) (2.0 g, 30 mmol, 1.0 *eq.*) the reaction mixture was refluxed for further 30 min. Afterwards the solution was slowly cooled to 0 °C for 15 min. The resulting precipitate was excessively washed with CHCl$_3$ (200 mL) and then dissolved in a mixture of acetone (100 mL) and CHCl$_3$ (50 mL), washed with saturated sodium bicarbonate solution (2×50 mL), brine (3×50 mL), dried,

filtered and concentrated. The crude product was purified by repetitive silica gel chromatography (1% MeOH in CHCl$_3$) to afford 2.5 g (49%) of *meso*-tetra(*p*-hydroxy)phenyl porphyrin as a purple solid.

Analysis data:

IR (neat): ν (cm^{-1}) = 3313 (br), 1700 (m), 1607 (s), 1509 (s), 1350 (s), 1213 (vs), 1171 (vs), 966 (s), 794 (vs), 728 (s);

^{1}H NMR (300 MHz, DMSO-*d6*): δ = 9.94 (s, 4H), 8.87 (s, 8H), 8.00 (d, 8H, *J* = 8.5), 7.21 (dd, 8H, *J* = 1.2, 8.5), -2.88(s, 2H);

^{13}C NMR (100 MHz, DMSO-*d6*): δ = 157.8, 157.7, 136.0, 120.4, 116.1, 114.4;

MS (EI) calcd. for C$_{44}$H$_{30}$N$_4$O$_4$ (M$^+$): 687.2267; found: 687.2271.

Porphyrin-containing ethoxysilyl precursor

A dry Schlenk tube was charged with *meso*-tetra(*p*-hydroxy)phenyl porphyrin (204 mg, 0.30 mmol, 1 *eq.*) in dry THF (15 mL). To the solution 3-isocyanatopropyltriethoxysilane (445 mg, 1,8 mmol, 6 *eq.*) and triethylamine (9.11 mg, 0.09 mmol, 0.3 *eq.*) were added at room temperature under argon atmosphere. The reaction mixture was heated to 80 °C for 4 h. After concentration *in vacuo*, filtration and washing with ethyl acetate (50 mL) all volatiles were removed. The resulting oily residue was taken up in a small amount of EtOAc and precipitated with hexane. The precipitate was collected after centrifugation. This procedure was repeated five times, after which the resulting solid was dried in high vacuum to obtain 200 mg (40%) of the title compound as purple solid.

Analysis data:

IR (neat): ν (cm^{-1}) = 3315 (br), 2971 (w), 2926 (vw), 2884 (vw), 1714 (vs), 1608 (s), 1586 (w), 1498 (s), 1470 (w), 1349 (s), 1205 (vs), 1166 (s), 1069 (vs), 965 (w);

^{1}H NMR (400 MHz, CDCl$_3$): δ = 8.88 (s, 8H), 8.18 (d, 8H, *J* = 8.4), 7.53 (d, 8H, *J* = 8.4), 5.60 (t, 4H, *J* = 5.9), 3.91 (dt, 24H, *J* = 6.2, 7.0), 3.42 (dd, 8H, *J* = 6.6, 13.0), 1.88-1.78 (m, 8H), 1.30 (td, 36H, *J* = 1.6, 7.0), 0.82-0.76 (m, 8H), -2.83 (s, 2H);

^{13}C NMR (100 MHz, CDCl$_3$): δ = 154.7, 151.1, 138.9, 135.7, 135.2, 119.8, 119.3, 113.7, 58.6, 43.7, 23.2, 18.3, 7.8;

MS (ESI) calcd. for C$_{84}$H$_{115}$N$_8$O$_{20}$Si$_4$ [M$^+$H]$^+$: 1667.7305; found: 1667.7306.

5.5.2   *Nitrogen sorption isotherms of Por-PMO after infiltration with PCBM*

The decrease in surface area, NLDFT pore diameter, and pore volume of Por-PMO after infiltration of PCBM clearly indicates the presence of the PCBM molecules in the large mesopores.

sample name	BET surface (m^{2}g^{-1})	pore size (nm)	pore volume (cm^{3}g^{-1})
Por-PMO	364	15.4	0.57
Por-PMO/PCBM	202	11.7	0.25
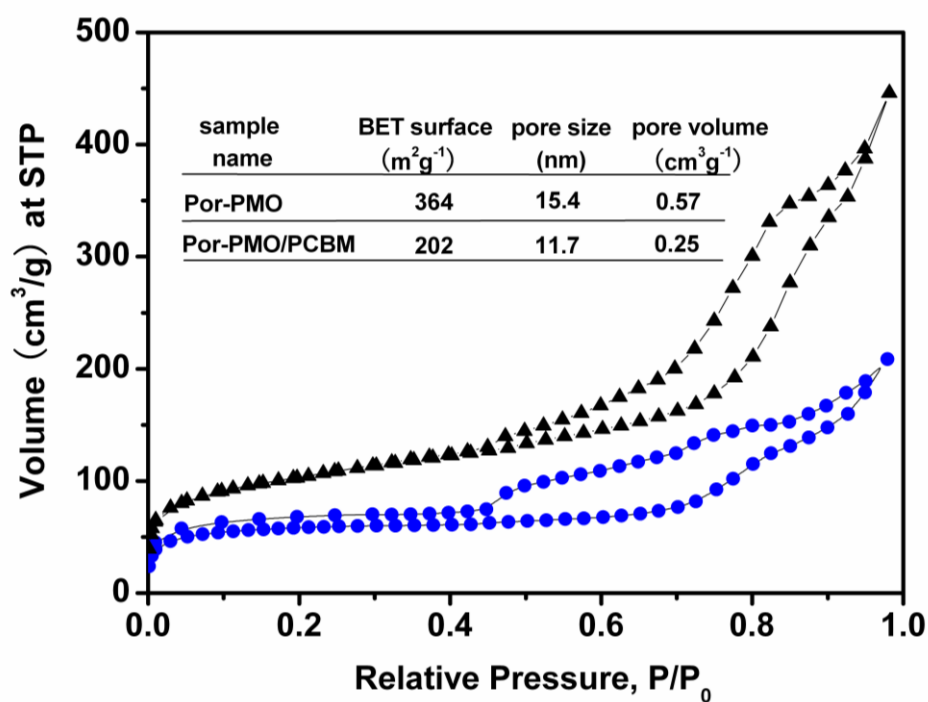
Figure 5.12   Nitrogen sorption isotherms of the extracted Por-PMO sample before (▲) and after (●) infiltration of PCBM molecules in the mesopores. Pore sizes are calculated by NLDFT method from the adsorption branch using a SiO$_2$ kernel assuming cylindrical/spherical pore geometry for the sample.

5.6   References

[1]   T. Asefa, M. J. MacLachlan, N. Coombs, G. A. Ozin, *Nature* **1999**, *402*, 867-871.

[2]   S. Inagaki, S. Guan, Y. Fukushima, T. Ohsuna, O. Terasaki, *J. Am. Chem. Soc.* **1999**, *121*, 9611-9614.

[3]   B. J. Melde, B. T. Holland, C. F. Blanford, A. Stein, *Chem. Mater.* **1999**, *11*, 3302-3308.

[4]   Q. Yang, J. Liu, L. Zhang, L. Can, *J. Mater. Chem.* **2009**, *19*, 1945-1955.

[5]   A. Kuschel, S. Polarz, *J. Am. Chem. Soc.* **2010**, *132*, 6558-6565.

[6]   E.-Y. Jeong, M. B. Ansari, S.-E. Park, *ACS Catal.* **2011**, *1*, 855-863.

[7]   C. Li, J. Liu, X. Shi, J. Yang, Q. Yang, *J. Phys. Chem. C* **2007**, *111*, 10948-10954.

[8]   M. Park, S. S. Park, M. Selvaraj, D. Zhao, C.-S. Ha, *Microporous Mesoporous Mater.* **2009**, *124*, 76-83.

[9]   R. Hernandez, A.-C. Franville, P. Minoofar, B. Dunn, J. I. Zink, *J. Am. Chem. Soc.* **2001**, *123*, 1248-1249.

[10]   P. N. Minoofar, R. Hernandez, S. Chia, B. Dunn, J. I. Zink, A.-C. Franville, *J. Am. Chem. Soc.* **2002**, *124*, 14388-14396.

[11]   N. Mizoshita, Y. Goto, T. Tani, S. Inagaki, *Adv. Funct. Mater.* **2008**, *18*, 3699-3705.

[12]   S. Inagaki, O. Ohtani, Y. Goto, K. Okamoto, M. Ikai, K.-i. Yamanaka, T. Tani, T. Okada, *Angew. Chem. Int. Ed.* **2009**, *48*, 4042-4046.

[13]   A. Sayari, W. Wang, *J. Am. Chem. Soc.* **2005**, *127*, 12194-12195.

[14]   J. Morell, M. Güngerich, G. Wolter, J. Jiao, M. Hunger, P. J. Klar, M. Fröba, *J. Mater. Chem.* **2006**, *16*, 2809-2818.

[15]   H. Takeda, Y. Goto, Y. Maegawa, T. Ohsuna, T. Tani, K. Matsumoto, T. Shimada, S. Inagaki, *Chem. Commun.* **2009**, *45*, 6032-6034.

[16]   C. Vercaemst, P. E. de Jongh, J. D. Meeldijk, B. Goderis, F. Verpoort, P. Van Der Voort, *Chem. Commun.* **2009**, *45*, 4052-4054.

[17]   M. P. Kapoor, Q. Yang, S. Inagaki, *J. Am. Chem. Soc.* **2002**, *124*, 15176-15177.

[18]   N. Mizoshita, T. Tani, S. Inagaki, *Chem. Soc. Rev.* **2011**, *40*, 789-800.

[19]   M. Cornelius, F. Hoffmann, M. Fröba, *Chem. Mater.* **2005**, *17*, 6674-6678.

[20]   N. Mizoshita, T. Tani, S. Inagaki, *Adv. Funct. Mater.* **2011**, *21*, 3291-3296.

[21]   N. Mizoshita, M. Ikai, T. Tani, S. Inagaki, *J. Am. Chem. Soc.* **2009**, *131*, 14225-14227.

[22]   M. V. Martínez-Díaz, G. de la Torre, T. Torres, *Chem. Commun.* **2010**, *46*, 7090-7108.

[23]   H. Peng, Y. Lu, *Adv. Mater.* **2008**, *20*, 797-800.

[24]   C. J. Brinker, Y. Lu, A. Sellinger, H. Fan, *Adv. Mater.* **1999**, *11*, 579-585.

[25]   H. Miyata, K. Kuroda, *Chem. Mater.* **2000**, *12*, 49-54.

[26]   J. Schuster, R. Köhn, A. Keilbach, M. Döblinger, H. Amenitsch, T. Bein, *Chem. Mater.* **2009**, *21*, 5754-5762.

[27]   E. Ortel, T. Reier, P. Strasser, R. Kraehnert, *Chem. Mater.* **2011**, *23*, 3201-3209.

[28]   P. Falcaro, D. Grosso, H. Amenitsch, P. Innocenzi, *J. Phys. Chem. B* **2004**, *108*, 10942-10948.

[29]   V. N. Urade, H. W. Hillhouse, *J. Phys. Chem. B* **2005**, *109*, 10538-10541.

[30]   S. Tanaka, Y. Katayama, M. P. Tate, H. W. Hillhouse, Y. Miyake, *J. Mater. Chem.* **2007**, *17*, 3639-3645.

[31]   J. Schuster, R. Köhn, M. Döblinger, A. Keilbach, H. Amenitsch, T. Bein, *J. Am. Chem. Soc.* **2012**, *134*, 11136-11145.

[32]   M. P. Tate, V. N. Urade, J. D. Kowalski, T.-c. Wei, B. D. Hamilton, B. W. Eggiman, H. W. Hillhouse, *J. Phys. Chem. B* **2006**, *110*, 9882-9892.

[33]   L. Song, D. Feng, C. G. Campbell, D. Gu, A. M. Forster, K. G. Yager, N. Fredin, H.-J. Lee, R. L. Jones, D. Zhao, B. D. Vogt, *J. Mater. Chem.* **2010**, *20*, 1691-1701.

[34]   L. Frydman, A. C. Olivieri, L. E. Díaz, A. Valasinas, B. Frydman, *J. Am. Chem. Soc.* **1988**, *110*, 5651-5661.

[35]   J.-Y. Tung, J.-H. Chen, F.-L. Liao, S.-L. Wang, L.-P. Hwang, *Inorg. Chem.* **1998**, *37*, 6104-6108.

[36]   X. Feng, L. Chen, Y. Dong, D. Jiang, *Chem. Commun.* **2011**, *47*, 1979-1981.

[37]   S. Wan, F. Gándara, A. Asano, H. Furukawa, A. Saeki, S. K. Dey, L. Liao, M. W. Ambrogio, Y. Y. Botros, X. Duan, S. Seki, J. F. Stoddart, O. M. Yaghi, *Chem. Mater.* **2011**, *23*, 4094-4097.

[38]   J.-S. Lee, S.-W. Ryu, *Macromolecules* **1999**, *32*, 2085-2087.

[39]   J. Bass, D., A. Katz, *Chem. Mater.* **2003**, *15*, 2757-2763.

[40]   I. V. Mel'nik, O. V. Lyashenko, Y. L. Zub, A. A. Chuiko, D. Cauzzi, G. Predieri, *Russ. J. Gen. Chem.* **2004**, *74*, 1782-1788.

[41]   B. Yan, D.-J. Ma, *J. Solid State Chem.* **2006**, *179*, 2059-2066.

[42]   B. Francis, D. B. A. Raj, M. L. P. Reddy, *Dalton Trans.* **2010**, *39*, 8084-8092.

[43]   M. Takafuji, N. Azuma, K. Miyamoto, S. Maeda, H. Ihara, *Langmuir* **2009**, *25*, 8428-8433.

[44]   B. Radi, R. M. Wellard, G. A. George, *Macromolecules* **2010**, *43*, 9957-9963.

[45]   A. Keilbach, M. Döblinger, R. Köhn, H. Amenitsch, T. Bein, *Chem. Eur. J.* **2009**, *15*, 6645-6650.

[46]   M. A. Wahab, C. He, *Langmuir* **2009**, *25*, 832-838.

[47]   Y. Li, A. Keilbach, M. Kienle, Y. Goto, S. Inagaki, P. Knochel, T. Bein, *J. Mater. Chem.* **2011**, *21*, 17338-17344.

[48]   M. A. García-Sánchez, A. Campero, *J. Non-Cryst. Solids* **2001**, *296*, 50-56.

[49]   M. A. García-Sánchez, A. Campero, *J. Non-Cryst. Solids* **2004**, *333*, 226-230.

[50]   N. C. Maiti, S. Mazumdar, N. Periasamy, *J. Phys. Chem. B* **1998**, *102*, 1528-1538.

[51]   V. De la Luz, M. A. García-Sánchez, A. Campero, *J. Non-Cryst. Solids* **2007**, *353*, 2143-2149.

[52]   T. Oekermann, D. Schlettwein, N. I. Jaeger, *J. Electroanal. Chem.* **1999**, *462*, 222-234.

[53]   D. Schlettwein, E. Karmann, T. Oekermann, H. Yanagi, *Electrochim. Acta* **2000**, *45*, 4697-4704.

[54]   T. Oekermann, D. Schlettwein, N. I. Jaeger, *J. Phys. Chem. B* **2001**, *105*, 9524-9532.

[55]   A. Kumar, S. Maji, P. Dubey, G. J. Abhilash, S. Pandey, S. Sarkar, *Tetrahedron Lett.* **2007**, *48*, 7287-7290.

6 Light-Induced Charge Carrier Generation in a Thienothiophene-Based Covalent Organic Framework

The following studies have been performed in a joint project: Thin films of the covalent organic framework were prepared and analysed by Mirjam Dogru, the thienothiophene building block was synthesized by Veronika Werner in the group of Prof Knochel. Optoelectronic characterisation and device fabrication and characterisation were performed by Florian Auras.

6.1 Introduction

Thiophene-based molecules and polymers are the most prominent materials in highly efficient organic solar cells.[1-4] While impressive advances in device efficiency have been made during the past years, precise control of the nanoscale morphology and molecular packing at the interpenetrated donor-acceptor heterojunction remains a key issue. We have recently reported a photovoltaic device based on a crystalline and porous covalent organic framework (COF).[5] The reaction scheme for the co-condensation of the thienothiophene-containing COF (TT-COF) is presented in Figure 6.1. An interdigitated heterojunction was formed upon infiltration of the COF with [6,6]-phenyl C_{61} butyric acid methyl ester and a stable photocurrent of $0.21\,\mathrm{mA\,cm^{-2}}$ under simulated solar illumination was obtained. Here we studied the influence of different fullerene-based acceptors inside COF thin films on the photoinduced charge transfer. We then prepared devices using a series of acceptors with different energy levels and found that very high open-circuit voltages of above 1.2 V can be reached in an optimised device architecture.

Figure 6.1   Reaction scheme for the co-condensation of TT-COF.

6.2   Results and Discussion

6.2.1   Thin film preparation

Thin films of the thienothiophene-containing covalent organic framework (TT-COF) were synthesized on MoO_x-covered indium tin oxide (ITO) substrates. Reduced metal oxides have proven to be an excellent substitute for the highly hygroscopic and corrosive PEDOT:PSS that is commonly used as hole-selective contact in organic photovoltaics.[6] COF films grown on thermally evaporated MoO_x were found to adhere strongly to the substrate and to exhibit very homogeneous coverage (Figure 6.2).
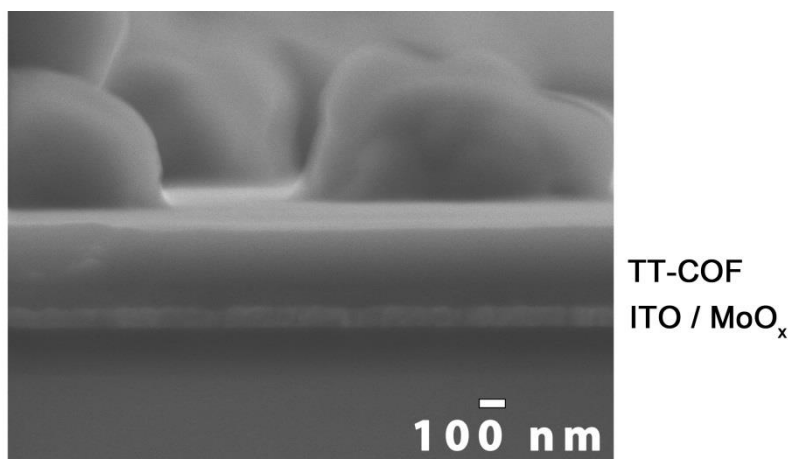
Figure 6.2 Cross-sectional scanning electron micrograph of a TT-COF film grown for 72 h at 100 °C. The thickness of the dense COF layer is 270 – 300 nm. The island-like structures in the background are precipitates from the growth solution. As we do not observe any starting material or other phases in XRD, we assume that they consist also of TT-COF.

The crystallinity of the TT-COF thin films was monitored with X-ray diffraction. In Figure 6.3 the TT-COF films show weak reflections at low 2Theta values and an increased 001 reflection at 26 ° compared to the bulk TT-COF. This indicates a preferred orientation of the TT-COF with the π-stacking direction parallel to the substrate. Since the charge transport in these systems is anticipated along the π-stack, the TT-COF films with a preferred orientation might be beneficial for efficient charge transport in the COF-based solar cell devices.
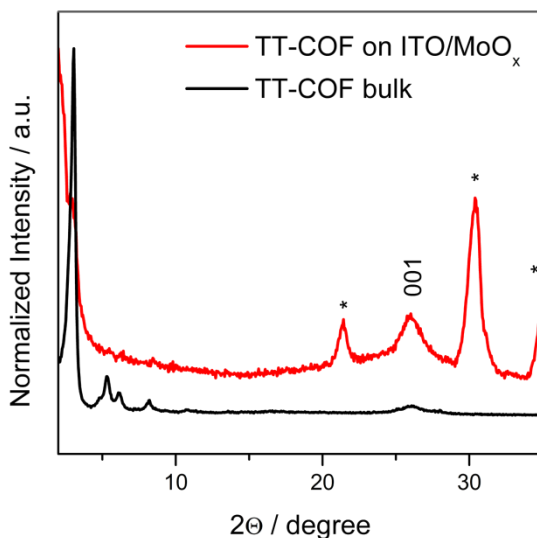
Figure 6.3   XRD Pattern of TT-COF bulk powder (black) and TT-COF film (red) on the MoO_x/ITO substrate. The significant decrease in intensity of the reflections in the small-angle range and the pronounced 001 reflection at 26° indicate a preferential growth of TT-COF with pores perpendicular to the substrate. The asterisks indicate the reflections originating from the ITO substrate.

6.2.2   Photo-induced charge transfer

The TT-COF is known to exhibit photoluminescence (PL) if excited with UV light.[5] It has been shown that the emission can be completely quenched if an electron acceptor, such as [6,6]-Phenyl C_{n+1} butyric acid methyl ester (n = 60, 70; [n]PCBM) is placed within the exciton diffusion length of the COF. In this study we utilize PL quenching to analyse the infiltration of COF thin films with electron acceptors. Since the exciton diffusion length in organic materials is typically on the order of 10 nm, significant PL quenching would require infiltration of the acceptor molecules throughout the entire film.

Upon excitation at 325 nm we observe a broad PL signal with a maximum at 445 nm (Figure 6.4). This signal is reduced significantly after infiltration of the film with PCBM. We observe that the degree of quenching is much higher for the better soluble [70]PCBM than for [60]PCBM (97% vs. 78%). Since we have shown quantitative PL quenching also with [60]PCBM for TT-COF powders,[5] we attribute the observed differences in the case

of thin films to a different degree of interpenetration of the donor and the acceptor networks. Thus, provided the acceptor shows sufficient solubility, our results demonstrate that the pores of our COF network are well accessible even in films of >100 nm thickness.
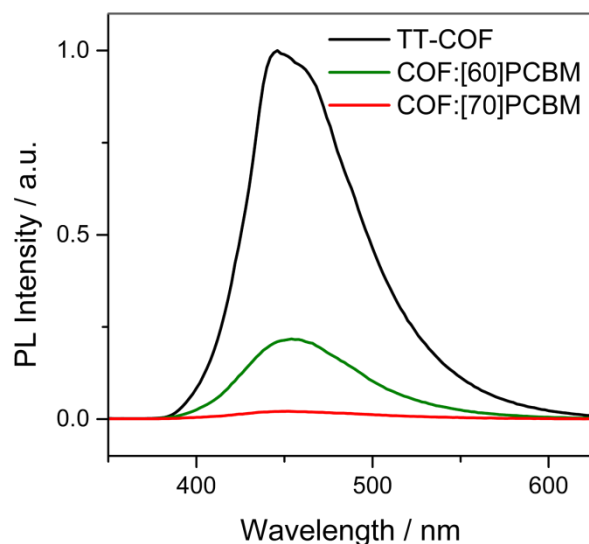
Figure 6.4   PL quenching of a 150 nm thick TT-COF film upon infiltration with PCBM. Excitation was at 325 nm. The spectra were normalized to the PL intensity of the respective film before infiltration.

6.2.3   *Photovoltaic devices*

The first COF-based photovoltaic devices have recently been demonstrated for an ITO/TT-COF:[60]PCBM/Al structure.[5] Here we refine the previous device layout by inserting a 10 nm MoO_x exciton- and electron-blocking layer and a 1 nm LiF layer underneath the Al back electrode. These layers have proven to be crucial for optimal contact in organic solar cells.[6-7] A SEM cross-sectional image of the device structure used in this study is presented in Figure 6.5.

LiF, Al (80 nm)

TT-COF:PCBM (130 nm)
MoO$_x$ (10 nm)
ITO

100 nm
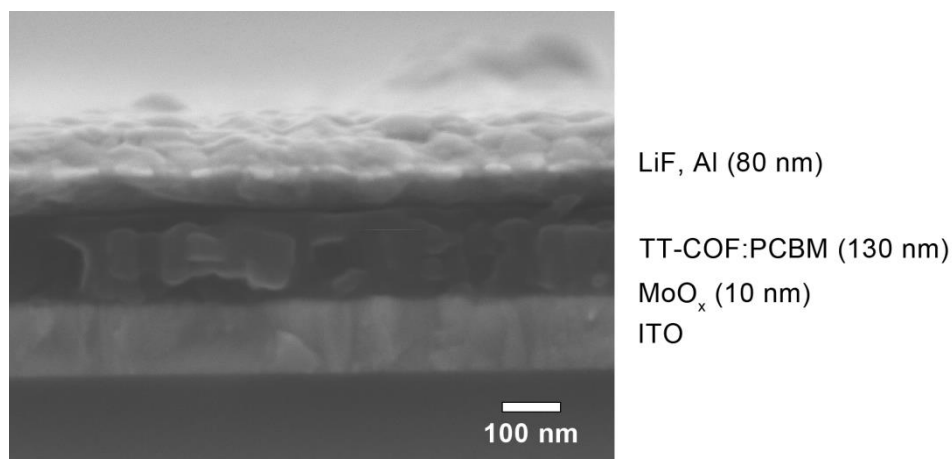
Figure 6.5   Cross-sectional SEM image of a complete COF-based device.

In order to analyse the charge carrier generation and transport capabilities of the TT-COF in combination with PCBM, we recorded external quantum efficiency spectra of our devices (Figure 6.6). We note that most of the photocurrent is generated in the visible region by the PCBM, despite its very low absorbance. The characteristic absorption feature of [60]PCBM is clearly visible in the EQE spectrum at 720 nm. Although the COF absorbs strongly at wavelengths below 400 nm, the EQE drops significantly towards higher energy. This is in part due to the absorption losses in the ITO and MoO$_x$ layers, which reduce the light that is available to the active layer. However, this cannot be the only reason for the low quantum efficiency at these wavelengths. Taking into account the partial PL quenching when using [60]PCBM, it seems likely that the infiltration into a considerable fraction of the COF film is not good enough to form a continuous pathway for electrons. Any interruption of the PCBM phase inside a COF pore would lead to the accumulation of charges, which cannot be transported to the back electrode and thus render a part close to the front electrode electronically inactive. However, this part will absorb the highest percentage of incident photons and therefore work as a light filter for the rest of the device, resulting in reduced EQE in the spectral region where the COF absorbs strongly.

Although the PL quenching is much more efficient when using [70]PCBM (Figure 6.4), devices prepared using this acceptor did not exhibit higher EQEs until now.
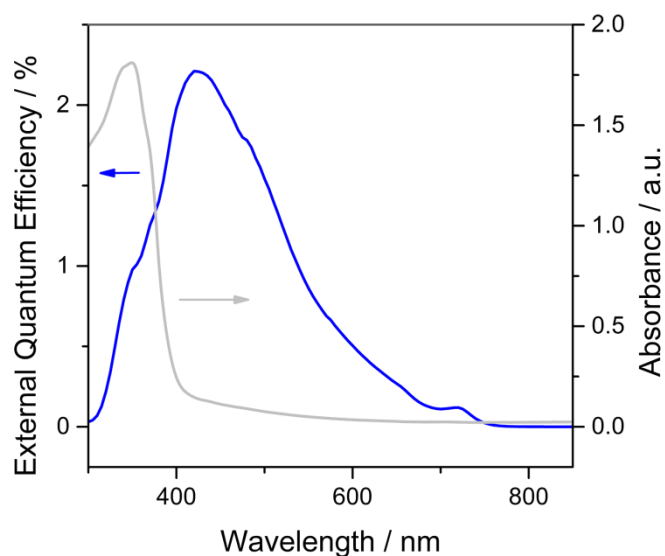
Figure 6.6 EQE spectrum of a ITO/MoOx/TT-COF:[60]PCBM/LiF/Al device (blue) and absorbance of a TT-COF film infiltrated with [60]PCBM (grey).

The *J-V* characteristics under simulated AM1.5G solar illumination are similar to the ones that were previously reported (Figure 6.7). Incorporation of the MoO_x and LiF layer into the device resulted in slightly enhanced average open-circuit voltage (V_{OC}) of about 620 mV. Due to generally lower fill factors – most probably as a result of incomplete infiltration – and low photocurrent the device performance is limited to a conversion efficiency (*PCE*) of 0.03% for the best device and 0.02% on average.
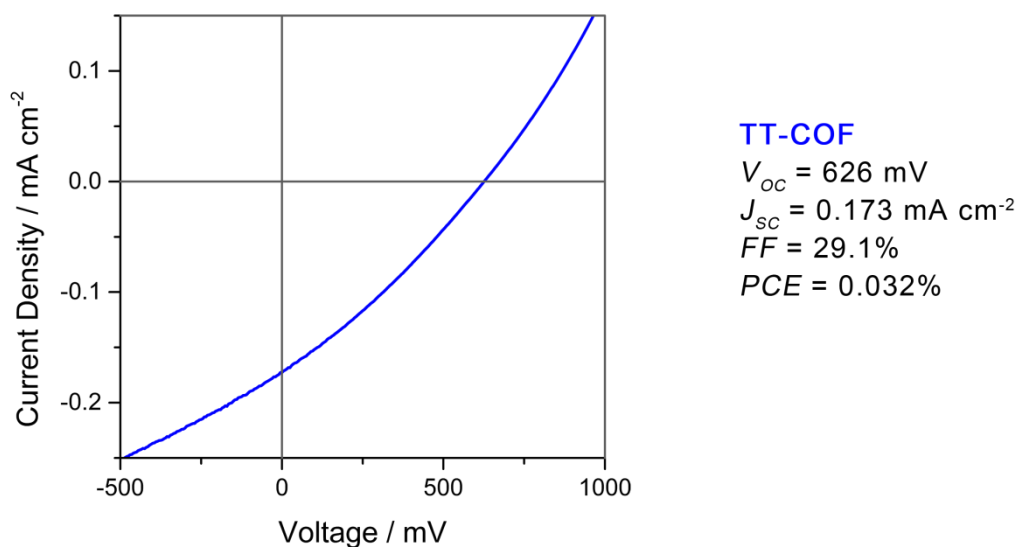
Figure 6.7 *J-V* characteristics of a ITO/MoO$_x$/TT-COF:[60]PCBM/LiF/Al device.

6.2.4 The potential of other fullerene acceptors

Since the optical band gap of the TT-COF is above 3 eV, but the V_{OC} of our PCBM-containing devices only about 600-800 mV (depending on the device thickness), a large fraction of the energy of absorbed photons is lost. Some materials for organic photovoltaics, such as poly(3-hexylthiophene) feature a large energy offset between the lowest unoccupied molecular orbital (LUMO) of the donor and the LUMO of the acceptor. Enhancements in power conversion efficiency have been realized in such devices by replacing the PCBM with a fullerene acceptor, such as ICBA, which possesses a 200 mV higher LUMO level.[3, 8] To test whether higher V_{OC} could be obtained from our TT-COF devices without sacrificing too much of the driving force for charge injection we prepared devices of the same structure as above, but replaced the PCBM with indene-C$_{60}$ bisadduct (ICBA) or indene-C$_{60}$ trisadduct (ICTA). The *J-V* curves of the devices comprising these acceptors are shown in Figure 6.8. As expected, the open-circuit voltage increases from 863 mV for PCBM to 936 and 1207 mV. This impressive improvement, however, is accompanied with a severe reduction in short-circuit current (J_{SC}) from 0.075 to 0.0043 mA cm^{-2}, such that the overall power conversion efficiency remains the best for PCBM. The EQE spectra (Figure 6.9) of the PCBM and ICBA devices

feature a clearly identifiable contribution of the fullerene derivative, whereas the ICTA device, despite similar absorption properties of the acceptors, exhibits only a measurable photoresponse at wavelengths below 450 nm. Despite different LUMO energies these fullerene-based acceptors have very similar HOMO-LUMO gaps. Consequently, as the LUMO energy is shifted upwards for the indene multi-adducts, the HOMO energy is shifted as well. In the case of ICTA the energy offset between the COF and fullerene HOMO might not be enough to drive efficient hole transfer from the fullerene to the COF and consequently excitons created in the fullerene will not contribute to the photocurrent. Electron injection from the COF, however, might still be possible, albeit at a reduced efficiency (see schematic representation of the junction in Figure 6.9).
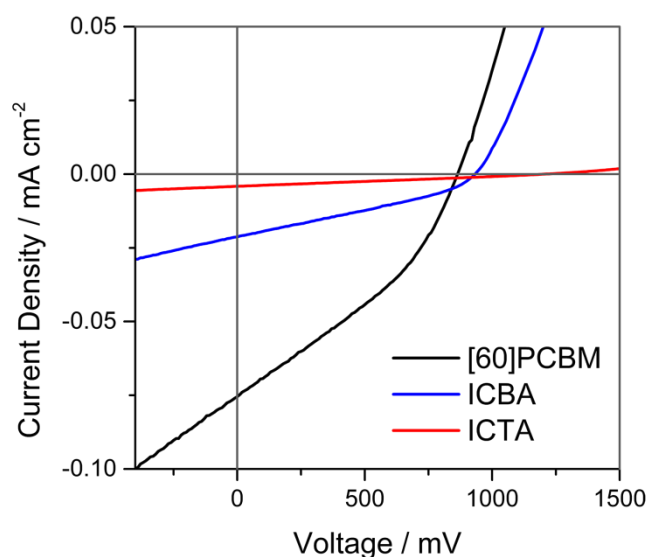
Figure 6.8 *J-V* curves recorded for TT-COF devices based on different fullerene derivatives. Device structure: ITO/MoO$_x$/TT-COF:acceptor/LiF/Al.
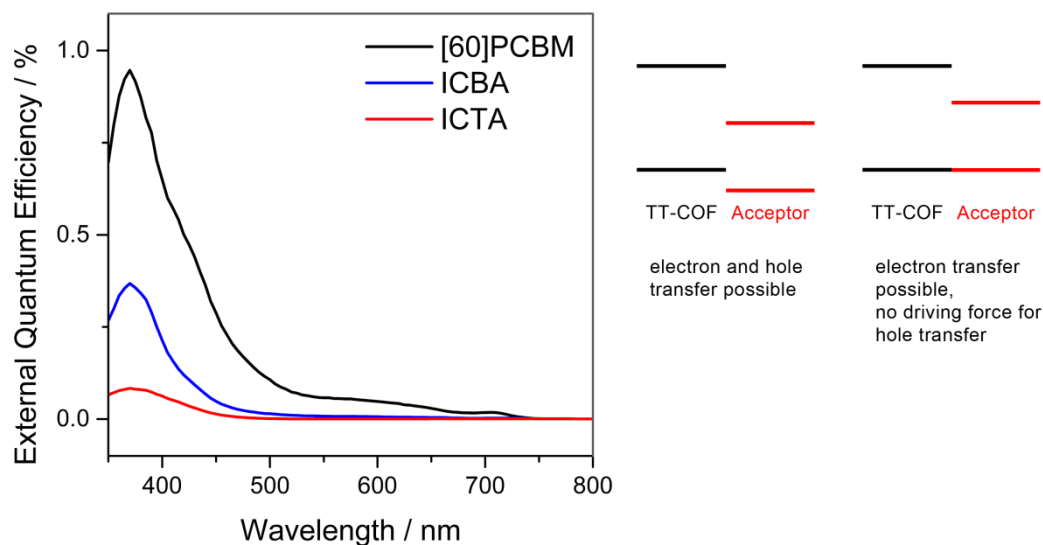
Figure 6.9 EQE spectra of the devices comprising different fullerene derivatives and proposed energy schemes for cases in which hole and electron transfer are favoured (left), and electron transfer only (right).

6.3 Conclusion

Covalent organic frameworks combine tuneable optoelectronic properties with a high degree of molecular order and well-defined and tuneable porosity. We demonstrated the formation of a bi-continuous donor-acceptor network upon infiltration of a thienothiophene-containing COF with a series of fullerene-based electron acceptors. Photo-induced charge transfer was found to cause effective quenching of the COF PL and we were thus able to prove the formation of a heterojunction throughout the entire COF film. First experiments with acceptors that feature a higher LUMO than the PCBM usually used in organic bulk heterojunction solar cells lead to a drastic improvement in open-circuit voltage with a maximum of 1.2 V obtained for the indene-C_{60} trisadduct. Further improvements in voltage, photocurrent, and photovoltaic efficiency are expected from new molecular building blocks that might offer enhanced charge carrier generation and transport properties.

6.4 Experimental

6.4.1 Materials

All materials (if not otherwise noted) were purchased from Aldrich or Fluka in the common purities purum and puriss. 2,3,6,7,10,11-hexahydroxytriphenylene (HHTP) was purchased from TCI Europe. [6,6]-Phenyl C61 butyric acid methyl ester (PCBM) was purchased from Solenne BV. All materials were used without further purification. The building block 2,5-bis(4,4,5,5-tetramethyl-1,3,2-dioxaborolan-2-yl)thieno[3,2-b]thiophene (TTBA) was prepared by Veronika Werner in the group of Prof Knochel.

6.4.2 Preparation of COF thin films

Photovoltaic devices were prepared on indium tin oxide (ITO)-covered glass substrates (VisionTec, 12-15 ohms/sq). After sonication in detergent solution (Hellmanex III, Hellma Analytics), water and ethanol the substrates were treated in an oxygen plasma for 5 min. A 10 nm layer of MoO_x was thermally evaporated at 2×10^{-6} mbar at a rate of 0.5 Å s^{-1}. The TT-COF thin film synthesis was carried out following the published procedure of the bulk synthesis of TT-COF.[5] A conventional stainless steel autoclave equipped with a 10 mL Teflon liner was charged with TTBA (11.6 mg, 0.051 mmol) and HHTP (11.0 mg, 0.034 mmol). The reaction mixture was suspended in 4 ml of a 1:1 v:v solution of mesitylene:dioxane and heated for 72 h at 150 °C. Two MoO_x covered ITO substrates were inserted into the synthesis solution and recovered after 72 h. The films were washed thoroughly with dioxane and dried under nitrogen. Typical film thicknesses are in the range of 250-300 nm, however, depending on the batch of the starting material and the amount of precipitate formed in the synthesis solution, some films are only around 130 nm thick. However, no clear correlation between COF film thickness and device performance was observed.

6.4.3 Device fabrication

TT-COF films were activated at 150 °C for 2 h in high vacuum and immediately transferred to an argon filled glove box. Infiltration with the fullerene derivatives was achieved by spin-coating a 25 mg mL^{-1} solution of the respective acceptor molecule in

chlorobenzene. Photovoltaic devices were completed by thermal evaporation of 1 nm LiF and 80 nm Al at rates of 0.2 and 2.0 Å s^{-1}, respectively, yielding an active area of 3.0×3.0 mm^2 and 4 individual devices per substrate (Figure 6.10).
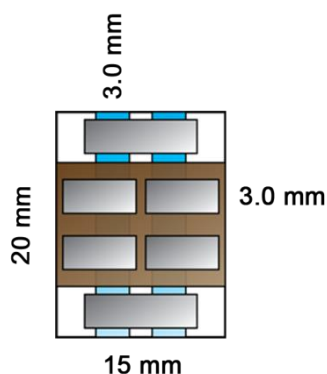
Figure 6.10 Device layout used for the COF solar cells. 4 individual devices are defined via the overlap of the ITO and the Al electrodes.

6.4.4   Characterisation

X-ray diffraction experiments were carried out using a Bruker D8 Discover with Ni-filtered CuK$_\alpha$-radiation (0.154 nm) and a position-sensitive detector (LynxEye). SEM micrographs were recorded on a JEOL JSM-6500F scanning electron microscope operated at 5 kV and using secondary electrons as signal for imaging. UV-Vis spectra were measured with a Perkin-Elmer Lambda 1050 UV-Vis/NIR spectrometer equipped with a 150 mm integrating sphere. COF thin films were measured in transmission geometry and the spectra were corrected for reflectance losses. Photoluminescence measurements were carried out using a Photon Technology International QuantaMaster 40. COF thin films were also synthesized on quartz glass serving as electronically inactive, non-fluorescent substrates.

J-V-curves of COF photovoltaic devices were recorded with a Keithley 2400 sourcemeter under illumination with simulated solar radiation obtained from an AM1.5G solar simulator (Solar Light Model 16S) at 100 mW cm^{-2}. Lower light intensities were realised by a set of neutral density filters. All light intensities were calibrated with a Fraunhofer

ISE certified silicon reference cell equipped with a KG5 filter for reduced spectral mismatch. External quantum efficiency (EQE) measurements were performed at short circuit. Monochromatic light was obtained from a 150 W xenon lamp in combination with a monochromator and order-sorting filters. The monochromatic light was modulated using an optical chopper at a frequency of 27 Hz. The modulation frequency was chosen slow enough such that the response of the sample was frequency-independent. The signal was detected via a low noise pre-amplifier (Femto DLPCA-200) and a lock-in amplifier (Signal Recovery 7230). During the measurement the light intensity was continuously monitored via a silicon photodiode connected to a second lock-in amplifier. The EQE measurement was referenced to the response of a silicon photodiode with NIST-traceable calibration.

6.5   References

[1]   A. K. K. Kyaw, D. H. Wang, V. Gupta, J. Zhang, S. Chand, G. C. Bazan, A. J. Heeger, *Adv. Mater.* **2013**, *25*, 2397-2402.

[2]   Y. Liang, Z. Xu, J. Xia, S.-T. Tsai, Y. Wu, G. Li, C. Ray, L. Yu, *Adv. Mater.* **2010**, *22*, E135-E138.

[3]   E. T. Hoke, K. Vandewal, J. A. Bartelt, W. R. Mateker, J. D. Douglas, R. Noriega, K. R. Graham, J. M. J. Fréchet, A. Salleo, M. D. McGehee, *Adv. Energy Mater.* **2013**, *3*, 220-230.

[4]   T. Kirchartz, T. Agostinelli, M. Campoy-Quiles, W. Gong, J. Nelson, *J. Phys. Chem. Lett.* **2012**, *3*, 3470-3475.

[5]   M. Dogru, M. Handloser, F. Auras, T. Kunz, D. Medina, A. Hartschuh, P. Knochel, T. Bein, *Angew. Chem. Int. Ed.* **2013**, *52*, 2920-2924.

[6]   V. Shrotriya, G. Li, Y. Yao, C.-W. Chu, Y. Yang, *Appl. Phys. Lett.* **2006**, *88*, 073508.

[7]   R. Steim, F. R. Kogler, C. J. Brabec, *J. Mater. Chem.* **2010**, *20*, 2499-2512.

[8]   M. A. Faist, T. Kirchartz, W. Gong, R. S. Ashraf, I. McCulloch, J. C. de Mello, N. J. Ekins-Daukes, D. D. C. Bradley, J. Nelson, *J. Am. Chem. Soc.* **2012**, *134*, 685-692.

7 Photo-Induced Charge Transfer in Phthalocyanine-Containing Covalent Organic Frameworks

The following studies have been performed in a joint project: Thin films of the covalent organic frameworks were grown and analysed by Mona Calik, the molecular building blocks were synthesized by John Colson in the group of Prof Dichtel at Cornell University. Optoelectronic characterisation and device fabrication and characterisation were performed by Florian Auras, Mona Calik and John Colson.

7.1 Introduction

Organic polymer- and small molecule-based solar cells have reached impressive power conversion efficiencies of above 10% during the past years.[1] While much of the progress is initiated by the development of new donor materials that exhibit improved light harvesting capabilities[2-3] and the implementation of multijunction device architectures,[4] precise control of the morphology in photoactive blends remains a major challenge. The performance of bulk heterojunction cells has been demonstrated to depend critically on microstructure formation during the deposition of the active layer.[5] It would therefore be highly desirable to create structurally well-defined interpenetrating donor and acceptor networks that could serve as model systems for basic research. Moreover, this could present a strategy for incorporating building blocks that would have suitable optoelectronic properties, but cannot develop their full potential in bulk heterojunction devices due to unfavourable film morphology. We have recently reported a photovoltaic device based on a photoactive covalent organic framework (COF) that was infiltrated with a soluble electron acceptor.[6] COFs are a recently discovered class of materials comprising molecular building blocks that form three-dimensional crystalline and porous networks.[7-8] Specifically, the π-stacked layers of 'two-dimensional' COFs are anticipated to permit charge migration through the framework, and several semiconducting structures have been described.[9-11] Here we report photo-induced charge transfer from different zinc phthalocyanine (ZnPc) COFs to an electron acceptor located inside the COF pores. We prepared COFs with pore sizes of 2.7 and 3.4 nm using pyrene- and diphenyl butadiyne-based linear linkers to connect the

107

tetragonal ZnPc units.[12] We studied the formation of a bi-continuous donor-acceptor network upon infiltration of the COFs with [6,6]-phenyl C_{n+1} butyric acid methyl ester (n = 60, 70; [n]PCBM) and created photovoltaic devices based on this combination of materials. Comparison of their optoelectronic properties and device performance to model systems that feature the same linear linkers[13-14] but a trigonal hexaol building block (2,3,6,7,10,11-hexahydroxytriphenylene, HHTP) that is not photoactive throughout the visible spectrum illustrates a profound effect of the ZnPc unit on the charge separation and transport capabilities.

7.2 Results and Discussion

7.2.1 Synthesis of COF films

To incorporate the unique structure of covalent organic frameworks into a photovoltaic device, thin films of the different COF systems were grown on conductive substrates. Instead of using single-layer graphene as nucleation surface as reported earlier by Spitler *et al.*,[12-13] a nickel oxide layer was used. This 5 nm thick layer not only provides a nucleation surface but also acts as hole-selective layer. Crystalline and oriented COF films were obtained by a condensation reaction of the starting materials under solvothermal conditions in the presence of NiO/ITO substrates.

Covalent organic frameworks provide access to a variety of different pore sizes and pore geometries by changing the molecular building blocks. In this work we investigated the differences between two tetragonal COFs based on a square-shaped zinc octahydroxyphthalocyanine (ZnPc(OH)$_8$) and two hexagonal frameworks with a trigonal hexahydroxy triphenylene (HHTP) linker (Figure 7.1). These units are joined through condensation of the polyol with pyrene diboronic acid (PyBA) or diphenyl butadiynediboronic acid (DPBA). Fragments of the two-dimensional periodic COF structures are shown in Figure 7.2. Incorporation of ZnPc leads to the formation of a square lattice with quadratic pores, whereas HHTP-containing COFs feature a hexagonal arrangement and consequently larger pore diameters. The pore size can be further adjusted through the selection of the linear linker.
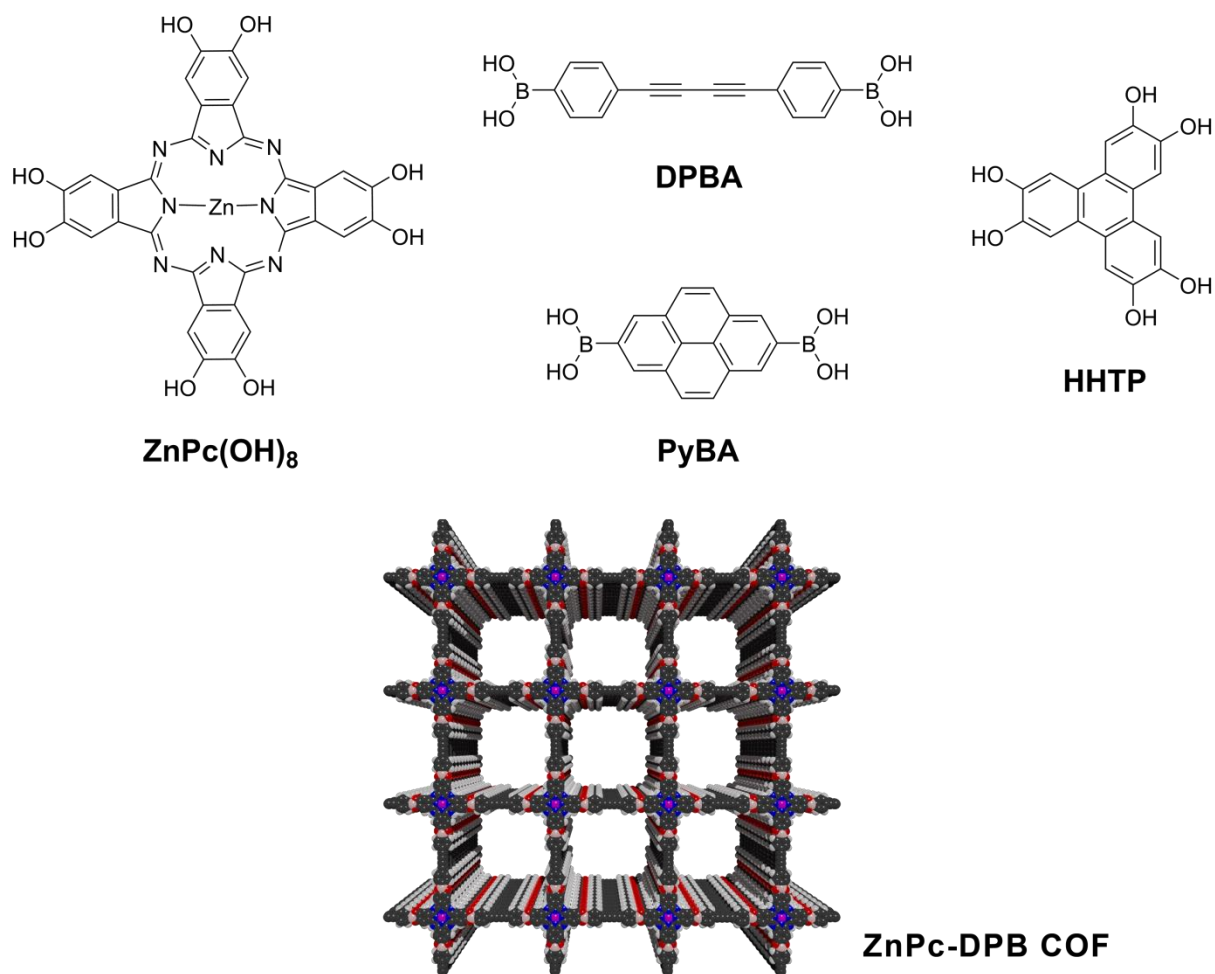
Figure 7.1 Chemical structure of the catechols and diboronic acids used in this study and an idealized model of the ZnPc-DPB COF.
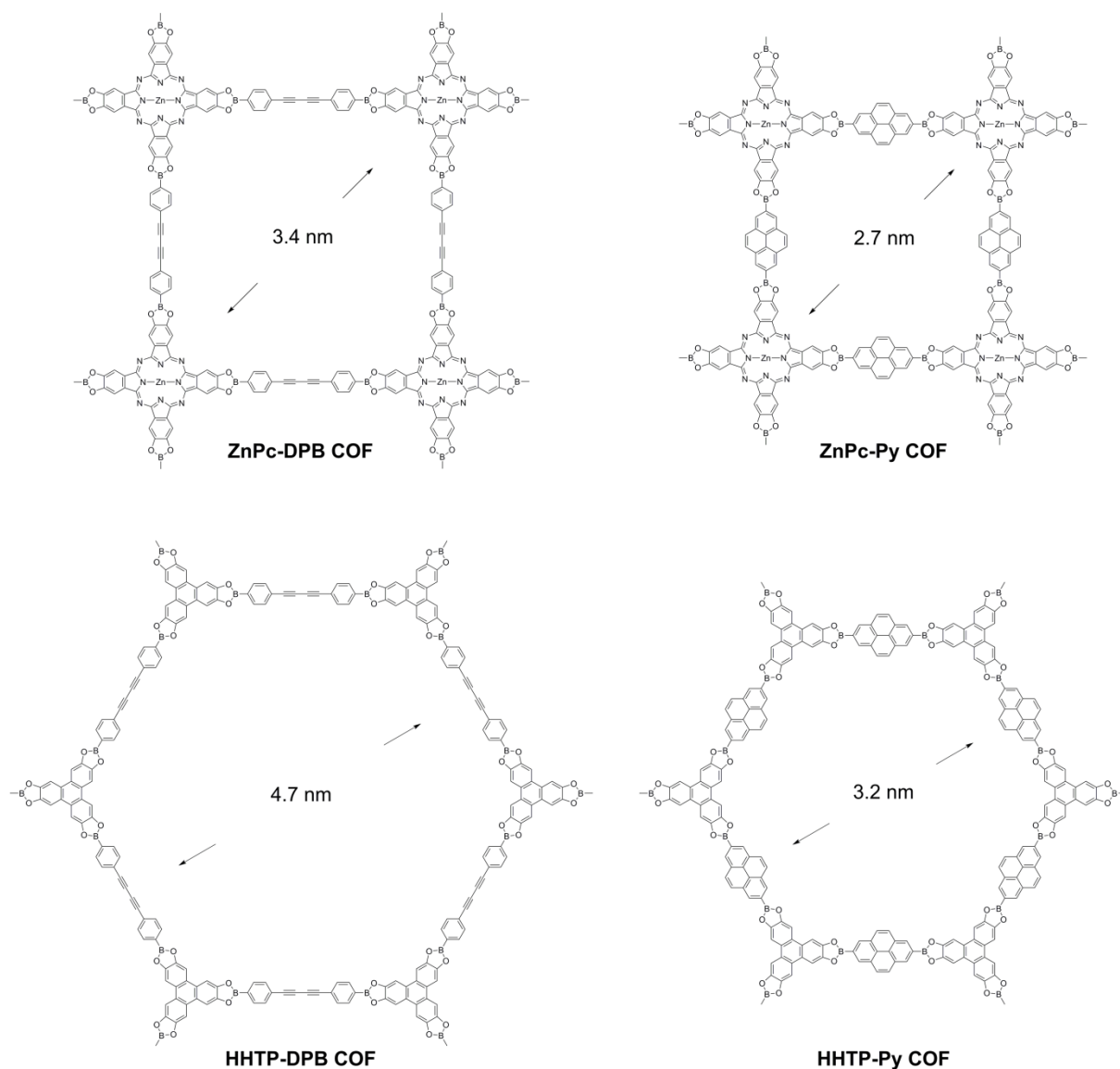
Figure 7.2 Chemical structures of the COFs used in this study. Each COF forms a two-dimensional periodic network of ZnPc (top row) or HHTP (bottom) joined by DPB (left) or pyrene units (right).

7.2.2 Optical properties and photo-induced charge transfer

The ZnPc-containing COFs possess a deep green colour. The UV-Vis spectrum of the ZnPc-Py COF thin film shows the characteristic Q-band signals at 715 and 751 nm (Figure 7.3, green line). In the ZnPc(OH)$_8$ precursor the Q-bands appear as broad signals at lower energy (730 and 801 nm), while they are much sharper and shifted to 717 and

750 nm, respectively, in the COF film (Supporting Information, Figure 7.11). The maximum of the ZnPc-Soret band is blue-shifted in the COF as well, from 275 to 262 nm. These observations indicate a change in the packing behaviour of the phthalocyanine upon COF formation. As the signals of the pyrene at 330 and 346 nm remain at their spectral position upon incorporation of the linker into the COF framework, the electronic interactions between the pyrene units seem to be less affected by the COF formation.
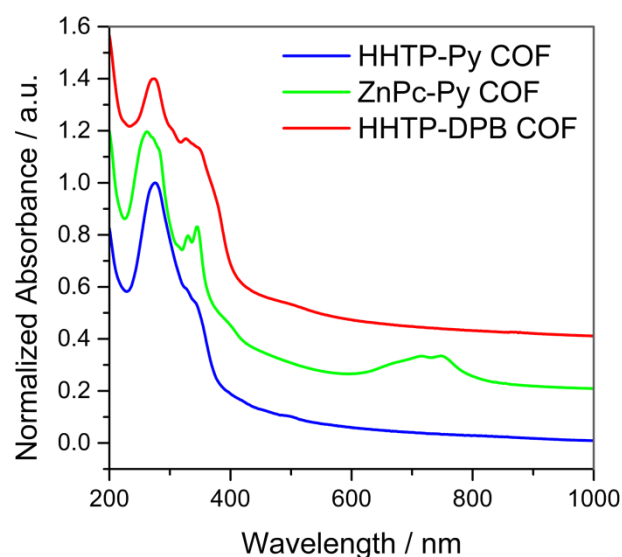
Figure 7.3   Absorbance of the COF films. The curves were normalized to the peak at 260-290 nm and an offset was added for clarity.

When combining the pyrene and diphenyl butadiyne (DPB) with HHTP instead, the COFs are transparent in the visible region, but absorb strongly in the UV (Figure 7.3; Supporting Information, Figure 7.12 and Figure 7.13). The spectral features of the linear linkers are clearly visible and remain unchanged after COF formation. The main absorption band of the HHTP is red-shifted by 5 nm upon incorporation into the COF framework.

Both the DPB and the pyrene linker show considerable photoluminescence (PL) with emission maxima at 439 and 436 nm, respectively, when immobilised in the COF framework.[13-14] If charge transfer to an acceptor molecule within the exciton diffusion

length is feasible, this PL will be quenched.[6] We prepared COF films on quartz glass (serving as a non-fluorescent, non-quenching substrate) and infiltrated them with a solution of PCBM. We observed that for the HHTP-DPB COF the initial PL is reduced by more than 80%, indicating that enough PCBM molecules were able to get into close enough contact with the DPB units to trigger charge transfer before the exciton on the DPB would recombine radiatively (Figure 7.4). A control experiment in which only the solvent without PCBM was used for infiltration resulted in reduction of the PL intensity by less than 1%. We observe a similar behaviour for the HHTP-Py COF, however, in this case the PL is quenched by only 55% (Supporting Information, Figure 7.14). Taking into account the smaller pore size of only 3.2 nm compared to 4.7 nm of the HHTP-DPB COF, it seems likely that the infiltration into the HHTP-Py COF is not as complete as in the case of the HHTP-DPB COF. Furthermore, misaligned domains might not be accessible to the PCBM solution and therefore still show PL.

When combining the linear linkers with the ZnPc, however, we do not observe any PL. Fast energy transfer has been reported for porphyrin-based COFs.[15] Since the PL emission of the DPB and pyrene linkers has significant overlap with the absorption of the phthalocyanine, the excited linker might undergo Förster resonance energy transfer (FRET) to the ZnPc. Due to the formation of H-aggregates the excited ZnPc, however, will not decay to its ground state radiatively. Judging from the complete absence of any measurable PL, the energy transfer seems to be a very fast and effective process.
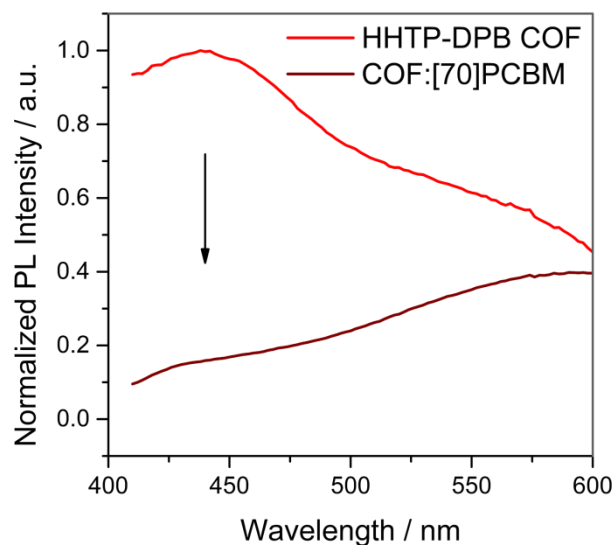
Figure 7.4 Photoluminescence spectra of the HHTP-DPB-COF before (red) and after (brown) impregnation with PC$_{71}$BM, with excitation at 365 nm. The PL intensity is reduced by approximately 85%.

7.2.3   Photovoltaic devices

Photovoltaic devices based on an interpenetrated COF:PCBM heterojunction were first demonstrated for hexagonal thienothiophene-containing COFs.[6] In order to study the charge generation and transport capabilities of the much stronger absorbing ZnPc COFs, we assembled devices with an ITO/NiO/COF:PCBM/LiF/Al structure. NiO has found application as a hole-selective layer in bulk heterojunction solar cells, whereas the low work function LiF/Al back electrode is widely used in organic photovoltaics as electron-selective contact.[16-17]
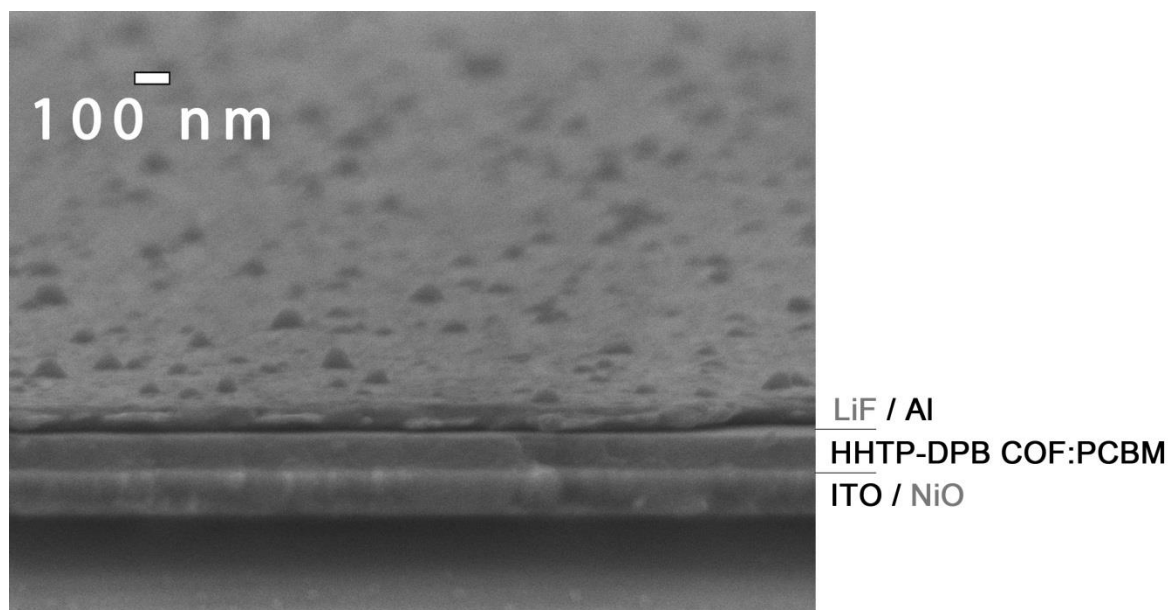
Figure 7.5 Tilted SEM cross section of a complete HHTP-DPB COF device. Device structure: ITO (130 nm) / NiO (5 nm, not resolved in SEM image) / HHTP-DPB COF:[60]PCBM (100 nm) / LiF (1 nm, not resolved) / Al (80 nm). The layers that are denoted in grey are too thin to be resolved in the SEM image.

As already demonstrated by the PL quenching experiments above, infiltration of a pre-formed COF film with PCBM can be achieved via spin-coating a solution of the fullerene derivative. This procedure also creates a PCBM overlayer of about 20 nm thickness, which additionally increases the electron-selectivity of the back contact.

The external quantum efficiency (EQE) spectra of the ZnPc-DPB COF and HHTP-DPB COF devices (Figure 7.6) peak at around 400 nm, where all potentially photoactive components absorb strongly. At longer wavelengths both spectra exhibit a series of features with the most characteristic one being at 720 nm, which can be attributed to the photoresponse of [60]PCBM. The photoresponse of the ZnPc unit, however, is unexpectedly weak. Only the broad signal above 750 nm can be attributed to a contribution of this unit. Taking into account the strong absorption of the phthalocyanine in this wavelength range, electron transfer from the photoexcited Pc seems to be hindered. At around 400 nm the Pc even seems to work as a light filter, which lowers the photoresponse of the DPB and PCBM, such that we observe an inverse peak (dip) in the spectrum. Efficient charge transfer at an organic heterojunction is

known to require an energy offset of typically around 300 meV.[18-19] At this point we do not know the energy levels of the ZnPc when incorporated into the ZnPc-DPB COF framewok, thus it is possible that an insufficient energy offset between the LUMO of the ZnPc and PCBM might cause the very low efficiency of this process. On the other hand, the tetragonal Pc unit is located at the corners of the COF pores. We note that close contact between the ZnPc moiety and PCBM molecules inside the quadratic COF pores might be sterically hindered by the pore geometry and the observed low efficiency for charge transfer might be due to the larger distance between donor and acceptor (compared to the contact with a linear linker). When comparing the EQE spectra of the HHTP-DPB and the ZnPc-DPB COF, however, we note that we obtain reproducibly higher overall EQEs for the ZnPc-DPB COF-based cells. Especially at wavelengths longer than 450 nm, at which the ZnPc is not strongly absorbing, considerably more current is collected from the ZnPc-DPB COF devices.

(a)   **(b)**
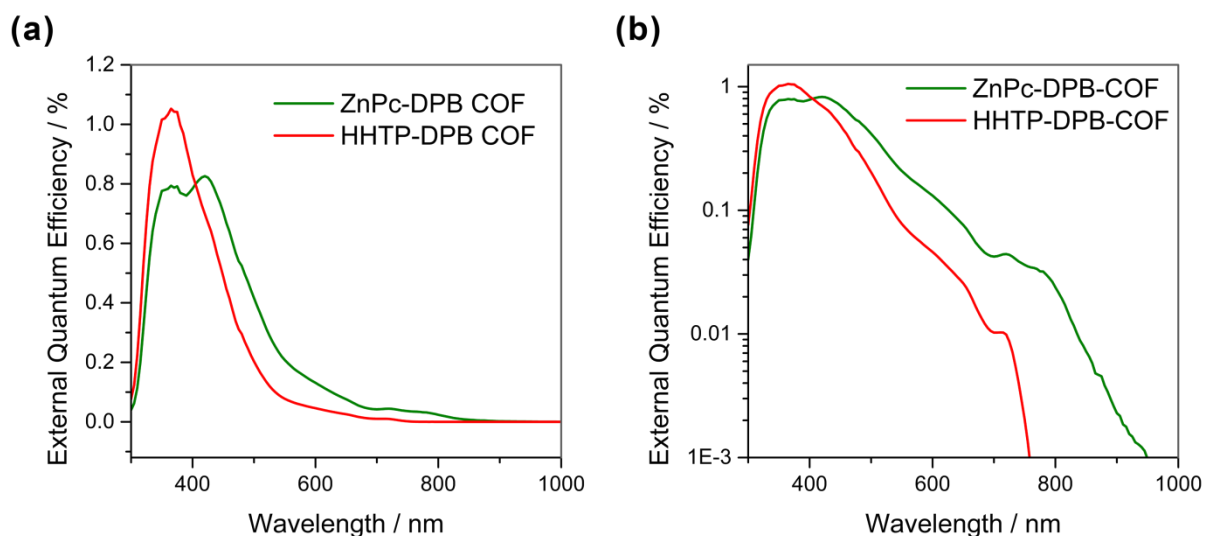
Figure 7.6 EQE spectra of the ZnPc-DPB (green) and HHTP-DPB COF devices (red) on a linear (a) and a semi-logarithmic scale (b).

We ask whether the ZnPc unit, despite hardly contributing directly to the charge carrier generation, may have an influence on the charge transport, which could render these devices more efficient than their HHTP-DPB counterparts. *J-V* curves were recorded for both types of devices under simulated AM1.5G solar illumination (Figure 7.7). The HHTP-containing device exhibited, despite larger pore size and consequently easier

infiltration with the fullerene phase, a significantly lower current and higher series resistance than the ZnPc device. Since the DPB molecule is extremely thin and does not provide large overlapping π-systems, this linker is expected to be poorly conducting and susceptible to non-geminate recombination losses. Although the two building blocks of our COFs seem to be electronically separated by the boronic acid ester linkage, the ZnPc-COF with the same linear linker exhibits higher photocurrents at the cost of a reduced open-circuit voltage.

ZnPc-DPB COF
V_{OC} = 362 mV
J_{SC} = 0.024 mA cm^{-2}
FF = 28%
PCE = 0.0024%

HHTP-DPB COF
V_{OC} = 611 mV
J_{SC} = 0.016 mA cm^{-2}
FF = 23%
PCE = 0.0023%
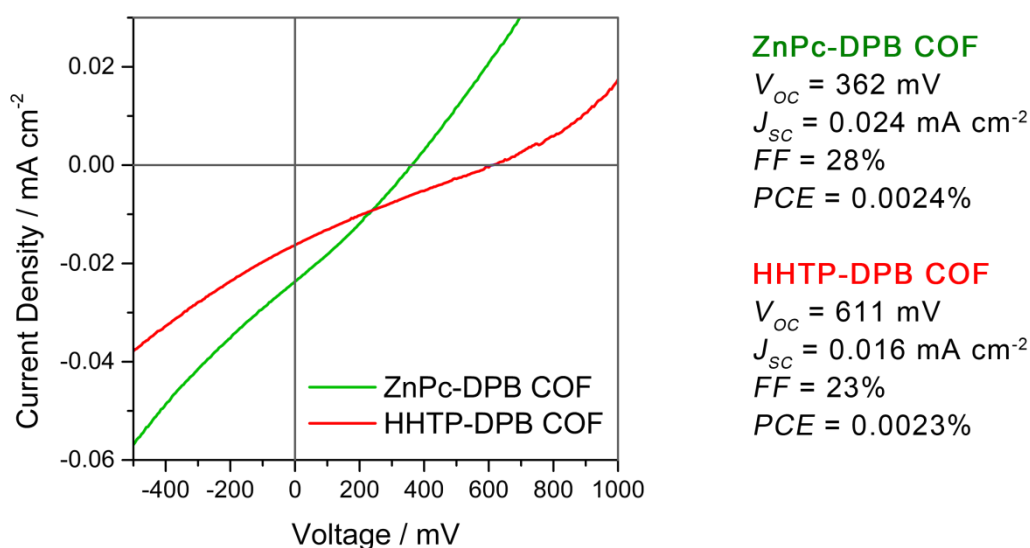
Figure 7.7 *J-V* characteristics of the ZnPc-DPB (green) and HHTP-DPB COF devices (red) with [60]PCBM as electron acceptor.

We performed control experiments with COFs containing a pyrene diboronic acid as linear linker and the same trigonal or tetragonal building blocks, respectively (see Supporting Information, Figure 7.15). The HHTP-Py COF exhibited an open-circuit voltage of 677 mV, which was reduced to around 400 mV when exchanging the HHTP for the ZnPc unit, very similar to the above case of the ZnPc-DPB COF. Since the pyrene building block provides a considerably larger π-electron system than the DPB, the stacked pyrene units are expected to offer reasonably efficient charge carrier transport even without the phthalocyanine. Moreover, the pores of the ZnPc-Py COF are only 2.7 nm, which might be too small for effective infiltration with PCBM. The 3.2 nm hexagonal pores of the HHTP-Py COF, however, are comparable to thienothiophene

COFs, for which successful infiltration has been demonstrated.[6, 20] From the above considerations we expect the short-circuit current of the HHTP-Py COF devices to be similar or higher than the current obtained from the ZnPc-Py COF. We measured indeed a higher photocurrent for HHTP-Py than for the ZnPc-Py COF-based devices.

The open circuit voltage depends on the difference in quasi-Fermi levels of holes in the donor phase and electrons in the acceptor phase. If the hole is collected from the linear linker and the building block in the corners is not involved in the charge generation or transport (as in the case for HHTP due to a large HOMO-LUMO gap and a packing scheme that renders it essentially non-conductive)[21] we expect V_{OC} to depend on the choice of the linear linker. Due to their deep-lying HOMO levels both the DPB and the pyrene linker generate open-circuit voltages of around 700 mV when linked to HHTP. However, when introducing the ZnPc this voltage is reduced to approximately 400 mV and the collection efficiency is enhanced in the DPB case, indicating the existence of a different path for charge collection. The enhanced collection efficiency can be due to either improved carrier mobility or a longer charge carrier lifetime. Taking into account the analysis of the EQE spectra, which indicated that the electron injection from the Pc unit into the fullerene phase located inside the COF pores is ineffective, we can assume that also the back-transfer of an electron on a PCBM molecule to the phthalocyanine stacks occurs at a low rate and therefore recombination losses are reduced. We thus propose the following model for the charge carrier generation and transport in our ZnPc-containing COFs: If light is absorbed by the PCBM the hole is initially transferred to the DPB molecule, from where it can be transferred, most likely via tunnelling, to the ZnPc stacks. Since recombination from the phthalocyanines is suppressed these holes will be collected with high probability, leading to an enhancement in J$_{SC}$. Due to the energy offset between the DPB and Py HOMO and the ZnPc HOMO, V_{OC} is reduced at the same time by about 300 mV (Figure 7.8). Achieving spatial separation of charge carriers through an energy cascade is a motif known from natural photosynthesis, where initially the photosystem is excited, followed by an electron transfer chain. Future experiments will be dedicated to clarifying the mechanism of charge transfer and optimizing this scheme for maximal collection efficiency at low voltage losses.
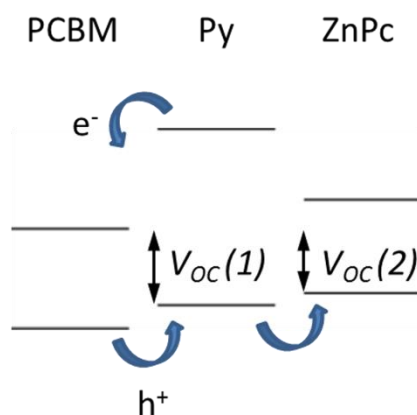
Figure 7.8 Proposed energy scheme for the hole transfer cascade. $V_{OC}(1)$ is the maximum voltage that could be obtained from the HHTP-Py COF:PCBM heterojunction. $V_{OC}(2)$ is the reduced voltage after the cascade to the ZnPc unit of the ZnPc-Py COF.

Many highly efficient organic semiconductors absorb strongly in the red to infrared spectral region, while they feature relatively weak absorbance for blue and green light. To extend the light harvesting capabilities of these materials, the [60]PCBM is frequently replaced by the much stronger absorbing [70]PCBM. The use of this acceptor in our COF devices would not only greatly extend the absorption into the visible spectral region, but could also lead to improved infiltration due to the much higher solubility of the C_{70} derivative. Indeed, when using [70]PCBM in our devices the short circuit current improved approximately by a factor of 2.5 and the corresponding EQE spectra feature a large signal that extends over the whole visible range (Figure 7.9). The maximum in the EQE spectrum is shifted to longer wavelengths, which can again be attributed to light filtering by the phthalocyanine in the spectral region where it absorbs strongly. The contribution of the ZnPc at long wavelengths seems essentially unaffected by the choice of the acceptor. Considering the very similar electronic properties of [60]PCBM and [70]PCBM, differences would be mostly expected from changes in the degree of infiltration. However, despite the higher solubility of the C_{70} derivative, the formation of the bi-continuous network seems to be similar in both cases.
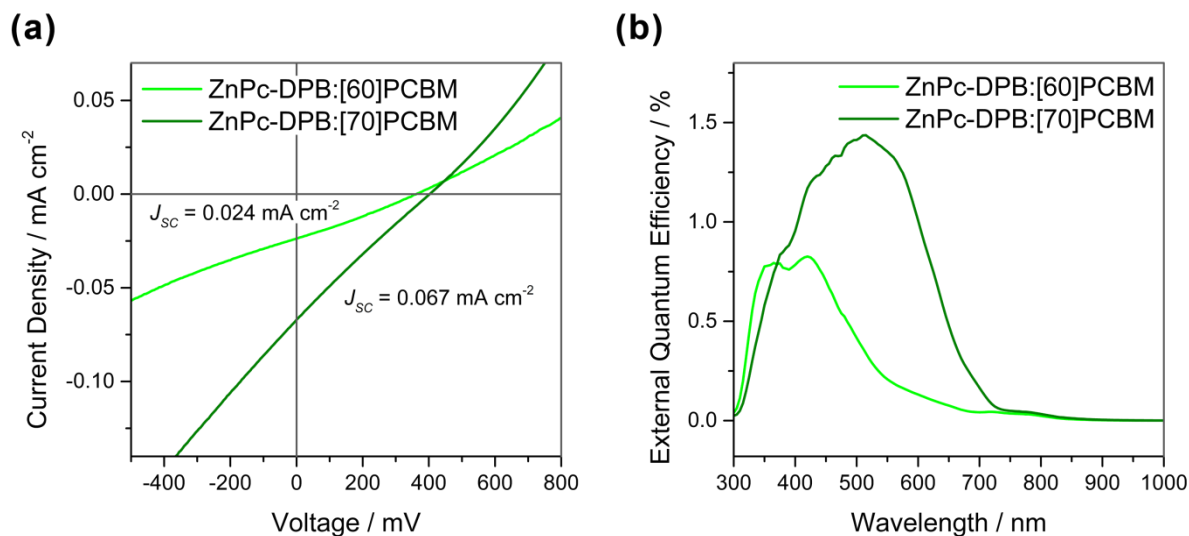
Figure 7.9 Comparison of the *J-V* characteristics (a) and EQE spectra (b) of the ZnPc-DPB COF infiltrated with [60]PCBM and [70]PCBM.

7.3 Conclusion

Molecular packing and microstructure formation on a length scale within the exciton diffusion length is a critical requirement for efficient bulk heterojunction solar cells and can impose a limit on the potential of new materials with promising optoelectronic properties. The creation of porous and crystalline frameworks of organic semiconductors that are subsequently infiltrated with a complementary phase to form a bi-continuous donor-acceptor network of defined dimensions might ultimately overcome these limitations. The covalent organic frameworks described herein show significant photoresponse when infiltrated with a fullerene derivative. The incorporation of a zinc phthalocyanine unit into the COF provides a pathway for achieving more efficient charge collection through a proposed energy cascade-driven spatial separation of the photogenerated charge carriers. The crystalline and hence atomically defined nature of COFs renders them ideal model systems for studying the interplay of rationally designed molecular building blocks for solar energy conversion and to decouple the effect of molecular orientation, packing, and microstructure formation from the optoelectronic properties of novel materials.

7.4 Experimental

7.4.1 Materials and precursors

All solvents were purchased from Sigma-Aldrich, Alfa Aesar or Acros and used as received. NiOAc$_2$×4H$_2$O (99.998%) and ethanolamine (99.5%) were obtained from Sigma-Aldrich. HHTP was purchased from TCI Europe, [60]PCBM (99.5%) and [70]PCBM (99%) were obtained from Solenne BV and used without further purification.

Diphenyl butadiynediboronic acid, zinc octahydroxyphthalocyanine, and pyrene diboronic acid were synthesized by John Colson at Cornell University following published procedures.[13, 22-23]

7.4.2 COF film synthesis

General procedure for ZnPc-DPB COF film growth on NiO. A 100 mL Schott flask was charged with Zn octahydroxyphthalocyanine (20 mg, 0.028 mmol), diphenyl butadiynediboronic acid (17 mg, 0.059 mmol) and 30 mL of a 2:1 v:v mixture of dimethylacetamide:dichlorobenzene. After capping, the flask was sonicated for 1 minute and nine NiO-coated ITO substrates were added with the NiO layer face down (see below for preparation of NiO-coated substrates). The sealed vessel was heated at 120 °C for 16 hours. The resulting dark green powder was isolated by filtration and dried under vacuum. The NiO-coated substrates were submerged in anhydrous toluene, sonicated for 5 seconds and dried under a nitrogen flow.

ZnPc-Pyr COF films were prepared following the above described procedure using Zn octahydroxyphthalocyanine (20 mg, 0.028 mmol), pyrene diboronic acid (17 mg, 0.059 mmol), and a 2:1 mixture of dimethylacetamide and dichlorobenzene (2:1, 30 mL).

HHTP-DPB COF film. Hexahydroxy triphenylene (30 mg, 0.093 mmol) and diphenyl butadiynediboronic acid (34 mg, 0.117 mmol) were added to a 100 mL Schott flask. The reagents were dissolved in a 4:1 v:v 1,4-dioxane:mesitylene mixture (4:1, 30 mL) and sonicated for 1 minute. After the addition of the NiO-coated substrates (preparation see below), the sealed flask was heated at 100 °C for 16 hours. The white precipitate was

collected by filtration and the substrates were submerged in anhydrous toluene, sonicated for 5 seconds and were dried under a nitrogen flow.

HHTP-Pyr COF film. The above-described procedure was followed using hexahydroxy triphenylene (30 mg, 0.093 mmol), pyrene diboronic acid (17 mg, 0.059 mmol), and a 4:1 v:v mixture of 1,4-dioxane and mesitylene (4:1, 30 mL).

7.4.3   Device fabrication

COF-based devices were prepared on ITO-coated glass (VisonTec, 12-15 ohms/sq) slides. After cleaning in detergent solution (Hellmanex III, Hellma Analytics), water, ethanol, and isopropanol the substrates were covered with 50 µL of a NiO precursor solution consisting of 100 mM $NiOAc_2 \times 4H_2O$ (99.998%, Aldrich) and 100 mM ethanolamine (99.5%, Aldrich) in HPLC-grade ethanol via spin-coating at 3000 rpm. Calcination of the dried films at 300 °C for 45 min in air converted the precursor into a ~5 nm thick layer of NiO. COF films were grown on these substrates as described above, washed with dioxane, transferred into an argon-filled glove box and activated by thermal treatment at 125 °C on a hotplate for 1h. [60]PCBM and [70]PCBM were applied via spin-coating 40 µL of a 25 mg mL^{-1} solution in 1,2-dichlorobenzene at 600 rpm., followed by annealing at 80 °C. Devices were completed by thermal evaporation of 1 nm LiF and 80 nm Al, resulting in an active area of 3.0×3.0 mm^2 and four pixels per substrate (Figure 7.10).
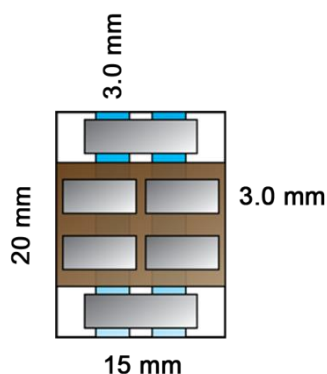
Figure 7.10   Device layout used for the COF solar cells. 4 individual devices are defined via the overlap of the ITO and the Al electrodes.

7.4.4   Characterisation

X-ray diffraction was carried out using a Bruker D8 Discover instrument with Ni-filtered CuK$_{\alpha}$-radiation (0.154 nm) and a position-sensitive detector (LynxEye). SEM micrographs were recorded on a JEOL JSM-6500F scanning electron microscope operated at 5 kV. UV-Vis spectra were measured with a Perkin-Elmer Lambda 1050 UV-Vis/NIR spectrometer equipped with a 150 mm integrating sphere and an InGaAs detector. COF thin films were measured in transmission geometry and the spectra corrected for reflectance losses. Complete devices were measured in reflectance geometry with the sample positioned such that light scattered towards the edges of the substrate was collected by the sphere. Photoluminescence measurements were recorded with a Photon Technology International QuantaMaster 40 or a home-built setup consisting of a Horiba iHR320 spectrometer equipped with a photomultiplier tube and a LN$_2$-cooled InGaAs detector. A 365 nm LED modulated at 83 Hz was used as excitation source and the PL signal was detected via a Signal Recovery 7230 lock-in amplifier. The system was calibrated for spectral response with a calibrated light source. *J-V* curves were recorded with a Keithley 2400 sourcemeter under illumination with simulated solar radiation obtained from an AM1.5G solar simulator (Solar Light Model 16S) at 100 mW cm^{-2}. Lower light intensities were realised by a set of neutral density filters. All light intensities were calibrated with a Fraunhofer ISE certified silicon

reference cell equipped with a KG5 filter. External quantum efficiency (EQE) measurements were performed at short circuit. Monochromatic light was obtained from a 150 W xenon lamp in combination with a monochromator and order-sorting filters. The slits were adjusted such that the FWHM was 6 nm at a light intensity of approximately 5 mW cm^{-2}. The monochromatic light was modulated using an optical chopper at a frequency of 27 Hz. The modulation frequency was chosen slow enough such that the response of the sample was frequency-independent. The signal was detected via a low noise pre-amplifier (Femto DLPCA-200) and a lock-in amplifier (Signal Recovery 7230). During the measurement the light intensity was continuously monitored via a silicon photodiode connected to a second lock-in amplifier. The EQE measurement was referenced to the response of a silicon photodiode with NIST-traceable calibration.

7.5 Supporting Information

7.5.1 UV-Vis spectra of the COF precursors
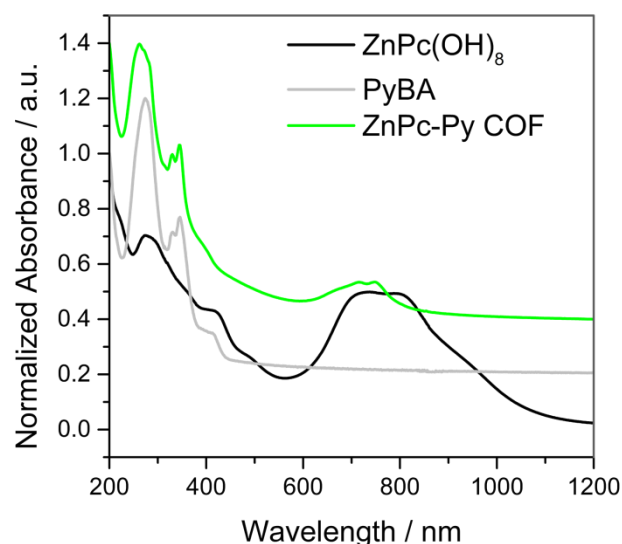
Figure 7.11 UV-Vis spectra of ZnPc(OH)$_8$ (black) PyBA (grey), and the ZnPc-Py COF (green). The spectra have been normalized to [0,1] and are offset for clarity.
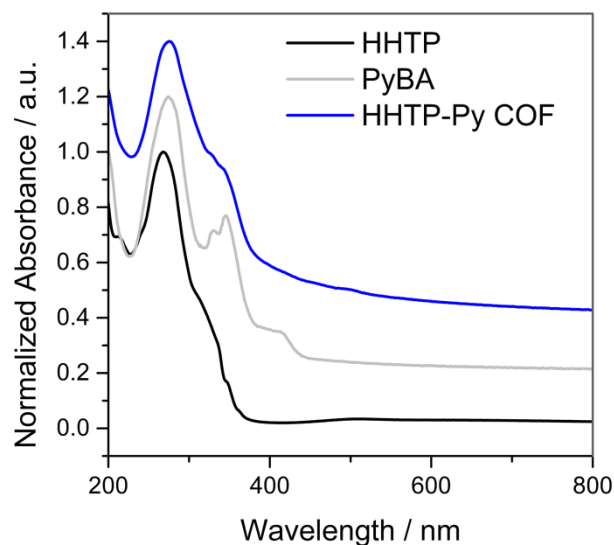
Figure 7.12 UV-Vis spectra of the HHTP-Py COF (blue) and its precursors HHTP (black) and PyBA (grey). The absorption bands of the pyrene at 330 and 346 nm appear as shoulders in the COF. The spectra have been normalized [0,1] and are offset for clarity.
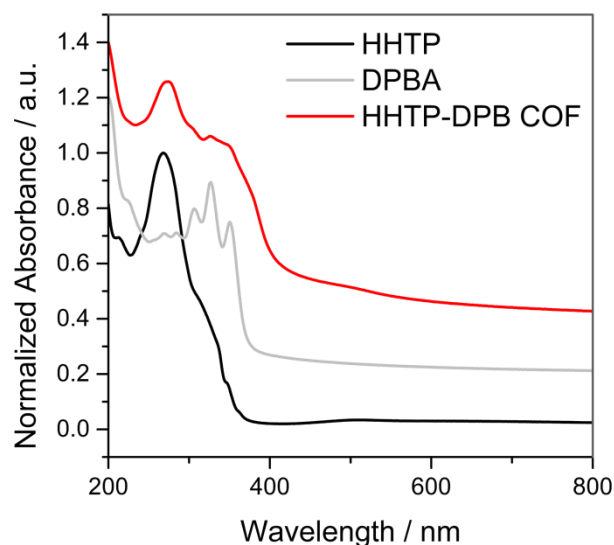
Figure 7.13 Absorbance of the HHTP-DPB COF (red) and its building blocks DPBA (grey) and HHTP (black). The features in the HHTP-DPB COF at 307, 327, and 350 nm originate from the DPB unit. The main HHTP absorption band at 269 nm is shifted to 274 nm upon incorporation into the COF framework. The spectra have been normalized to [0,1] and an offset has been added for clarity.
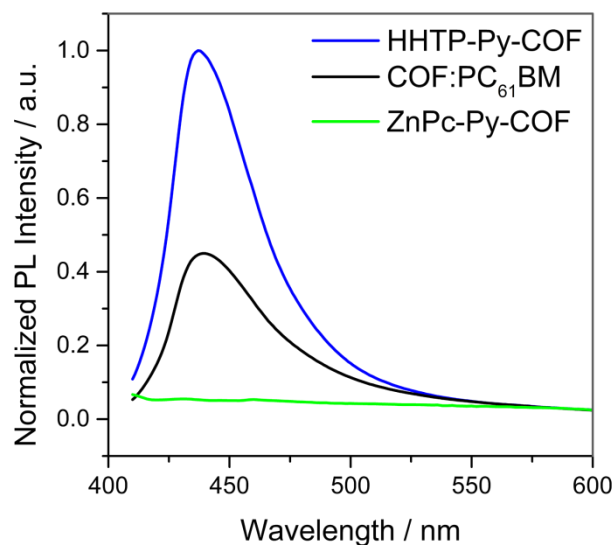
Figure 7.14 Photoluminescence spectra of the HHTP-Py (blue) and ZnPc-Py (green) COFs at 365 nm excitation. Infiltration of the HHTP-Py COF with $PC_{61}BM$ (black) results in a reduction of the PL intensity of 55%.
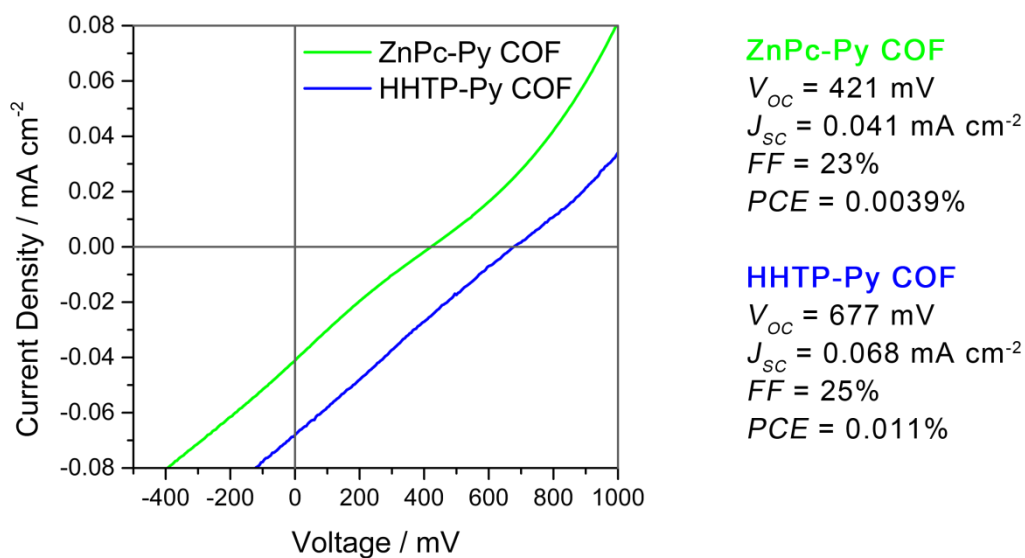
Figure 7.15 *J-V* characteristics of the ZnPc-Py (green) and HHTP-Py (blue) devices.

7.6 References

[1] http://www.nrel.gov/ncpv/

[2] Y. Liang, Z. Xu, J. Xia, S.-T. Tsai, Y. Wu, G. Li, C. Ray, L. Yu, *Adv. Mater.* **2010**, *22*, E135-E138.

[3] A. K. K. Kyaw, D. H. Wang, V. Gupta, J. Zhang, S. Chand, G. C. Bazan, A. J. Heeger, *Adv. Mater.* **2013**, *25*, 2397-2402.

[4] W. Li, A. Furlan, K. H. Hendriks, M. M. Wienk, R. A. J. Janssen, *J. Am. Chem. Soc.* **2013**, *135*, 5529-5532.

[5] M. A. Ruderer, S. Guo, R. Meier, H.-Y. Chiang, V. Körstgens, J. Wiedersich, J. Perlich, S. V. Roth, P. Müller-Buschbaum, *Adv. Funct. Mater.* **2011**, *21*, 3382-3391.

[6] M. Dogru, M. Handloser, F. Auras, T. Kunz, D. Medina, A. Hartschuh, P. Knochel, T. Bein, *Angew. Chem. Int. Ed.* **2013**, *52*, 2920-2924.

[7] A. P. Côte, A. I. Benin, N. W. Ockwig, M. O'Keeffe, A. J. Matzger, O. M. Yaghi, *Science* **2005**, *310*, 1166-1170.

[8] J. W. Colson, W. R. Dichtel, *Nat. Chem.* **2013**, *5*, 453-465.

[9] S. Wan, F. Gándara, A. Asano, H. Furukawa, A. Saeki, S. K. Dey, L. Liao, M. W. Ambrogio, Y. Y. Botros, X. Duan, S. Seki, J. F. Stoddart, O. M. Yaghi, *Chem. Mater.* **2011**, *23*, 4094-4097.

[10] X. Ding, L. Chen, Y. Honsho, X. Feng, O. Saengsawang, J. Guo, A. Saeki, S. Seki, S. Irle, S. Nagase, V. Parasuk, D. Jiang, *J. Am. Chem. Soc.* **2011**, *133*, 14510-14513.

[11] X. Ding, J. Guo, X. Feng, Y. Honsho, J. Guo, S. Seki, P. Maitarad, A. Saeki, S. Nagase, D. Jiang, *Angew. Chem. Int. Ed.* **2011**, *50*, 1289-1293.

[12] E. L. Spitler, J. W. Colson, F. J. Uribe-Romo, A. R. Woll, M. R. Giovino, A. Saldivar, W. R. Dichtel, *Angew. Chem. Int. Ed.* **2012**, *51*, 2623-2627.

[13] E. L. Spitler, B. T. Koo, J. L. Novotney, J. W. Colson, F. J. Uribe-Romo, G. D. Gutierrez, P. Clancy, W. R. Dichtel, *J. Am. Chem. Soc.* **2011**, *133*, 19416-19421.

[14] S. Wan, J. Guo, J. Kim, H. Ihee, D. Jiang, *Angew. Chem. Int. Ed.* **2008**, *47*, 8826-8830.

[15] S. Jin, X. Ding, X. Feng, M. Supur, K. Furukawa, S. Takahashi, M. Addicoat, M. E. El-Khouly, T. Nakamura, S. Irle, S. Fukuzumi, A. Nagai, D. Jiang, *Angew. Chem. Int. Ed.* **2013**, *52*, 2017-2021.

[16] M. D. Irwin, D. B. Buchholz, A. W. Hains, R. P. H. Chang, T. J. Marks, *PNAS* **2008**, *105*, 2783-2787.

[17]   J. R. Manders, S.-W. Tsang, M. J. Hartel, T.-H. Lai, S. Chen, C. M. Amb, J. R. Reynolds, F. So, *Adv. Funct. Mater.* **2013**, *23*, 2993-3001.

[18]   K. Vanderwal, K. Tvingstedt, A. Gadisa, O. Inganäs, J. V. Manca, *Nat. Mater.* **2009**, *8*, 904-909.

[19]   A. A. Bakulin, A. Rao, V. G. Pavelyev, P. H. M. Loosdrecht, M. S. Pshenichnikov, D. Niedzialek, J. Cornil, D. Beljonne, R. H. Friend, *Science* **2012**, *335*, 1340-1344.

[20]   G. H. V. Bertrand, V. K. Michaelis, T.-C. Ong, R. G. Griffin, M. Dinca, *PNAS* **2013**, *110*, 4923-4928.

[21]   S. Patwardhan, A. A. Kocherzhenko, F. C. Grozema, L. D. A. Siebbeles, *J. Phys. Chem. C* **2011**, *115*, 11768-11772.

[22]   T. E. Youssef, *Polyhedron* **2010**, *29*, 1776-1783.

[23]   C. C. Tzschucke, J. M. Murphy, J. F. Hartwig, *Org. Lett.* **2007**, *9*, 761-764.

8 Conclusion and Outlook

This thesis was focused on the creation and evaluation of model systems for hybrid and organic solar cells that feature a well-defined morphology on the nanoscale. A variety of concepts and synthetic approaches were employed to achieve this goal and the specific properties of the respective systems, including morphological and optoelectronic features, were analysed.

We employed a hybrid device concept comprising ordered arrays of zinc oxide nanowires and a subsequently introduced photoactive polymer. Zinc oxide nanowires have been widely studied as photoanodes due to their unique one-dimensional growth and favourable charge transport characteristics. We improved a hydrothermal synthesis approach for these nanowires, such that we were able to grow well-ordered nanowire arrays on transparent conducting substrates without the formation of bulk precipitates in the growth solution. These undesired precipitates could adhere to the growing nanowires and compromise the film quality and reproducibility. We were able to tune the synthesis conditions towards the growth of extremely thin nanowires, which provide the roughness factors and inter-wire distances that would be most favourable for efficient light harvesting in zinc oxide/polymer photovoltaic devices. In combination with poly(3-hexylthiophene) as a first model system we obtained a power conversion efficiency of 0.09% under simulated solar illumination. We found that our devices were mainly limited by comparably high dark currents, which originate from a high degree of defect-related doping.

In a collaboration with the groups of Dr Valentina Cauda (Istituto Italiano di Tecnologia, Turin, Italy) and Prof Barbara Onida (Politecnico di Torino, Turin, Italy) we utilized the piezoelectric properties of ZnO in nanogenerator devices. A detailed study on the effect of the synthetic parameters on the piezoelectric characteristics illustrated that appropriate conductivity and charge carrier concentration are key to good nanogenerator performance and that they can be systematically controlled via the growth conditions.

Furthermore, we examined the charge carrier generation capabilities of a porphyrin-containing periodic mesoporous organosilica. While porphyrin-based molecules are

known sensitizers in dye-sensitized solar cells and perform well in small molecule organic photovoltaics, the potential of porphyrin as photoactive building block in a well-defined organosilica morphology had not been explored so far. We synthesized an organosilica material with periodically ordered pores and studied its photoresponse in an electrolyte as well as in solid-state heterojunctions after infiltration with a suitable electron acceptor. Taking into account the insulating nature of the silica linkages, the observed photocurrents of about $25\,\text{nA}\,\text{cm}^{-2}$ are an indication for the existence of stacked porphyrin units inside the material that render it electronically conductive.

In the last projects described in this thesis we employed crystalline covalent organic frameworks (COFs) as semiconducting host materials. These materials consist of extended two-dimensional sheets with an atomically defined arrangement of covalently bound building blocks, which stack in the third dimension via π-π–interactions. We demonstrated that upon infiltration with an electron acceptor a bi-continuous network is formed. Specifically, we used a recently developed thienothiophene-containing COF to study the infiltration of COF films with the solution of a fullerene-based electron acceptor. From PL quenching experiments we concluded that the COF films have accessible pores throughout their entire thickness, while the degree of quenching and pore filling is tentatively attributed to the solubility of the employed fullerene derivative. Experiments with acceptors that feature higher LUMO energies resulted in a considerable improvement in open-circuit voltage.

We then investigated COFs that feature highly absorbing zinc phthalocyanine units in a collaboration with the group of Prof William Dichtel (Cornell University, Ithaca, USA). We found that the position and accessibility of the COF building blocks is key to effective charge carrier generation and that for the examples we have investigated thus far the main contribution to the photocurrent originates from the PCBM located inside the COF pores. The charge transport properties, however, seem to be strongly affected by the selection of COF building blocks. We conclude that the incorporation of the phthalocyanine units enhances the fraction of collected electrons significantly, although the direct contribution to the photocurrent is negligible.

In this thesis we have pursued different routes for obtaining structurally well-defined bulk heterojunctions for solar energy conversion. While the nanowire projects used the

anisotropic growth behaviour of zinc oxide in certain reaction mixtures, the periodic mesoporous organosilica was forced into its morphology via a soft template. Finally, the morphology of COFs is pre-defined by the molecular geometry of the building blocks and their packing due to π-π-interactions. All these approaches lead to the formation of a rigid semiconducting network, which subsequently was infiltrated with its counterpart to form a three-dimensional heterojunction.

Despite challenges in achieving sufficient infiltration and obtaining an interface that provides high charge carrier generation efficiency and low recombination rates, these nanostructured systems offer a unique degree of definition on the nanoscale, which renders them promising model systems for fundamental research in photovoltaics.

9 Supporting Information

9.1 Design of the solar simulator / EQE setup

During the course of this thesis we developed a setup for obtaining *J-V* curves under simulated solar irradiation and for measuring high quality EQE spectra with optional bias illumination or voltage bias (Figure 9.1).

9.1.1 Optical design

Simulated AM1.5G solar irradiation is obtained from a solar simulator (1) (Solar Light Model 16S). The spectrum of a 300 W Xe arc light source is adjusted by filters to match the solar spectrum in the UV-NIR range. The distance of the sample holder (4) can be adjusted such that the light intensity equals the standardized value of $100 \, \mathrm{mW \, cm^{-2}}$ (also referred to as full sun). Although the spectrum of the solar simulator closely resembles the standardized solar spectrum,[1] the intense spectral features of the Xe lamp cannot be fully suppressed. Depending on the spectral response of a specific solar cell, this might lead to a small difference in the current the cell produces in the test environment and the current the cell would produce under actual solar illumination at the identical overall light intensity. This spectral mismatch is minimized through using a reference cell for light intensity calibration, which has a spectral response very similar to the solar cell samples. We employ a calibrated reference cell with a KG5 glass filter that suppresses the response at wavelengths longer than 850 nm for this purpose. A series of reflective neutral density filters (2) allow for measurements at 50%, 20%, 10%, 5%, 1%, and 0.1% sun. An optional shutter (3) can be used for recording slow current transients or for quasi-simultaneous measurement of *J-V* curves in the dark and under illumination.
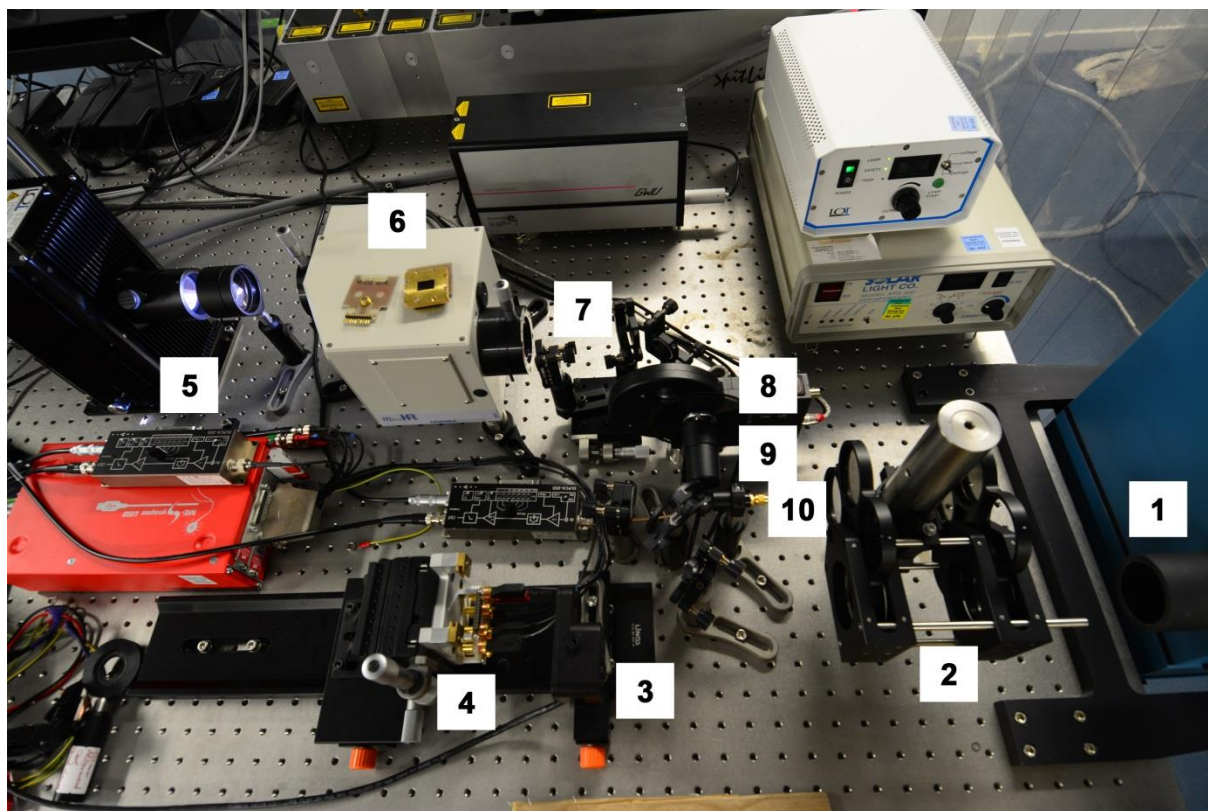
Figure 9.1   Layout of the solar simulator/EQE setup.

External quantum efficiency measurements are performed with pulsed monochromatic light to increase the signal to noise ratio and to enable measurements under bias illumination or at an applied potential.[2] Monochromatic light is obtained from a 150 W Xe short arc lamp (5) (LOT Oriel) in combination with a monochromator (6) (Horiba microHR). The design of the monochromator and the choice of the grating are optimized for high throughput at the cost of resolution. However, since most of our photovoltaic devices lack any sharp features, 6-8 nm bandpass are sufficient. The diverging monochromatic light is collimated or focused by a focusing unit (7) and passes a filter wheel with order-sorting long pass filters (8). For the 300-1200 nm range a 550 nm and a 1000 nm dielectric coated longpass filter are sufficient. Since the light intensity and the throughput of the monochromator are virtually zero below 300 nm, no filters are required to exclude second-order diffraction in this wavelength range. An optical chopper (9) is used to modulate the monochromatic beam at frequencies between 1 and 99 Hz. The modulation frequency needs to be chosen low enough that the response of

the cell is not frequency-dependent. Typical values are 27 or 43 Hz for good organic solar cells, 7-17 Hz for COF devices or solid-state dye-sensitized solar cells, and 1-2 Hz for haematite or liquid-electrolyte dye-sensitized solar cells. After passing the optical chopper, the light is divided into two beams by a 92:8 beamsplitter. The larger fraction of the beam is transmitted onto the sample, while the less intense beam is focused onto a silicon photodiode (10). We noted that, although the overall light intensity of the Xe lamp is very stable once the lamp has warmed up, the intensity of the xenon lines changes with time, causing artefacts in the EQE spectra. We therefore monitor the light intensity at each data point during the scan with the photodiode and correct for lamp drift between the reference scan and the measurement of a sample.

9.1.2 Signal detection

Up to four individual devices per substrate can be addressed automatically via computer-controlled relays. J-V curves are measured using a source meter (Keithley 2400) in remote sensing (4-point probe) operation. The 4-point probe ensures that the additional series resistance of the relays ($\sim$1 Ω) is not included in the measurement.

EQE spectra are recorded via lock-in technique. The current through the device under test is converted into a voltage signal via a low-noise pre-amplifier (Femto DLPCA-200). Detection via a lock-in amplifier (Signal Recovery 7230), using the modulation frequency of the optical chopper as reference, ensures that only the response of the device to the monochromatic light is detected. Any current originating from white light bias or an applied voltage adds a constant offset to the signal and is not detected.

An identical combination of pre-amplifier and lock-in detection is used for the silicon photodiode, which serves as an internal reference to monitor and correct for variations in light intensity.

As described in Chapter 2.4 the external quantum efficiency relates the collected current to the flux of incident photons. In practice, the number of incident photons is determined from a reference scan with a calibrated photodiode. The EQE of a sample is then obtained from

$$EQE = \frac{J_{sample}}{J_{ref}} \times EQE_{ref}$$

where J_{sample} and J_{ref} are the current densities measured for the sample and the calibrated reference cell, respectively, and EQE_{ref} is the known EQE of the reference cell. If using a photodiode as internal reference, a correction factor is added to the above equation.

$$EQE = \frac{J_{sample}}{J_{ref}} \times EQE_{ref} \times \frac{V_{ref}}{V_{sample}}$$

V_{ref} and V_{sample} are the signal of the photodiode during the reference and the sample scan, respectively. This method assumes that all devices respond linearly to small fluctuations in light intensity, which proved to be a good approximation for lamp drift of a few percent over several hours.

9.2 The VIS/NIR PL setup

We furthermore set up a photoluminescence setup capable of measuring PL of films in the VIS and NIR range. The output of a 365 nm LED (1) is collimated and focused onto the sample (3). A 400 nm shortpass filter and dielectric mirrors (2) that reflect only at wavelengths below 400 nm are used to suppress the small visible output of the LED. PL of the sample is collected and focused onto the entrance slit of a monochromator (4) (Horiba iHR320). A 1200 l/mm grating is used together with a photomultiplier tube (5) for the 400-860 nm range. For the NIR range from 860-1600 nm a 900 l/mm grating and a liquid N_2-cooled InGaAs detector (6) are used. High quality longpass filters (400 nm, 550 nm, 1000 nm) in an internal filter wheel suppress higher order diffraction signals and ensure that no scattered light from the excitation source can enter the detection system. Typical wavelength resolution of this setup is 0.2-4 nm, depending on the width of the entrance and exit slits.

For obtaining maximal signal to noise ratio we use lock-in detection on this setup. The LED can be modulated via an arbitrary function generator (HP 33120A), which also provides the reference to the lock-in amplifier (Signal Recovery 7230). An optical

chopper (7) can be used as modulation source if a non-modulated light source is used for excitation.

Figure 9.2 Photograph of the VIS/NIR PL setup.

9.3 References

[1] http://rredc.nrel.gov/solar/spectra/am1.5

[2] T. J. K. Brenner, Z. Li, C. R. McNeill, *J. Phys. Chem. C* **2011**, *115*, 22075-22883.

10 Curriculum Vitae

Persönliche Daten	
Geburtsdatum / -ort	03.11.1982, Augsburg
Nationalität	deutsch

Ausbildung	
08/2009 –	**Ludwig-Maximilians-Universität München**
	Promotion
	Thema: Solar light harvesting with nanostructured organic and hybrid photovoltaic devices (Prof. Thomas Bein)
07/2010 – 08/2010	**University of Bath, England**
	Forschungsaufenthalt bei Prof. Laurence Peter
	Thema: Transport and recombination in nanostructured solar cells
	Teilnahme an der Bath Electrochemical Impedance Summer School
10/2008 – 04/2009	**Eidgenössische Technische Hochschule Zürich, Schweiz**
	Forschungsprojekt
	Thema: Catalytic properties of palladium complexes (Prof. Hansjörg Grützmacher)
12/2007 – 06/2008	**Technische Universität München, LMU München, Universität Augsburg, Universitetet i Bergen, Norwegen**
	Masterstudium Advanced Materials Science
	Abschlussarbeit: Molecular magnetism in lanthanide alkylaluminates (Prof. Wolfgang Scherer)
	Abschluss: **Master of Science**
10/2003 – 09/2006	**Universität Augsburg**
	Bachelorstudium Materialwissenschaften
	Abschlussarbeit: Design and characterisation of *N*-heterocyclic

ligands for the synthesis of molybdenum hybrid materials (Prof. Wolfgang Scherer)

Abschluss: **Bachelor of Science**

Stipendien

05/2007 – 06/2008	Stipendium der Studienstiftung des deutschen Volkes

Berufliche Erfahrung

08/2007 – 09/2007	**hte AG**
	High-throughput synthesis of supported catalysts
02/2004 – 04/2004	**EADS Deutschland GmbH**
	Surface modification of aircraft components

Weitere Fähigkeiten

Sprachkenntnisse	Deutsch: Muttersprache
	Englisch: Fließend in Wort und Schrift
Softwarekenntnisse	LabView, AutoCAD Inventor, InDesign, Photoshop, Origin, POVRay

11 Publications and Presentations

11.1 Publications

1. Synthesis and stability of homoleptic metal(III) tetramethylaluminates

    G. Occhipinti, C. Meermann, H.-M. Dietrich, R. Litlabo, F. Auras, K. W. Toernroos, C. Maichle-Moessmer, V. R. Jensen, R. Anwander, *J. Am. Chem. Soc.* **2011**, *133*, 6323-6337.

2. Characterization of Interfacial Modifiers for Hybrid Solar Cells

    J. Weickert, F. Auras, T. Bein, L. Schmidt-Mende, *J. Phys. Chem. C* **2011**, *115*, 15081-15088.

3. Synthesis and characterization of $CuInS_2$ thin film structures

    A. Wochnik, C. Heinzl, F. Auras, T. Bein, C. Scheu, *J. Mater. Sci.* **2012**, *47*, 1669-1676.

4. A Photoconductive Thienothiophene-Based Covalent Organic Framework Showing Charge Transfer Towards Included Fullerene

    M. Dogru, M. Handloser, F. Auras, T. Kunz, D. Medina, A. Hartschuh, P. Knochel, T. Bein, *Angew. Chem. Int. Ed.* **2013**, *52*, 2920-2924.

5. Length-Dependent Charge Generation from Vertical Arrays of High-Aspect-Ratio ZnO Nanowires

    V. F. Rivera, F. Auras, P. Motto, S. Stassi, G. Canavese, E. Celasco, T. Bein, B. Onida, V. Cauda, *Chem. Eur. J.* **2013**, DOI: 10.1002/chem.201204429.

6. A Photoactive Porphyrin-Based Periodic Mesoporous Organosilica Thin Film

    Y. Li, F. Auras, F. Löbermann, M. Döblinger, J. Schuster, L. Peter, D. Trauner, T. Bein, *submitted*.

7.   Oriented Thin Films of a Photoactive Benzodithiophene Covalent Organic Framework

D. Medina, V. Werner, F. Auras, M. Dogru, J. Schuster, S. Linke, M. Döblinger, P. Knochel, T. Bein, *submitted*.

11.2 Oral presentations

1.   Covalent Organic Framework-Based Solar Cells

F. Auras, M. Dogru, D. Medina, T. Kunz, P. Knochel, T. Bein, *HOPV* **2013**, Seville, Spain.

2.   Covalent Organic Framework-Based Photovoltaics

F. Auras, M. Dogru, M. Calik, D. Medina, T. Bein, *NIM Nanosystems for Energy Conversion* **2013**, Munich.

11.3 Poster presentations

1.   Nanostructured Solid-State Solar Cells

F. Auras, N. K. Minar, J. M. Szeifert, A. Wochnik, C. Scheu, T. Bein, *CeNS Workshop* **2010**, Venice, Italy.

2.   Oriented Zinc Oxide Nanowire Arrays with Tuneable Morphology and Dimensions for Hybrid Solar Cells

F. Auras, V. C. F. Rivera, I. Kondofersky, T. Bein, *HOPV* **2012**, Uppsala, Sweden.

3.   Polymer/Metal Oxide Hybrid Solar Cells Based on Ultra-Thin Nanowires

F. Auras, E. Kouhiisfahani, T. Bein, *CeNS Workshop* **2012**, Venice, Italy.

4.   Host-Guest Interactions in Photoactive Covalent Organic Frameworks

F. Auras, M. Dogru, D. Medina, T. Kunz, V. Werner, P. Knochel, T. Bein, *25. Deutsche Zeolith-Tagung* **2013**, Hamburg.

5. Host-Guest Interactions in Photoactive Covalent Organic Frameworks

F. Auras, M. Dogru, D. Medina, T. Kunz, V. Werner, P. Knochel, T. Bein, *SolTech Symposium* **2013**, Kloster Banz.